

PROJECTILE THRUST-DRAG OPTIMIZATION  
WITH EXTERNAL BURNING

William John Henry Smithey

DUDLEY KNOX LIBRARY  
NAVAL POSTGRADUATE SCHOOL  
MONTEREY, CALIFORNIA 93940

# NAVAL POSTGRADUATE SCHOOL

## Monterey, California



# THESIS

PROJECTILE THRUST-DRAG OPTIMIZATION  
WITH EXTERNAL BURNING

by

William John Henry Smithey

June 1974

Thesis Advisor:

Allen E. Fuhs

Approved for public release; distribution unlimited.

T 162 504



UNCLASSIFIED

SECURITY CLASSIFICATION OF THIS PAGE (When Data Entered)

REPORT DOCUMENTATION PAGE		READ INSTRUCTIONS BEFORE COMPLETING FORM
1. REPORT NUMBER	2. GOVT ACCESSION NO.	3. RECIPIENT'S CATALOG NUMBER
4. TITLE (and Subtitle) Projectile Thrust - Drag Optimization With External Burning		5. TYPE OF REPORT & PERIOD COVERED Doctor's Thesis; June 1974
		6. PERFORMING ORG. REPORT NUMBER
7. AUTHOR(s) William John Henry Smithey		8. CONTRACT OR GRANT NUMBER(s)
9. PERFORMING ORGANIZATION NAME AND ADDRESS Naval Postgraduate School Monterey, California 93940		10. PROGRAM ELEMENT, PROJECT, TASK AREA & WORK UNIT NUMBERS
11. CONTROLLING OFFICE NAME AND ADDRESS Naval Postgraduate School Monterey, California 93940		12. REPORT DATE June 1974
		13. NUMBER OF PAGES 130
14. MONITORING AGENCY NAME & ADDRESS (if different from Controlling Office) Naval Postgraduate School Monterey, California 93940		15. SECURITY CLASS. (of this report) UNCLASSIFIED
		15a. DECLASSIFICATION/DOWNGRADING SCHEDULE
16. DISTRIBUTION STATEMENT (of this Report)  Approved for public release; distribution unlimited.		
17. DISTRIBUTION STATEMENT (of the abstract entered in Block 20, if different from Report)		
18. SUPPLEMENTARY NOTES		
19. KEY WORDS (Continue on reverse side if necessary and identify by block number) Base Drag Reduction Axisymmetric Heat Addition External Heat Addition Method of Characteristics With Heat Addition		
20. ABSTRACT (Continue on reverse side if necessary and identify by block number) External burning increases base pressure. The characteristic and linearized equations with heat addition are discussed, and the condition for maintaining irrotationality with heat addition is derived. A transition model, which extends the Crocco-Lees base flow model, and a spin model are discussed. Computed results are compared with experiment. The optimum location for supersonic external burning is given.		



UNCLASSIFIED

SECURITY CLASSIFICATION OF THIS PAGE(When Data Entered)

Block #19 continued

Base Flow

Base Drag





Projectile Thrust-Drag Optimization

With External Burning

by

William John Henry Smithey

Commander, United States Navy

B.M.E., University of Virginia, 1957

B.S., Naval Postgraduate School, 1963

A.E., California Institute of Technology, 1964

Submitted in partial fulfillment of the  
requirements for the degree of

DOCTOR OF PHILOSOPHY

from the

NAVAL POSTGRADUATE SCHOOL

June 1974



## ABSTRACT

External burning increases base pressure. The characteristic and linearized equations with heat addition are discussed, and the condition for maintaining irrotationality with heat addition is derived. A transition model, which extends the Crocco-Lees base flow model, and a spin model are discussed. Computed results are compared with experiment. The optimum location for supersonic external burning is given.



## TABLE OF CONTENTS

I.	INTRODUCTION.....	12
II.	THEORY.....	18
III.	EXPERIMENTAL INVESTIGATION.....	37
IV.	NUMERICAL INVESTIGATION.....	48
V.	DISCUSSION OF RESULTS.....	54
VI.	CONCLUSIONS.....	73
APPENDIX A:	DERIVATION OF THE CHARACTERISTIC EQUATIONS WITH HEAT ADDITION.....	75
APPENDIX B:	DERIVATION OF CONDITION FOR IRROTATION- ALITY WITH HEAT ADDITION.....	79
APPENDIX C:	BRIEF DEVELOPMENT OF CROCCO-LEES BASE FLOW FORMULATION.....	83
APPENDIX D:	CALCULATION OF BOUNDARY LAYER MASS FLUX AT THE BASE.....	87
APPENDIX E:	MASS FLUX CALCULATION ALONG THE SHEAR LAYER.....	90
APPENDIX F:	CALCULATION OF BOUNDARY LAYER THICKNESS AND MIXING COEFFICIENT.....	92
APPENDIX G:	DERIVATION OF LINEARIZED STEADY FLOW EQUATION WITH HEAT ADDITION.....	96
APPENDIX H:	DETERMINATION OF THE MACH ANGLE.....	98
APPENDIX I:	SPINNING CYLINDER DESIGN.....	101
APPENDIX J:	COMPUTER PROGRAM.....	103
	COMPUTER PROGRAM.....	107
	LIST OF REFERENCES.....	124
	INITIAL DISTRIBUTION LIST.....	128



## LIST OF TABLES

I.	Base Pressure Ratio and Specific Impulse with Simulated Heat Addition.....	46
II.	Comparison of Calculated Base Pressure Ratio with External Heat Addition, Two Dimensional Planar Flow and Mach Number of 2.3.....	60





## LIST OF FIGURES

1.	External Burning Projectile.....	13
2.	Base Pressure Ratio and Flow Angle.....	15
3.	Natural and Characteristic Coordinate Systems.....	19
4.	Conceptual Diagram Depicting Shear Layer Pressures, $P_{SL}$ , Which Straddle the Critical Point.....	26
5.	Transition Model.....	27
6.	Transition of Shear Layer Mixing Coefficient.....	31
7.	Momentum Control Volume Depicting Shear Layer Mixing.....	32
8.	Sensitivity of Base Pressure Ratio.....	34
9.	Computed Values of $p_b/p_\infty$ vs. Reynolds Number, Mach 2.0, No Heat Addition.....	35
10.	Heat Zone Simulation with Nozzle Wall.....	38
11.	Photograph of Free Jet Experimental Facility.....	39
12.	Schematic Diagram of Free Jet Experimental Facility.....	40
13.	Coaxial Epoxy Nozzle. Insert Showing Spacers.....	42
14.	Schlieren Photographs at Mach 2.0 Showing Uniform Flow and Flow with Compression.....	44
15.	Characteristic Mesh.....	49
16.	Integration in the $F - w_e$ Plane.....	51
17.	Computed Values of $p_b/p_\infty$ , Transition Points and Critical Point.....	55
18.	Experimental Values of $p_b/p_\infty$ vs. Reynolds Number Without Heat Addition, from Ref. 32.....	56
19.	Experimental Values of $p_b/p_\infty$ vs. Reynolds Number Without Heat Addition.....	57



20.	Comparison of Experimental and Computed Values of Base Pressure Ratio vs. Reynolds Number at Mach 2.0 Without and With Simulated Heat Addition.....	62
21.	Comparison of Experimental [Ref. 26] and Computed Values of Base Pressure Ratio vs. Reynolds Number With Spin.....	64
22.	Computed Values of Base Pressure Ratio at a Mach Number of 2.0 With External Burning.....	66
23.	Comparison of Calculated Base Flow With And Without Heat Addition at Mach 2.0.....	68
24.	Schematic Diagram of Resulting Base Flow When an External Shock Wave Impinges on the Shear Layer...	71
1I.	Disassembled View of Spinning Cylinder.....	102
1J.	Simplified Flow Diagram for External Burning Assisted Projectile (EBAP) Computer Program.....	105



## NOTATION

### English

$a$	speed of sound, feet/second
$C_f$	skin friction coefficient, dimensionless
$c_p$	specific heat at constant pressure, foot-pounds/slug-degree Rankine
$F$	dimensionless ratio of various boundary layer thicknesses
$h$	specific enthalpy, foot-pounds/slug
$k$	shear layer mixing coefficient, dimensionless
$L$	body length, feet
$M$	Mach number, dimensionless
$\bar{m}$	mass flux, slugs/second-square foot
$n$	normal coordinate, feet; also velocity profile integer
$p$	static pressure, pounds/square-foot
$Q$	heat added per unit mass, foot-pounds/slug; also dimensionless heat addition rate of Eqn. (12)
$q$	heat addition rate, foot-pounds/slug-second
$R$	universal gas constant, foot-pounds/slug-degree Rankine
$Re$	Reynolds number, dimensionless
$r$	radial coordinate, feet
$S$	specific entropy, foot-pounds/slug-degree Rankine
$s$	streamline coordinate, feet
$T$	static temperature, degrees Rankine
$\bar{U}$	velocity vector, feet/second
$U, u$	speed, feet/second



w speed along streamline, feet/second; also  
nondimensionalized by stagnation speed  
of sound,  $a_s$

w/r dimensionless heat zone length

z/r dimensionless position on body or shear layer,  
measured from base

#### Greek

$\alpha$  flow field type, dimensionless

$\beta$   $(M^2 - 1)^{1/2}$

$\gamma$  ratio of specific heats, dimensionless

$\delta$  boundary layer thickness, feet

$\delta^*$  boundary layer displacement thickness, feet

$\delta^{**}$  boundary layer momentum thickness, feet

$\epsilon$  dimensionless small quantity,  $0 < \epsilon \ll 1$

$\eta$  left running characteristic coordinate, feet;  
also dimensionless heating parameter of Ref. 7

$\theta$  flow angle, radians

$\kappa$  dimensionless ratio of average internal to  
external speed

$\mu$  Mach angle, radians

$\nu$  Prandtl-Meyer angle, radians

$\xi$  right running characteristic coordinate, feet

$\rho$  density, slugs/cubic foot

$\phi$  perturbation velocity potential, square feet/second

$\bar{\Omega}$  curl  $\bar{U}$ , radians/second

$\omega$  angular velocity, radians/second

#### Superscripts

( )' dimensionless perturbation quantity





## Subscripts

1	average condition
$\infty$	freestream condition
b	base condition
e	condition at edge of shear layer
L	laminar
o,s	total or stagnation condition
T	turbulent
tr	laminar transition point
trt	turbulent transition point



## I. INTRODUCTION

Projectiles in supersonic flight experience drag. One source of drag is due to the pressure acting on the base (rear surface) of the projectile, which, under normal circumstances, is below ambient pressure. The base drag force is equal to the base surface area normal to the direction of flight multiplied by the mean difference between the ambient and base pressures.

External burning has been studied by many authors [Ref. 1] to determine its ability to reduce the drag of a body or even to produce thrust. The basic objective of external burning in a supersonic flow, Fig. 1, is to create compression waves which impinge on the base flow region and increase the static pressure within the recirculation zone, thereby increasing the pressure acting on the base of the body to reduce base drag or produce thrust.

Other methods of reducing base drag or producing thrust are available. The rocket assisted projectile provides thrust from combustion of self-contained fuel and oxidizer. With external burning, additional fuel can replace some of this oxidizer since oxygen is used from the atmosphere for burning the excess fuel. The ram jet assisted projectile delivers excellent performance but does require air inlets and has additional hardware costs. The method of base burning offers advantages similar to external burning, but has not proven its ability to create thrust.



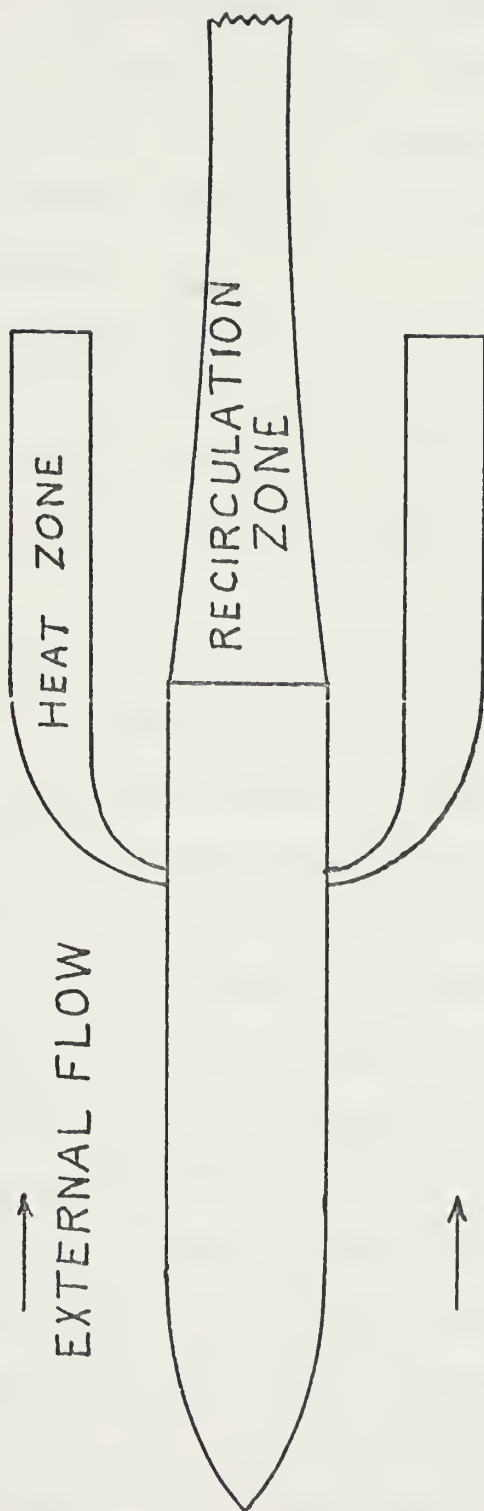


Figure 1. External Burning Projectile



The external burning assisted projectile provides a 50% increase in range when fuel rich propellant is substituted for one third of the conventional projectile payload. In addition to an increase in range, external burning can be used to decrease the projectile flight time to the target, increase its kinetic energy at the target and provide a flatter trajectory.

The base pressure ratio,  $p_b/p_\infty$ , is a measure of the effectiveness of the external burning process. As shown in Fig. 2, the behavior and effect of this ratio can be related to the flow angle,  $\theta$ , of the boundary layer streamline at the base.

For purposes of analysis, the external burning process may be described thermodynamically as a heat addition term in the energy equation, bearing in mind that numerous other factors must be considered with actual combustion, such as the effect of pressure on combustion rate. The linearized problem involving two dimensional planar uniform flow with unit heat addition has been solved by Tsien and Beilock in closed form [Ref. 2,3]. In supersonic flow it was shown that a pressure perturbation, due to the heat source, is transmitted along a characteristic. Further study of the linearized flow equations by Rues has shown that there is an equivalence between heat, force and mass sources [Ref. 4]. These unit sources were given an integral formulation by Fuhs to determine the flow field perturbation resulting from a source zone [Ref. 5]. It is the study of these linearized





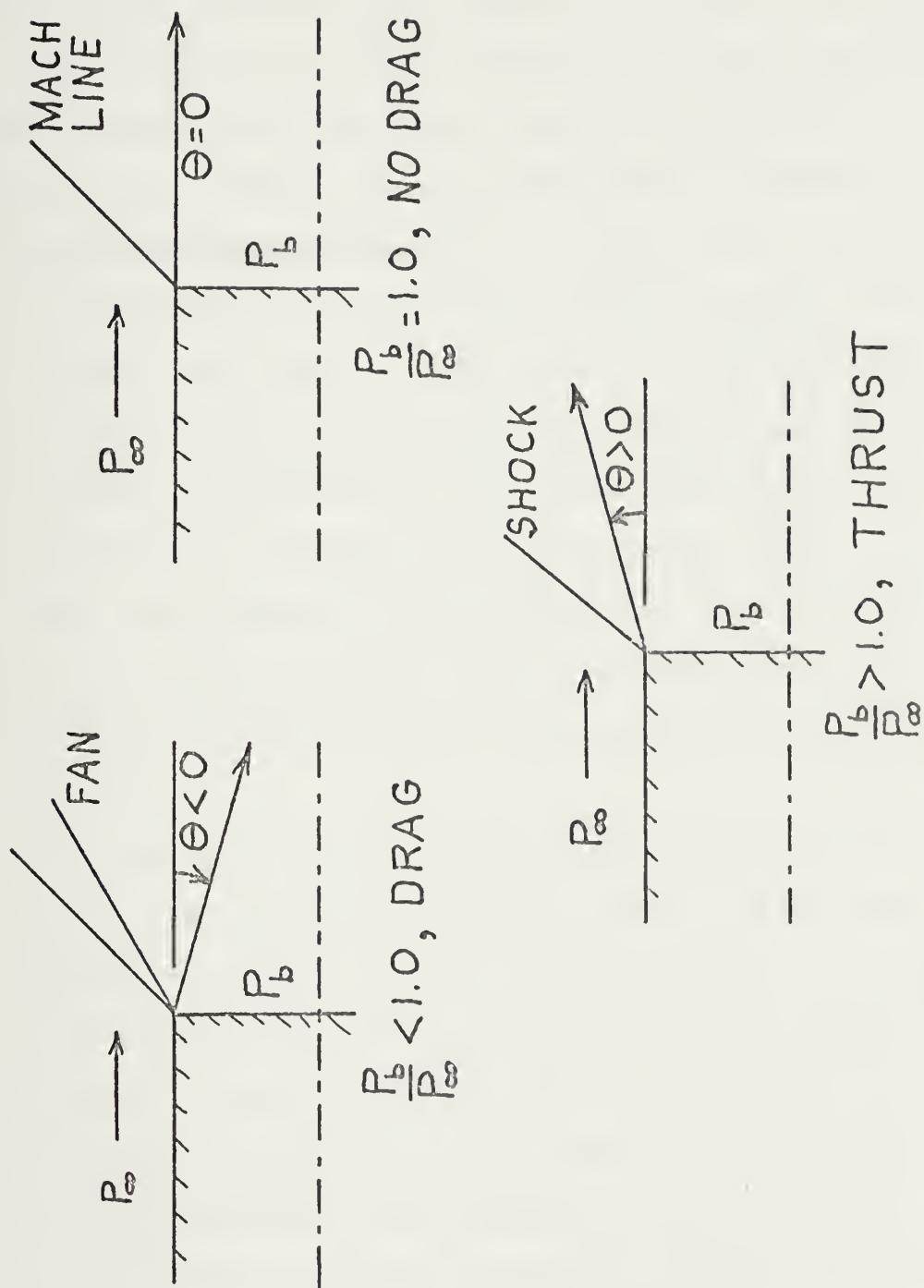


Figure 2. Base Pressure Ratio and Flow Angle



results which suggested that for experimental investigation the external burning process may be simulated by supersonic nozzle wall contours which generate identical characteristics.

Heat addition in a two dimensional planar supersonic flow was investigated by Strahle, using one dimensional and linearized heat addition theory, and shown to reduce base drag or produce thrust [Ref. 6,7]. In this study, the base flow was described by the Crocco-Lees [Ref. 8] model, and the resulting base pressure ratio was determined for heat addition zones of different intensity, location and extent. Experimental investigation [Ref. 9-11] has demonstrated the feasibility of external burning and shown that it can increase base pressure. Heat addition in an axisymmetric supersonic flow has been studied by Hosack and O'Leary using the method of characteristics and the Korst base flow model [Ref. 11].

The object of the present investigation was to study base pressure in two dimensional planar and axisymmetric supersonic flow with external heat addition using the method of characteristics and the Crocco-Lees base flow model. The effects of varying Reynolds number, including boundary layer transition, and projectile spin have been included. A concurrent experimental investigation studied the effect on base pressure of various axisymmetric nozzle contours which simulated the external burning process.

It should be mentioned that several combinations of external heat addition analysis and base flow models have not



been investigated theoretically. These include two dimensional planar method of characteristics and linearized theory with the Chapman-Korst base flow model, and linearized axisymmetric flow with both the Chapman-Korst and Crocco-Lees base flow models. The linearized axisymmetric flow problem will be discussed later.



## II. THEORY

The theory employed for this investigation must describe the steady flow in two entirely different flow regimes, Fig. 1. The external flow is supersonic and can be accurately treated by the method of characteristics. The internal viscous flow, or recirculation zone, is dissipative and difficult to describe. As in the two dimensional case, it was assumed that the Crocco-Lees model [Ref. 1,12-15] adequately describes the axisymmetric internal flow. Boundary layer type (laminar or turbulent), thickness and transition were included as a function of Reynolds number since these effects profoundly influence the base flow behavior.

The characteristic equations have been derived for flow with heat addition [Ref. 16,17]. In vector notation the steady equations for flow without viscosity, heat conduction or body forces are

$$\nabla \cdot (\rho \bar{U}) = 0 \quad (1)$$

$$\rho \bar{U} \cdot \nabla \bar{U} + \nabla p = 0 \quad (2)$$

$$\bar{U} \cdot \nabla (h + \frac{1}{2} \bar{U} \cdot \bar{U}) = q \quad (3)$$

$$p = \rho RT \quad (4)$$

where  $\rho$  is density,  $\bar{U}$  is velocity,  $p$  is static pressure,  $h$  is enthalpy,  $q$  is the time rate of heat addition per unit mass,  $R$  is the universal gas constant and  $T$  is static temperature. Using a natural coordinate system [Ref. 18], Fig. 3, the characteristic equations were derived from the above equations









in the following convenient form (Appendix A)

$$\frac{\partial(v-\theta)}{\partial\eta} = \left( \frac{\alpha \sin\theta}{r/r_b} - \frac{r_b q}{U c_p T} \right) \sin\mu - \frac{\cos\mu}{U^2} \left( T \frac{\partial S}{\partial n} - \frac{\partial h_0}{\partial n} \right) \quad (5)$$

$$\frac{\partial(v+\theta)}{\partial\xi} = \left( \frac{\alpha \sin\theta}{r/r_b} - \frac{r_b q}{U c_p T} \right) \sin\mu + \frac{\cos\mu}{U^2} \left( T \frac{\partial S}{\partial n} - \frac{\partial h_0}{\partial n} \right) \quad (6)$$

where  $\theta$ ,  $v$  and  $\mu$  are respectively the flow, Prandtl-Meyer and Mach angles,  $U$  is speed,  $S$  is specific entropy and  $h_0$  is total enthalpy,  $h_0 = h + \frac{1}{2}U^2$ . The left and right running characteristics are  $\eta$  and  $\xi$  respectively. The natural coordinates,  $s$  and  $n$ , are along and normal to the streamline. For two dimensional planar flow,  $\alpha$  is 0, and  $\alpha$  is 1 for axisymmetric flow. The characteristic equations, (5) and (6), have been multiplied by the characteristic length of base radius,  $r_b$ , to obtain a dimensionless form. Therefore, in contrast to the dimensional coordinates  $\eta$ ,  $\xi$  and  $n$  used in Fig. 3, the coordinates  $\eta$ ,  $\xi$  and  $n$  in Eqns. (5) and (6) are understood to be dimensionless. Also, the specific heat at constant pressure,  $c_p$ , was assumed constant in the enthalpy relation  $h = c_p T$ .

The characteristic computations with Eqns. (5) and (6) were simplified by neglecting the term  $\frac{1}{U} \left( T \frac{\partial S}{\partial n} - \frac{\partial h_0}{\partial n} \right) / r_b$ , which is the vorticity. One may assume the external flow to be irrotational before heat addition and then determine the restrictions on heat addition which preserve irrotationality. Crocco's theorem for steady flow may be written (Appendix B)

$$TVS + \bar{U}X\bar{\Omega} = v h_0 \quad (7)$$

where  $\bar{\Omega} = \nabla X \bar{U}$ . Taking the curl of Eqn. (7)



$$\dot{\bar{U}} \cdot \nabla \bar{\Omega} = \bar{\Omega} \cdot \nabla \bar{U} - \bar{\Omega} \nabla \cdot \bar{U} + \nabla T X \nabla S. \quad (8)$$

Assume  $\bar{\Omega} = 0$  before and during heat addition. Then, from Eqn. (8), the condition which preserves irrotationality is

$$\nabla T X \nabla S = 0. \quad (9)$$

If one redefines the heat addition and has uniform upstream conditions at infinity [Ref. 19], then

$$\nabla(h_0 - Q) = 0 \quad (10)$$

where  $Q$  is the heat per unit mass which has been supplied to the fluid element. Using Eqn. (7), with  $\bar{\Omega} = 0$ , Eqns. (9) and (10) yield the following result

$$\nabla Q X \nabla (\frac{1}{2} U^2) = 0 \quad (11)$$

which is the condition preserving irrotationality; that is, the gradients of kinetic energy and heat added must be parallel. If  $Q$  is a small perturbation,  $(Q/h_\infty) = \epsilon$ , then Eqn. (11) is of order  $\epsilon^2$  and the irrotationality condition is automatically satisfied to order  $\epsilon$ . To neglect the vorticity term in Eqns. (5) and (6), one must insure

$$\frac{r_{bq}}{U c_p T} = r_{b \frac{\bar{U} \cdot \nabla Q}{U c_p T}} = \epsilon \ll 1. \quad (12)$$

In the computations discussed in Section V, the quantity of Eqn. (12),  $(r_{bq})/(U c_p T)$ , was assigned a constant value independent of local pressure, within the heat zone and was taken as zero outside the heat zone. Thus, within the heat zone,  $\nabla Q$  was approximately parallel to the gradient of kinetic energy and the irrotationality condition of Eqn. (11) was



satisfied. This condition was not satisfied along the inner and outer streamlines of the heat zone, since a jump in  $Q$  existed normal to the streamlines. However, by assigning a value for Eqn. (12),  $(r_b q)/(U c_p T) \leq 0.2 \ll 1$ , the irrotationality condition was satisfied to order epsilon along the streamline boundaries of the heat zone.

Equations (1) through (4) may be combined to give

$$\nabla \cdot \bar{U} - \frac{1}{a^2} \bar{U} \cdot \nabla (\frac{1}{2} \bar{U} \cdot \bar{U}) = \frac{q}{c_p T} \quad (13)$$

where  $a$  is the speed of sound. Assuming small perturbation, Eqn. (13) may be linearized (Appendix G)

$$\nabla^2 \phi - M_\infty^2 \frac{\partial^2 \phi}{\partial x^2} = q' \quad (14)$$

where  $M_\infty$  is the Mach number at infinity,  $q'$  is the heat addition,  $q = h_\infty q'$ ,  $\phi$  is the perturbation velocity potential,  $\bar{U} = \bar{U}_\infty + \bar{U}'$ ,  $\bar{U}' = \nabla \phi$  and  $T = T_\infty(1+T')$ . In Cartesian coordinates, Eqn. (14) may be written

$$-\beta^2 \phi_{xx} + \phi_{yy} + \phi_{zz} = q' \quad (15)$$

where  $\beta^2 = M_\infty^2 - 1$ . For supersonic flow, the solution of Eqn. (15) is found by integrating the sources in the fore-cone volume,  $V_f$  [Ref. 20],

$$\phi = - \frac{1}{2\pi} \int_{V_f} \frac{q' dx_1 dy_1 dz_1}{((x-x_1)^2 - \beta^2((y-y_1)^2 + (z-z_1)^2))^{\frac{1}{2}}}. \quad (16)$$

Although the linearized theory was not pursued further, it should be noted that this theory could be used instead of the method of characteristics to establish the effect of





external burning at the base flow shear layer. Studies of linearized supersonic flow through ducts have provided solutions for an annular source distribution [Ref. 21-23], which could be used in conjunction with centerline sources and sinks [Ref. 18] to describe the axisymmetric external flow with burning.

The two dimensional planar Crocco-Lees theory [Ref. 8] considers the base flow as a separated boundary layer merging into a free jet profile and derives integral equations to describe the mean values of the flow quantities (Appendix C). From the integrals of the conservation equations, a single ordinary differential equation is derived. This ordinary differential equation has a saddle point singularity; existence of the singularity is a key feature of the Crocco-Lees model. The behavior of this equation is partly determined by an empirical  $F - \kappa$  relation and by the nature of the shear layer mixing.  $\kappa$  is the ratio of average internal base flow velocity to the external velocity,  $u_1/u_e$ .  $F$  is a ratio formed by using the various boundary layer thicknesses. The turbulent shear layer mixing coefficient,  $k_T$ , was assigned the constant value, 0.03, by Crocco-Lees. The laminar value used for this investigation was 0.0033, about 1/9 the turbulent value.

$F$  is conceptually a profile form factor; when the velocity profile changes shape, the value of  $F$  changes. As discussed in reference 8, the  $F - \kappa$  functional relationship is based on many known viscous flows. For example the Blasius



solution is represented by a point in the  $F - \kappa$  plane.

Falkner-Skan boundary layer solutions, which involve either favorable or adverse pressure gradients, become a curve in the  $F - \kappa$  plane. The velocity profiles of jets under certain conditions are described by the error function; these jets become a point in the  $F - \kappa$  plane. Likewise the Howarth boundary layer solutions for flows in pressure gradients are a curve in the  $F - \kappa$  plane.

The  $F - \kappa$  curve corresponds to viscous flow near walls, i.e. boundary layers, as well as free jets. Furthermore, adverse, zero or favorable pressure gradients are represented by positions on the  $F - \kappa$  curve. Heat addition in a supersonic flow generates compression waves. When  $z/r < 0$ , the compression waves impinge ahead of the base; the boundary layer on the body and the shear layer experience an adverse pressure gradient. When  $z/r > 0$ , the compression waves impinge downstream of the base and only the shear layer flows into the adverse pressure gradient established by the external burning. Since the  $F - \kappa$  curve incorporates pressure gradients, the presence of an adverse pressure gradient due to heat addition should not alter its validity. As stated in reference 8, the  $F - \kappa$  curve needs additional experimental verification; this applies to the case with external burning. Further discussion of the  $F - \kappa$  curve may be found in references 6, 12, 13, 14 and 15.

The reformulation of the Crocco-Lees theory for axisymmetric flow [Ref. 1,12-14] resulted in the same single ordinary



differential equation which had been derived for planar flow. In two dimensional planar flow this equation is numerically integrated by starting at the singularity, or so called critical point, and working toward the base, using the Prandtl-Meyer relation to obtain flow angle for various Mach numbers. With external heat addition, one may no longer use the Prandtl-Meyer relation for flow angle at the shear layer, since the heat addition, described by either linearized or one dimensional flow, introduces a correction term [Ref. 6,7].

This procedure cannot be used for the axisymmetric problem without heat addition due to the  $1/r$  term arising in the continuity equation; thus, one must start at the base and integrate toward the critical point. As was anticipated, attempts to numerically integrate through this saddle point singularity were unsuccessful; however, by repeated integration one may determine two Mach numbers on the downstream side of the expansion fan which straddle the saddle point singularity, thus establishing the base pressure within the limits given by the two Mach numbers, Fig. 4. This technique was used with Eqns. (5) and (6) for both axisymmetric and two dimensional planar flow.

To incorporate the effects of various boundary layers on the body (laminar, transitional, turbulent) and shear layer transition, it was necessary to formulate a transition model, Fig. 5. While this model treats the boundary layer mass flux differently, it is not a departure from the existing Crocco-Lees theory. In fact, this transition model extends the Crocco-Lees base flow model.



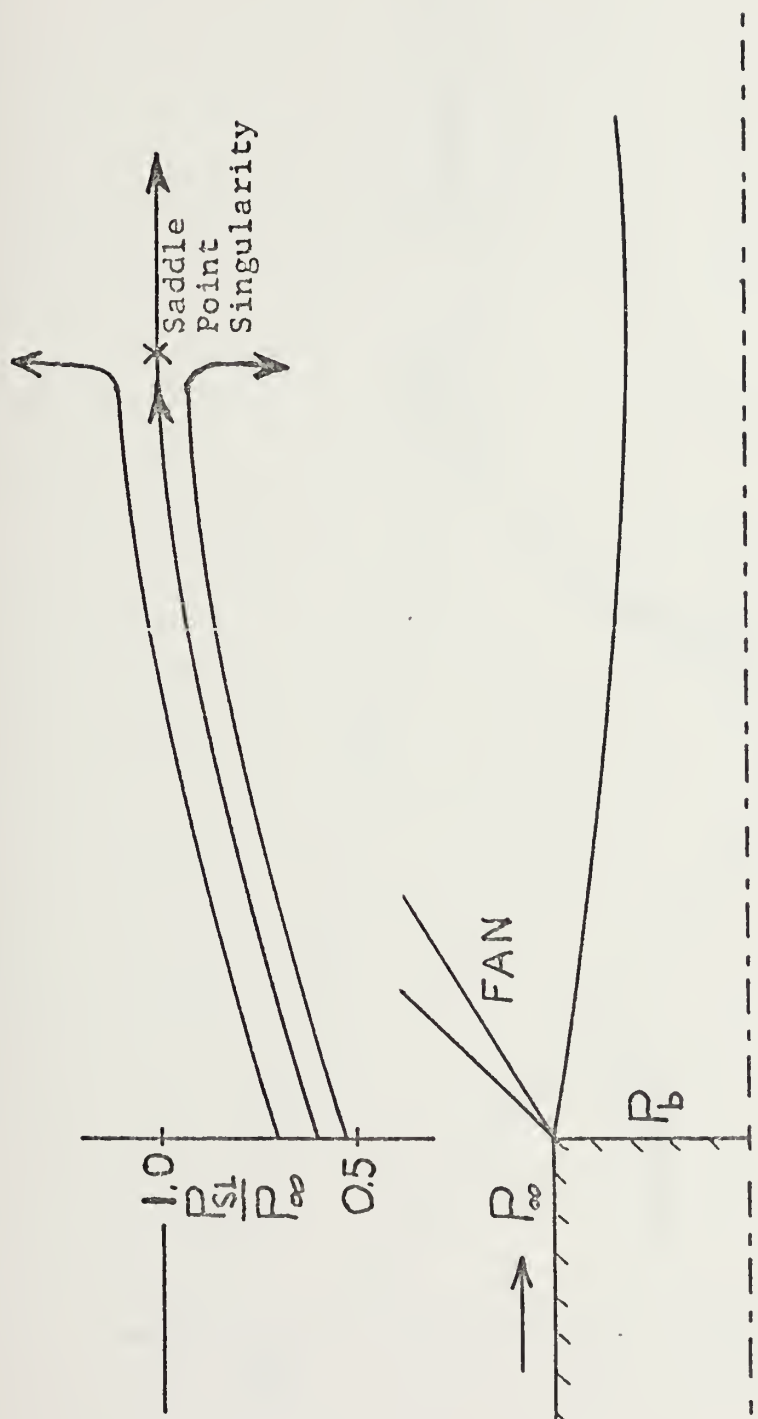


Figure 4. Conceptual Diagram Depicting Shear Layer Pressures,  $P_{SL}$ , Which Straddle the Critical Point





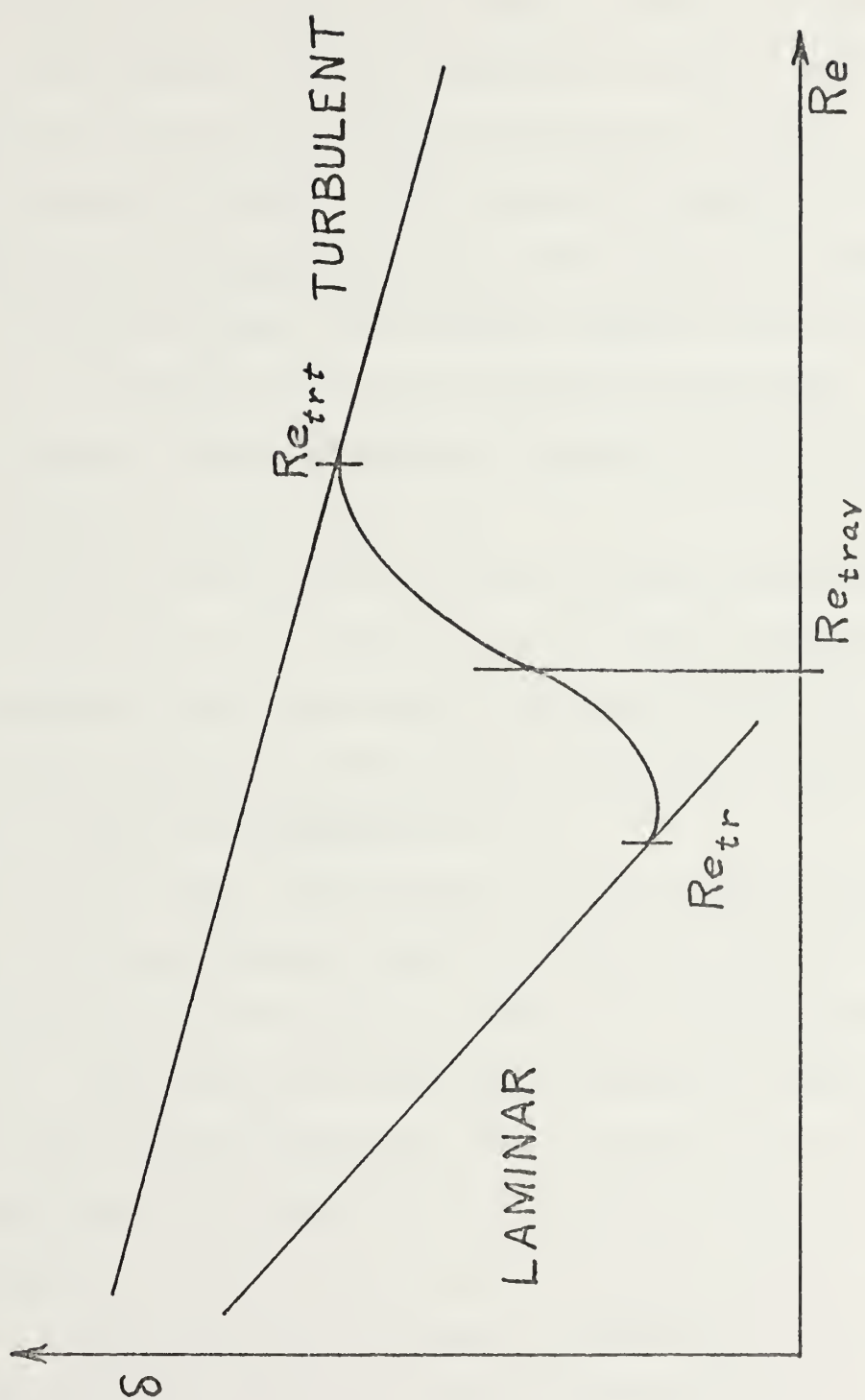


Figure 5. Transition Model



Since the transition from laminar to turbulent flow is more or less probabilistic in nature and, depending on the Reynolds number, may occur on the body or along the shear layer, it was assumed that the transition process could be described by an integrated normal distribution and two transition Reynolds numbers. The transition Reynolds numbers identified the start and end of the transition process, and the integrated normal distribution ranged from 0.02 to 0.98 in the span between the two specified transition Reynolds numbers. This assumption replaces the previously assumed transition curves [Ref. 8].

The transition model must provide several parameters which are required in the Crocco-Lees base flow formulation. It must establish the values for the mixing coefficient,  $k$ , along the shear layer and the boundary layer mass flux at the base to permit determination of  $F$ .

The boundary layer was assumed to be at constant static pressure and total enthalpy, and the velocity profile was assumed to have a  $1/n$  dependence, where  $n$  is an integer,  $1 \leq n \leq 7$ . This formulation may be integrated (Appendix D) for both planar and axisymmetric flows to give the boundary layer mass flux at the base as an explicit function of velocity profile,  $1/n$ , base radius,  $r_b$ , and boundary layer thickness,  $\delta$ . If the flow over the body is completely laminar,  $\delta$  is given by the compressible Blasius solution [Ref. 8],  $\delta_L = (5.0 + 1.2(\gamma - 1)M^2)L / (Re_b)^{1/2}$ , and the value of  $n = 1$  is used for the velocity profile [Ref. 24]. If the boundary layer is



completely turbulent, the  $n$  is taken as 7 and  $\delta$  is computed from the compressible one-seventh power solution [Ref 8],  $\delta_T = (0.037L/(\text{Re}_b)^{1/5})(C_{f_M}/C_{f_i})(\delta/\delta^{**})$ . The term  $(C_{f_M}/C_{f_i})$  is a ratio of skin friction coefficients for compressible and incompressible turbulent flow [Ref. 24]. It was recognized that the boundary layer thickness computed for planar flow will be different from the axisymmetric thickness. This difference will be small if  $\delta/r_b$  and radial velocity,  $v/U$ , are of order  $\epsilon$ . The dimensional term  $\rho v/r$  from the axisymmetric continuity equation will be of order  $\epsilon^2$  upon nondimensionalizing with  $\delta$  and  $U$ . Thus, the governing equations and their solutions are identical to order  $\epsilon$  in both cases.

The first transition Reynolds number,  $\text{Re}_{tr}$ , is where the laminar flow starts transition to turbulent. The second transition Reynolds number,  $\text{Re}_{trt}$ , is where the flow must be completely turbulent ( $\text{Re}_{trt} = 4\text{Re}_{tr}$ ). As one changes values of base Reynolds number from  $\text{Re}_{tr}$  to  $\text{Re}_{trt}$ , the values for  $n$  and  $\delta$ , which determine the boundary layer mass flux at the base, must vary from 1 to 7 and  $\delta_L$  to  $\delta_T$ , respectively. This transition was computed by the error function, erf, since it is readily available in FORTRAN and can be directly related to the integral of the normal distribution. A numerical span,  $S$ , of 4, which takes the value of erf from -0.96 to 0.96, was used to normalize the difference  $(\text{Re}_{trt} - \text{Re}_{tr})$ . Let  $\text{Re}_{tra} = \frac{1}{2}(\text{Re}_{tr} + \text{Re}_{trt})$ . Then

$$\text{ERF}_B = \frac{1}{2} \text{erf} \left( \frac{S}{2^{1/2}} (\text{Re}_{tra} - \text{Re}_b) / (\text{Re}_{trt} - \text{Re}_{tr}) \right). \quad (17)$$



So, when  $Re_b > Re_{tr}$

$$\delta_{BASE} = \delta_L(\frac{1}{2} + ERF_B) + \delta_T(\frac{1}{2} - ERF_B) \quad (18)$$

and

$$n_{BASE} = 1(\frac{1}{2} + ERF_B) + 7(\frac{1}{2} - ERF_B) \quad (19)$$

were the values used to compute the boundary layer mass flux at the base (Appendix F).

When transition from laminar to turbulent flow occurred on the shear layer, the value for the mixing coefficient,  $k$ , at a particular point was computed in a similar fashion using the error function to transition from laminar mixing,  $k_L$ , to turbulent mixing,  $k_T$ , Fig. 6.

The effect of shear layer mixing on base pressure is shown schematically in the momentum control volume of Fig. 7. The axial pressure on surfaces  $cd$  and  $de$ , and momentum flux leaving the volume,  $de$ , must be balanced by the pressure on surfaces  $ab$  and  $bc$  and momentum flux entering the volume,  $abcd$ . Thus, to maintain this balance, an increase of momentum flux along  $cd$  due to mixing requires a corresponding decrease of base pressure,  $p_b$ , along  $ab$ .

One additional assumption was necessary to obtain good agreement with experimental data. At low Reynolds numbers and completely laminar flow, it was necessary to increase the value of the laminar mixing coefficient,  $k_L$ , in direct proportion to the increase of the thickness of the boundary layer at the base. This assumption may be expressed as

$$k_L = k(Re_{tr}/Re_b)^{\frac{1}{2}} \quad (20)$$





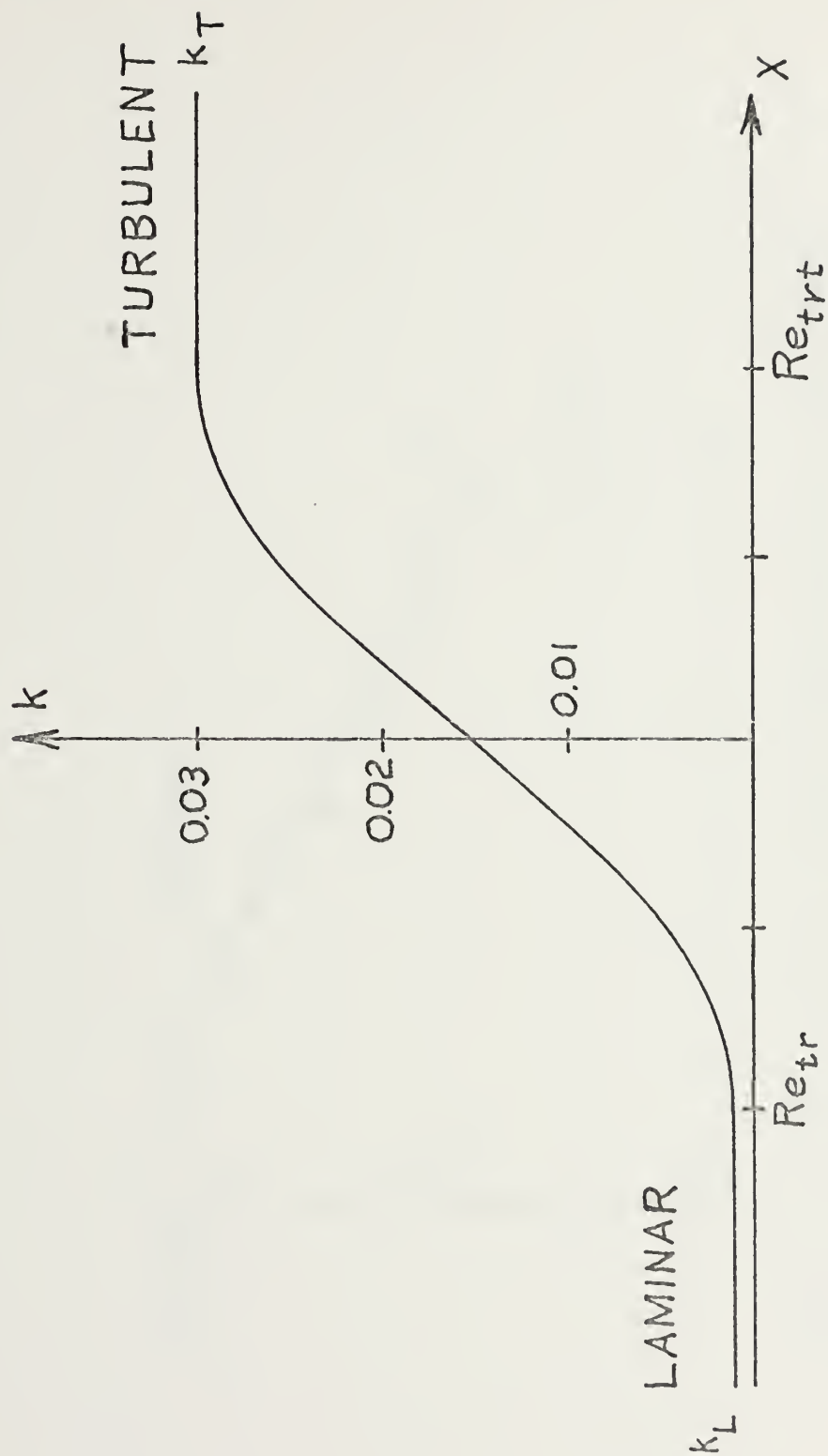


Figure 6. Transition of Shear Layer Mixing Coefficient



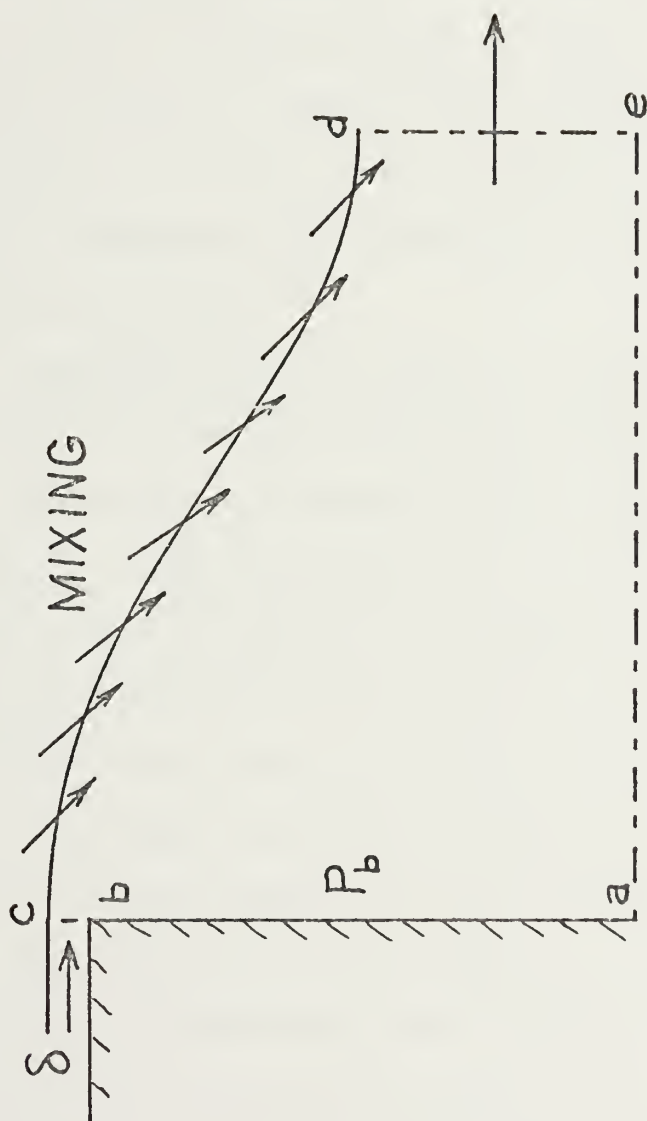


Figure 7. Momentum Control Volume Depicting Shear Layer Mixing



where  $Re_{tr}$  is the transition Reynolds number,  $Re_b$  is the Reynolds number of the body, based on length or chord,  $L$ , and  $k$  is the laminar mixing coefficient when  $Re_{tr} = Re_b$ . Some justification may be provided for Eqn. (20) by considering the Blasius boundary layer solution where the mass flux,  $\bar{m}$ , is given by  $3.28\rho u x / (Re)^{1/2}$  and the Crocco-Lees theory where  $k\rho u$  is taken equal to  $d\bar{m}/dx$ . If one forms the derivative of  $3.28\rho u x / (Re)^{1/2}$ ,  $d\bar{m}/dx$  is found to vary as  $1/(Re)^{1/2}$ , thereby suggesting the form assumed in Eqn. (20). Although  $k_T$  was held constant at 0.03 for all calculations, a similar analysis using the incompressible turbulent solution suggests that  $k_T$  might vary as  $1/(Re)^{1/5}$ .

It has been suggested that the effect of projectile spin could be included in the mixing coefficient [Ref. 15],  $k$ , by using  $k_{spin} = k(1+r\omega/U)$ , where  $r\omega/U$  is the spin number. However, since  $k_{spin}$  always increased with an increase in spin number, and, since it has been determined through numerical experiments with the Crocco-Lees theory, Fig. 8, that increasing  $k$  decreases the base pressure, this simple hypothesis contradicts experiment [Ref. 25,26] where, in some cases, increasing the spin number increased the base pressure. In Fig. 9 it is clear that at certain values of Reynolds number,  $Re_b$ , an increase of Reynolds number resulted in an increase in base pressure. This fact suggests that the spin number could be used to shift the  $p_b/p_\infty$  versus  $Re_b$  curve, Fig. 9, instead of increasing the mixing coefficient. Several methods were attempted at this point, such as increasing



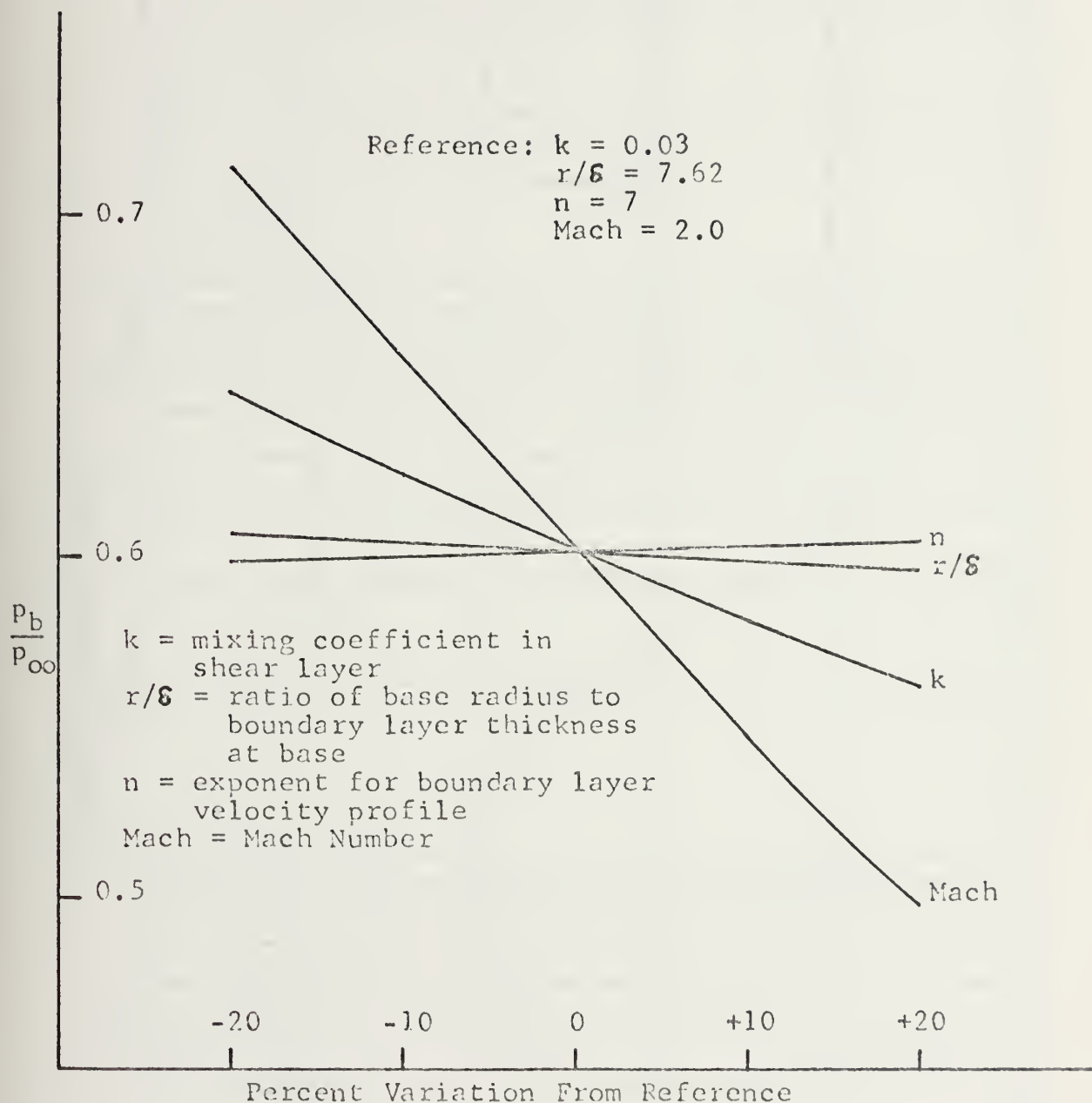


Figure 8. Sensitivity of Base Pressure Ratio





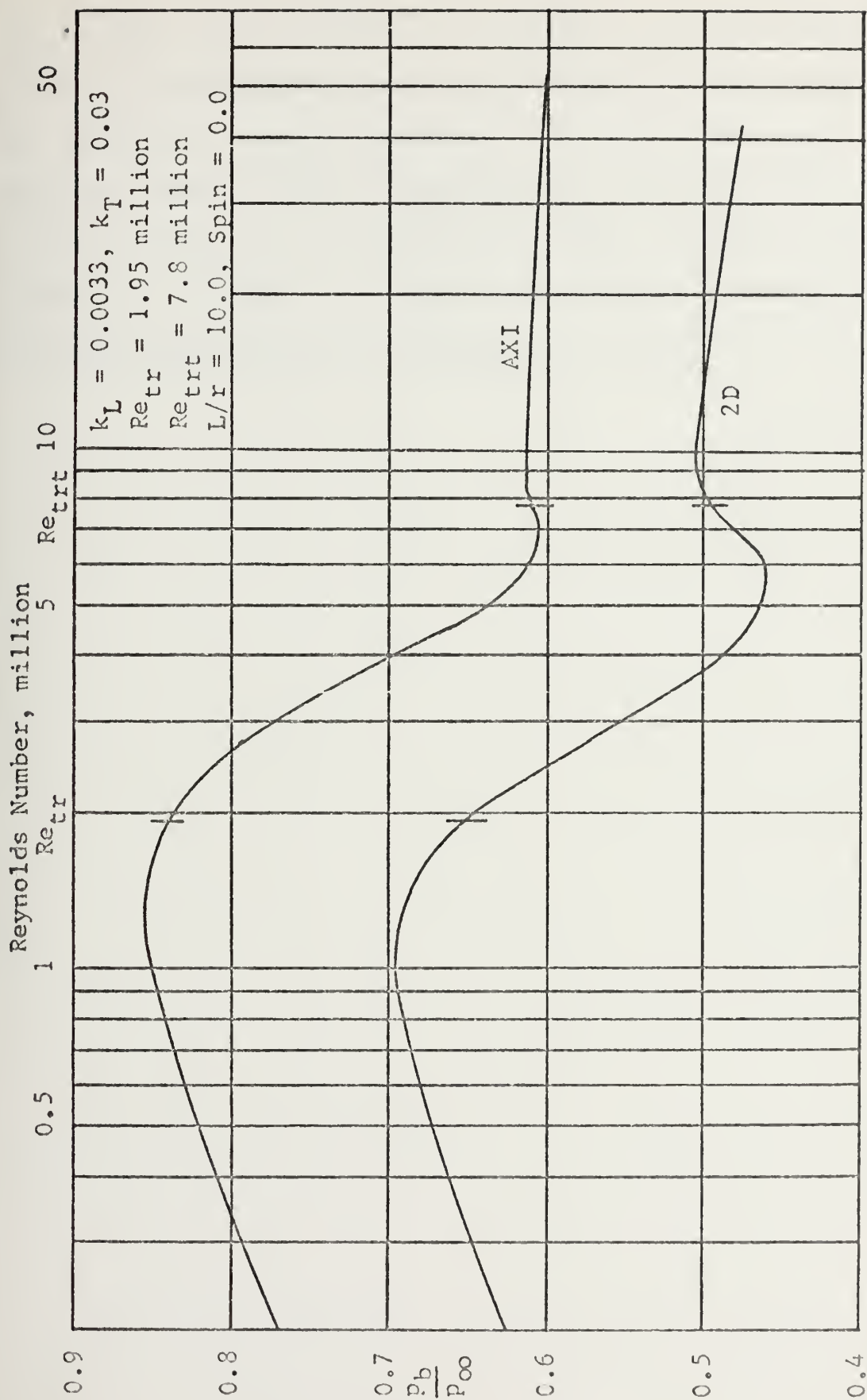


Figure 9. Computed Values of  $p_b/p_\infty$  vs. Reynolds Number, Mach 2.0, No Heat Addition



$Re_b$  by [Ref. 27]  $(1+(\frac{r\omega}{U})^2)^{\frac{1}{2}}$  or  $(1+(\frac{r\omega}{U})^2)$ , but the method which provided the best correlation was to simply decrease the transition Reynolds numbers. The spin transition Reynolds numbers used to compute  $p_b/p_\infty$  versus  $Re_b$  were formed by dividing the corresponding no spin transition Reynolds numbers by  $(1+(\frac{r\omega}{U}))$ . Interpretation of base pressure data for a spinning projectile is given in Section V.



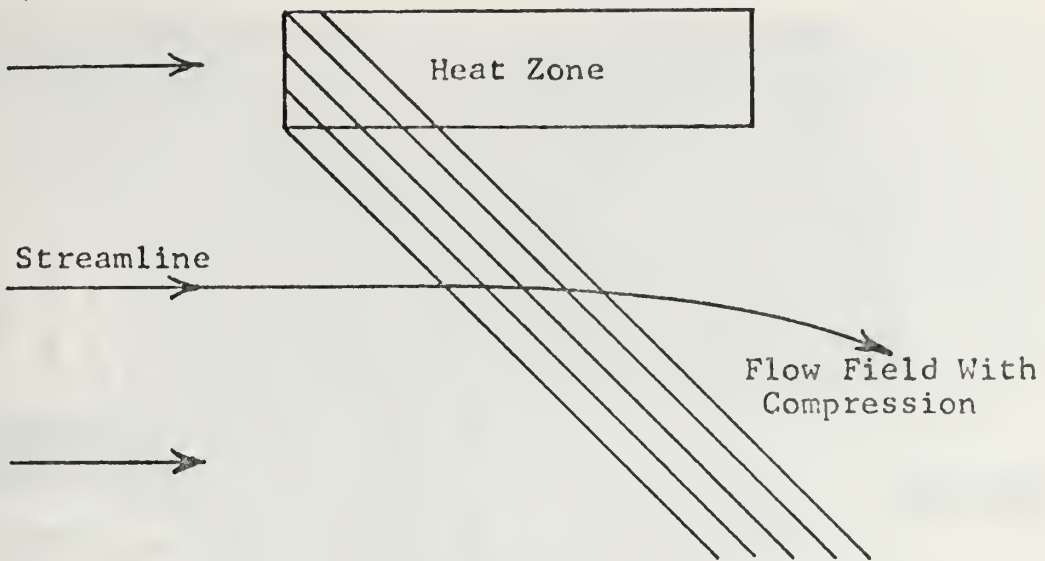
### III. EXPERIMENTAL INVESTIGATION

To carry out experiments related to the five inch projectile, the mid point of a maximum range trajectory was selected. This flight condition established an altitude of 23,000 feet and a Mach number of 2.0 for determining similarity parameters. For the five inch projectile, this gave a body Reynolds number of  $15.7 \times 10^6$ , a radius Reynolds number of  $1.51 \times 10^6$ , and a turbulent boundary layer thickness to radius,  $\delta/r$ , of 0.1313. The spin at 23,000 feet was assumed to be the same as the muzzle spin, 250 revolutions per second, which gave a spin number,  $r\omega/U$ , of 0.1595. Using these nominal values, it was found that all similarity parameters could be matched with a free jet Mach 2.0 coaxial nozzle exhausting at room pressure if the center cylinder had a radius of 0.641 inches,  $\delta$  of 0.084 inches, and a spin of 800 revolutions per second. As stated in the introduction, the actual combustion process was simulated with various nozzle contours which duplicated the compression waves generated by the external burning.

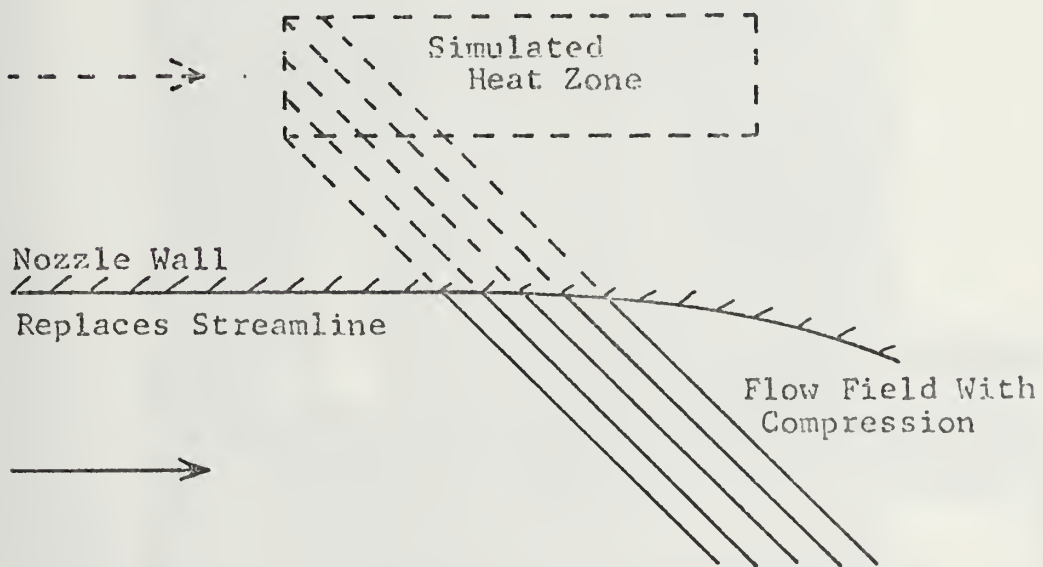
The simulation process is depicted in Fig. 10 where the streamline deflected by the presence of a heat zone can be replaced by a nozzle wall to generate an identical flow field.

The free jet experimental facility, Figs. 11 and 12, was conventional in most respects and has been previously reported [Ref. 28,29]. The use of cast aluminum filled epoxy





(a) Heat Zone in Supersonic Flow



(b) Identical Flow Field With Compression Generated by Nozzle Wall to Simulate Heat Zone

Figure 10. Heat Zone Simulation With Nozzle Wall

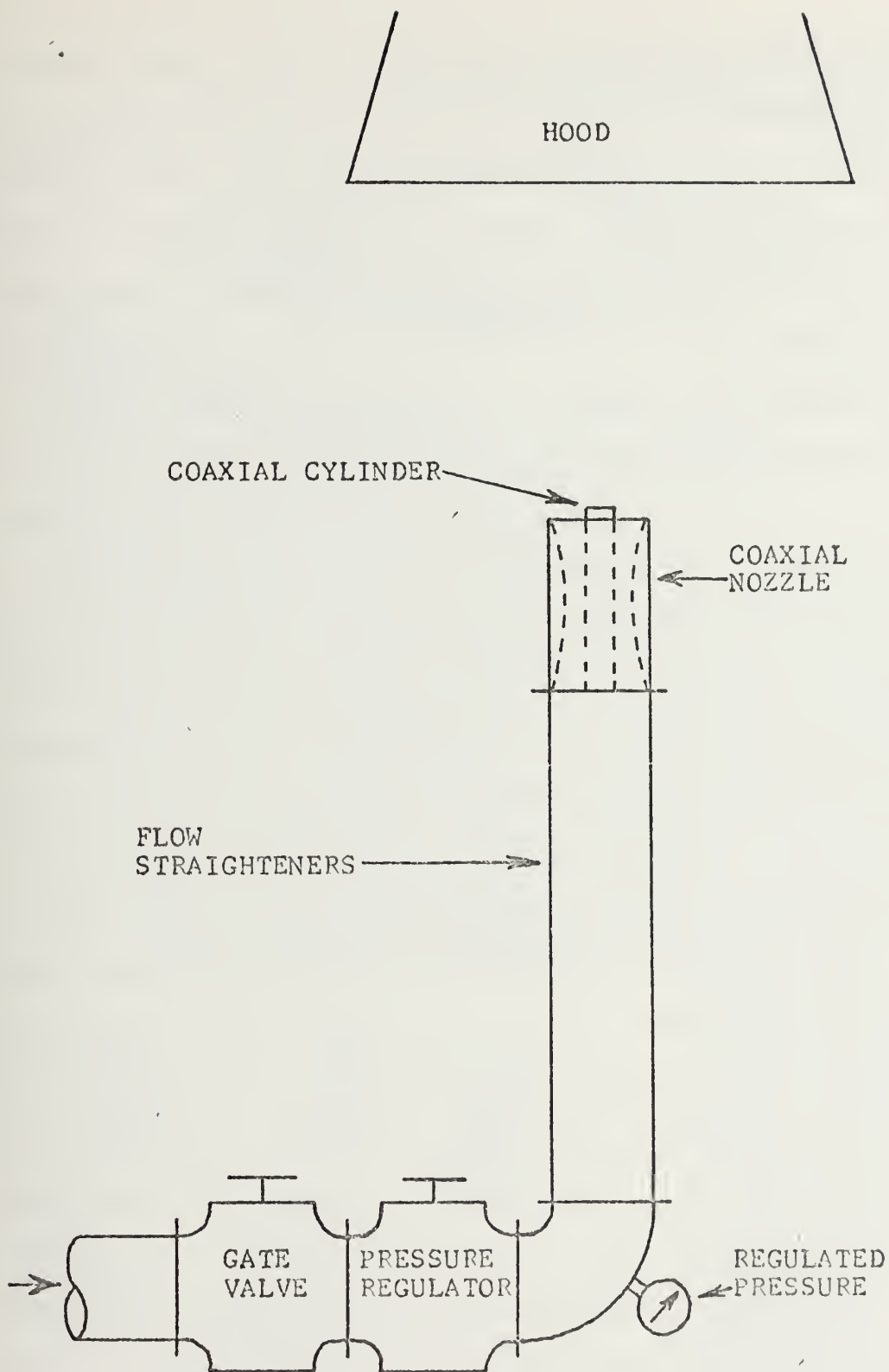






Figure 11. Photograph of Free Jet Experimental Facility





• Figure 12. Schematic Diagram of Free Jet Experimental Facility





nozzles, Fig. 13, was the only new hardware innovation. The technique of casting employed a wax plug contoured to the desired shape with an aluminum template. This plug was turned slightly undersize and then restored to size using a thin coat of automotive body plastic. After melting the wax from the cast nozzle, the plastic peeled away from the epoxy to leave a smooth nozzle wall. Without this plastic, the heat generated by the epoxy had softened the wax and caused some irregularity in the nozzle wall.

The location of the zone of combustion to be simulated by the nozzle was estimated using an empirical formula for penetration depth of a jet normal to a supersonic free-stream [Ref. 30]. For Mach 2.0 flow, internal pressures from 300 to 500 psia were computed to provide penetration to  $2\frac{1}{2}$  inches with various orifice diameters. Thus it was assumed that external burning at 5 inches from the projectile centerline would be practical. Assuming a fuel rich propellant exhaust, ARC-168, with an available heating value of 7200 BTU/lb and 0.6 lb/sec flow rate, it was found using one dimensional theory that the flow should be deflected about  $4\frac{1}{2}^\circ$  for a distance of 15 inches, or three diameters, downstream. This computation used the integral methods of reference 5 which gave a perturbation velocity normal to the flow of -163 feet per second. The resulting flow angle tangent was  $-163/2058$ , which gave a computed flow angle of -4.54 degrees along the inner streamline of the heat zone.



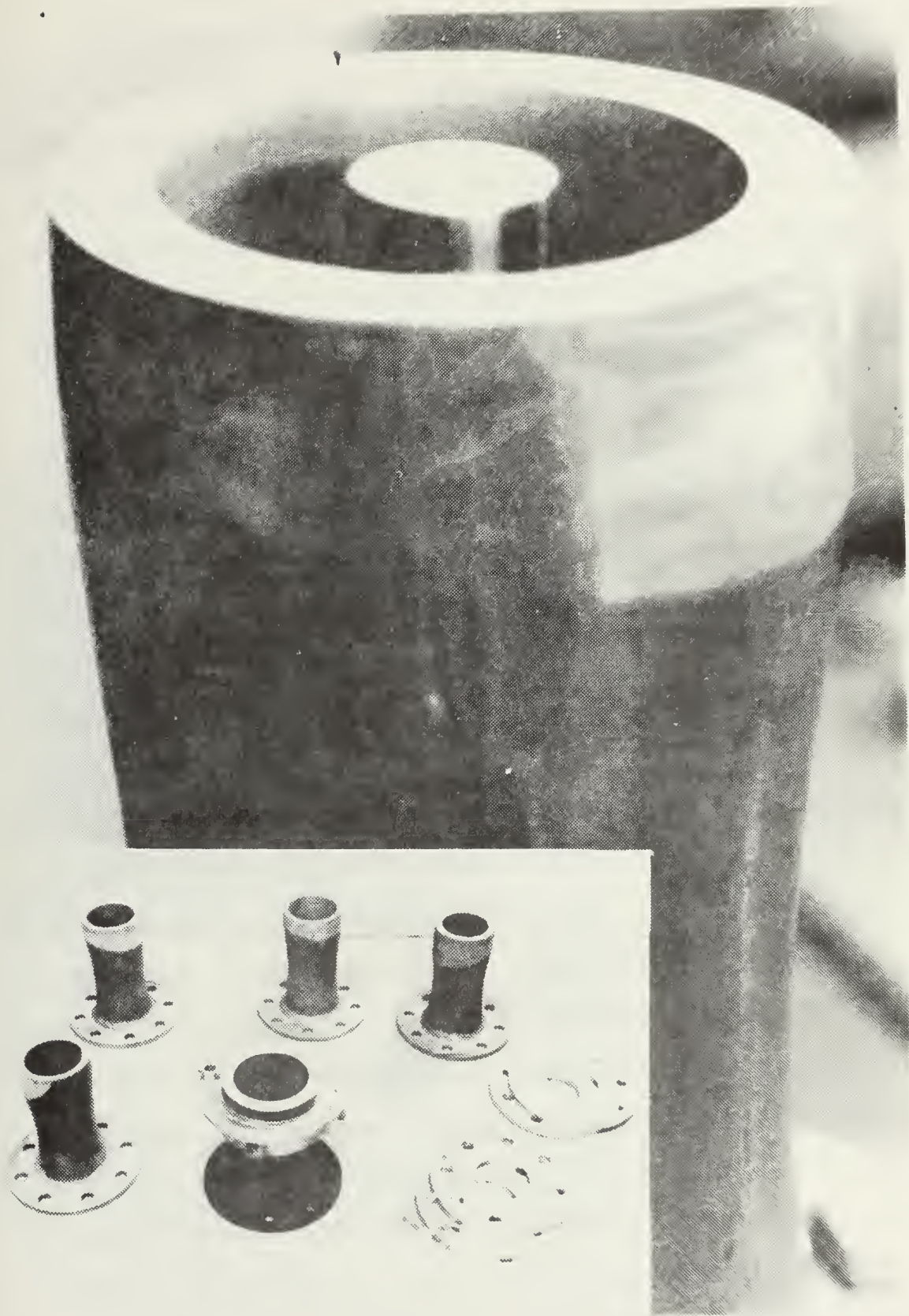


Figure 13.Coaxial Epoxy Nozzle. Insert Showing Spacers.





These estimated values for the heat zone were taken as the upper limit and were used to form a test matrix and for subsequent nozzle design. Several different nozzle contours were computed by the method of characteristics for  $4\frac{1}{2}^\circ$  streamline deflection at a radius equal to a cylinder diameter from the centerline and with different assumed lengths for the combustion zone. The test matrix included using spacers, Fig. 13 insert, with each nozzle so that the first full compression waves impinged ahead of, at, or behind the base of the cylinder. Pressures were measured along the base and side of a stationary centerline cylinder, Fig. 13, using mercury manometers. Attempts to carry out experiments with a spinning cylinder were unsuccessful due to faulty air bearing design (Appendix I). Time did not permit correction of this difficulty.

The differences in the flow field with the stationary cylinder and different nozzles can be seen in Fig. 14. The photograph of the uniform flow nozzle in Fig. 14a used a horizontal knife edge and the expansion fan at the base appears dark. The base pressure ratio was 0.635. In Fig. 14b the vertical knife edge was positioned to make a positive density gradient from the centerline to the right appear brighter. The flow with compression, Fig. 14c, had an expansion fan at the base but achieved a higher base pressure ratio of 1.065 due to compression upstream of the base as well as along the shear layer. The compression upstream of the base increased the pressure right before the expansion





Figure 14a.  
Uniform Flow,  
Horizontal  
Knife Edge



Figure 14b.  
Uniform Flow,  
Vertical  
Knife Edge

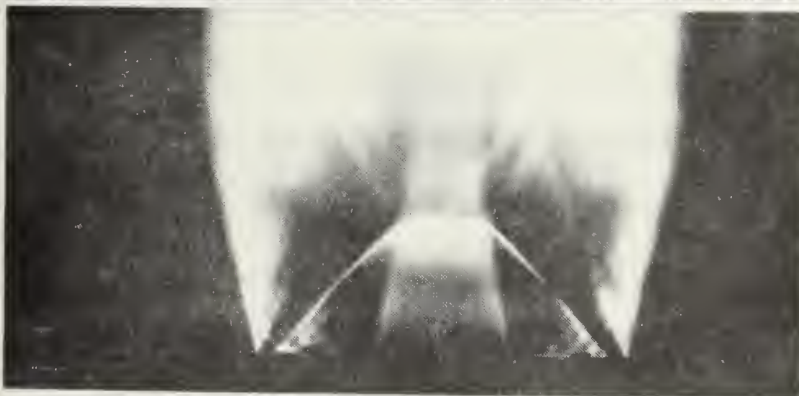


Figure 14c.  
Compression Flow,  
Horizontal  
Knife Edge

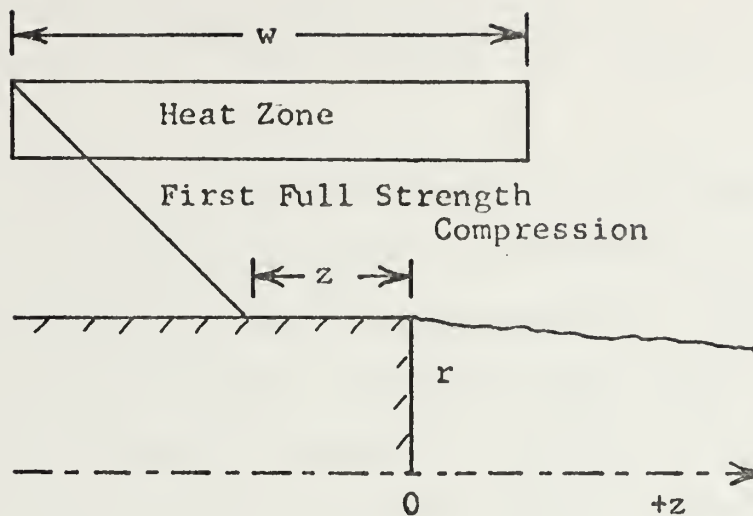
Figure 14. Schlieren Photographs at Mach 2.0 Showing  
Uniform Flow and Flow With Compression



fan, so that it was greater than  $p_\infty$ , thus the flow was near ambient pressure after passing through the expansion fan. Some test results using the stationary cylinder are given in Table I. Except for the nozzle with  $w/r = 4.34$ , these tests indicate that compression applied upstream of the base,  $z/r = -0.5$ , is less efficient at increasing base pressure than compression applied at the base, or slightly downstream. The nozzle with  $w/r = 4.34$  had a strong shock wave at the exit, due to compression waves reflected from the cylinder [Ref. 15], which, with  $z/r = -0.5$ , impinged on the base flow region ahead of the critical point. In turn, increased pressure across the shock wave was impressed on the subsonic flow in the recirculating zone and gave a higher base pressure. The shock wave observed with this experimental nozzle would not be expected with uniform external burning.

In Table I the experimental base pressure ratios,  $p_b/p_\infty$ , are shown as the upper number in each box for the various test positions,  $z/r$ , of each nozzle,  $w/r$ . The cylinder radius is  $r$ , the axial location where the first full strength compression wave impinges on the body or shear layer is  $z$  ( $z=0$  at the base) and  $w$  is the length of the heat zone. The corresponding Reynolds number,  $Re_b$ , is shown below each value of  $z/r$ . The lower number shown in each box is the computed specific impulse for the assumed projectile flight condition at 23,000 feet. The uniform flow nozzle, with  $w/r = 0.0$ , was taken as the reference pressure ratio to compute the





Sketch to Table I

$z/r \rightarrow$	-0.5	0.0	0.5	1.0
$Re_b \times 10^6 \rightarrow$	8.55	7.80	7.05	6.29
$w/r \downarrow$				
0.0	0.62	0.61	0.60	0.60
0.72	0.759 227	0.893 460	0.993 639	----
1.84	0.96 216	1.055 283	1.074 302	----
3.91	1.078 137	1.175 169	1.160 167	1.129 158
4.34	1.20 156	1.14 143	1.085 131	----

Table I. Base Pressure Ratio and Specific Impulse With Simulated Heat Addition





base pressure force created by the other nozzles. The fuel flow rate was taken proportional to  $(w/r)/(6.0)$ , since 6.0 was the combustion zone length assumed for the fuel flow of 0.6 lb/sec.

Once Mach number and operating pressure and temperature are selected, the remaining variable controlling Reynolds number is the length or scale of the apparatus. The free jet facility of Figure 11 has sufficient mass flow to permit duplication of Reynolds number at 23,000 feet altitude provided the cylinder has sufficient length. Consequently the nominal Reynolds number was chosen as  $15.7 \times 10^6$  for 23,000 feet to match capability of the facility.

When the design of the spinning cylinder was initiated it became apparent that a long cylinder had problems in regard to shaft whip or the first vibrational mode in bending. A shorter cylinder reduced the Reynolds numbers to the values shown in Table I. Conditions at a higher altitude were simulated, or else conditions for a short projectile at 23,000 feet were duplicated.

Two cylinders could have been designed. Each cylinder would have required a separate family of nozzles. A choice was made to use a short cylinder for both stationary and spinning tests.

Variation in  $z/r$  as shown in the sketch with Table I changes Reynolds number slightly. The variation in  $Re_b$  in Table I is due to this fact.



#### IV. NUMERICAL INVESTIGATION

The computer program for this numerical investigation was written to calculate either two-dimensional planar or axisymmetric problems. The program used the method of characteristics where the axisymmetric term in Eqns. (5) and (6),  $r_b(\sin\mu\sin\theta)/r$ , was deleted for two-dimensional planar flow. Similarly, the effect of radius in the mass flux calculation, at the base and along the shear layer, was deleted or retained as required. The characteristic mesh, Fig. 15, was computed from the body or shear layer upstream through the heat zone, if present, to a reference freestream Mach line (i.e., backwards along a right running  $\xi$  characteristic). The error from the reference condition was used to correct  $v$  on the body, since  $\theta$  was given, or  $\theta$  along the shear layer since  $v$  was computed from the Crocco-Lees theory. Each body or shear layer point was iterated until the error at the upstream boundary condition was less than  $10^{-3}$  radians. At each point in the characteristic mesh, the value of  $\mu$  was determined for the resulting value of  $v$  by the method given in Appendix H. In retrospect, this method of characteristics computation could be made more efficient if one could devise a scheme which works with arbitrary points along the body or shear layer and increments the characteristic mesh along the reference freestream Mach line. Then only one calculation would be required along each characteristic, rather than the







iterative scheme used in the present method. This approach was considered, but it was not clear how one would formulate the calculation for the corner or the shear layer mass influx (Appendix E).

The flow field was calculated along the body to the base at which point all computed values along the last characteristic were stored. These values were used to reset the flow field for each iteration of the straddle method.

The Crocco-Lees theory was formulated in terms of  $w_e$  instead of Mach number, where  $w_e$  is the velocity at the edge of the shear layer divided by the freestream stagnation speed of sound,  $w_e = U/a_s$ . To start the straddle method a value of  $w_e$  was chosen for the downstream side of the expansion fan which was too large. The expansion fan was divided into ten parts; downstream of the fan the computation proceeded toward the critical point. Each new point along the shear layer, computed by the Crocco-Lees theory (Appendixes C, E and F), required several iterations along the characteristic to the upstream Mach line boundary condition, where the flow angle error after each iteration was used to correct the shear layer flow angle.

Integration in the  $F - w_e$  plane followed the first path shown in Fig. 16. It can be seen that this path falls to the right of the path passing through the saddle point singularity,  $x$ , and, as the value of  $F$  was decreased, the slope,  $dF/dw_e$ , became negative at 1'. This occurred when the denominator used to form  $dF/dw_e$  became positive [Ref. 8], i.e. both the numerator and denominator of  $dF/dw_e$  were





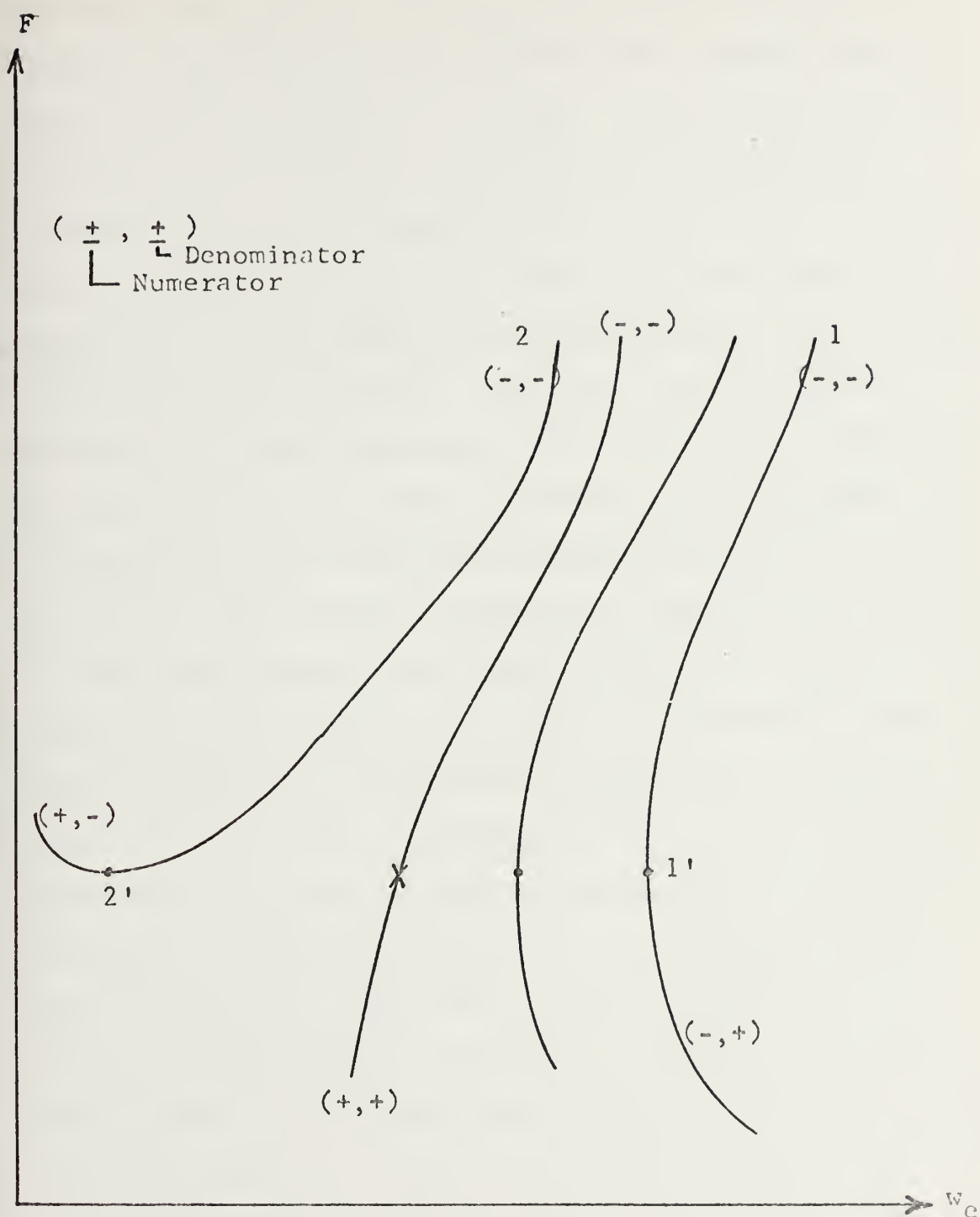


Figure 16. Integration in the  $F - w_e$  Plane



negative from 1 to 1'. This transition from positive to negative slope with positive denominator occurred when the initial guess for  $w_c$  was too large. By systematically decreasing the initial guess for  $w_c$ , say by tenths, one eventually has the integration path from 2 to 2', which is similar to the previous case, except that the negative slope at 2' is associated with the numerator, used to form  $dF/dw_c$ , becoming positive. Thus, the last two initial guesses for  $w_c$  have straddled the saddle point singularity. The interval between these two values may be divided, say in hundredths, and the process repeated to find two values of  $w_c$  which more closely straddle the saddle point singularity.

The heat zone was specified to start and stop at certain values of axial position,  $z$ , and to lie between an inner and outer streamline. The quantity  $r_b q/Uc_p T$  was assigned a constant numerical value, between 0.15 and 0.175, within the zone, which gave the desired  $-4\frac{1}{2}^\circ$  deflection to the inner streamline. External to the heat zone  $r_b q/Uc_p T$  was zero. Before deflection, the inner and outer streamlines have values of approximately 2.0 and 3.0, maximum body radius, respectively. These values were chosen to match the rate of compression increase used in the nozzle design. As the computation proceeded downstream, the values of radius and flow angle for the inner and outer streamlines were computed to insure realistic boundaries for the heat zone.

When a sufficient amount of properly located heat was added to the external flow, the base pressure ratio was



computed to be greater than 1. It is interesting to note that for this condition the method of characteristics routine generated a compression fan at the base, rather than the usual expansion fan. The compression fan calculation mathematically folds the flow field on itself [Ref. 31]. This of course is physically impossible and is replaced in real flow by an oblique shock. For values of  $p_b/p_\infty = 1.5$  at Mach 2.0, the loss of total pressure due to the oblique shock is less than 1%, which corresponds to an entropy increase,  $\Delta S/R$ , of 0.01. This resulted in an error of less than  $0.18^\circ$  in the turning angle, which was neglected. There is also the possibility of boundary layer separation upstream of the base for values of  $p_b/p_\infty$  greater than one [Ref. 7]. This effect was not considered in the calculations. The computer program is discussed in Appendix J.



## V. DISCUSSION OF RESULTS

The computed values of  $p_b/p_\infty$  versus  $Re_b$ , shown in Fig. 9, were based on the apparent transition Reynolds numbers from the uniform flow nozzle experiments. These were  $Re_{tr} = 1.95 \times 10^6$  and  $Re_{trt} = 7.8 \times 10^6$ . The curves display the same general features and approximate values found from experiment [Ref. 32-35]. It should be noted in Fig. 9 that for both the two dimensional planar and axisymmetric flow the maximum value of  $p_b/p_\infty$  occurred below  $Re_{tr}$  and the minimum value of  $p_b/p_\infty$  occurred below  $Re_{trt}$ .

A slightly different choice of transition Reynolds numbers,  $Re_{tr} = 1.5 \times 10^6$  and  $Re_{trt} = 6.0 \times 10^6$ , resulted in the curve of  $p_b/p_\infty$  versus Reynolds number shown in Fig. 17. One may compare the curves of  $p_b/p_\infty$  in Fig. 9 and Fig. 17 with the experimental curves shown in Fig. 18. While the curves are by no means identical, they do agree in having the same general shape. Figure 19 shows additional experimental data to compare with Fig. 9. The locations of maximum and minimum computed  $p_b/p_\infty$  are controlled by the choice of values for  $Re_{tr}$  and  $Re_{trt}$ . The ratio of  $\frac{1}{4}$  for  $Re_{tr}/Re_{trt}$  used in these computations was based on information in reference 8. This ratio is an approximation which varies considerably for different bodies, depending on their shape and surface condition. The maximum value of  $p_b/p_\infty$  was controlled by the choice of  $k_L$ , while the choice of  $k_T$  controlled the second





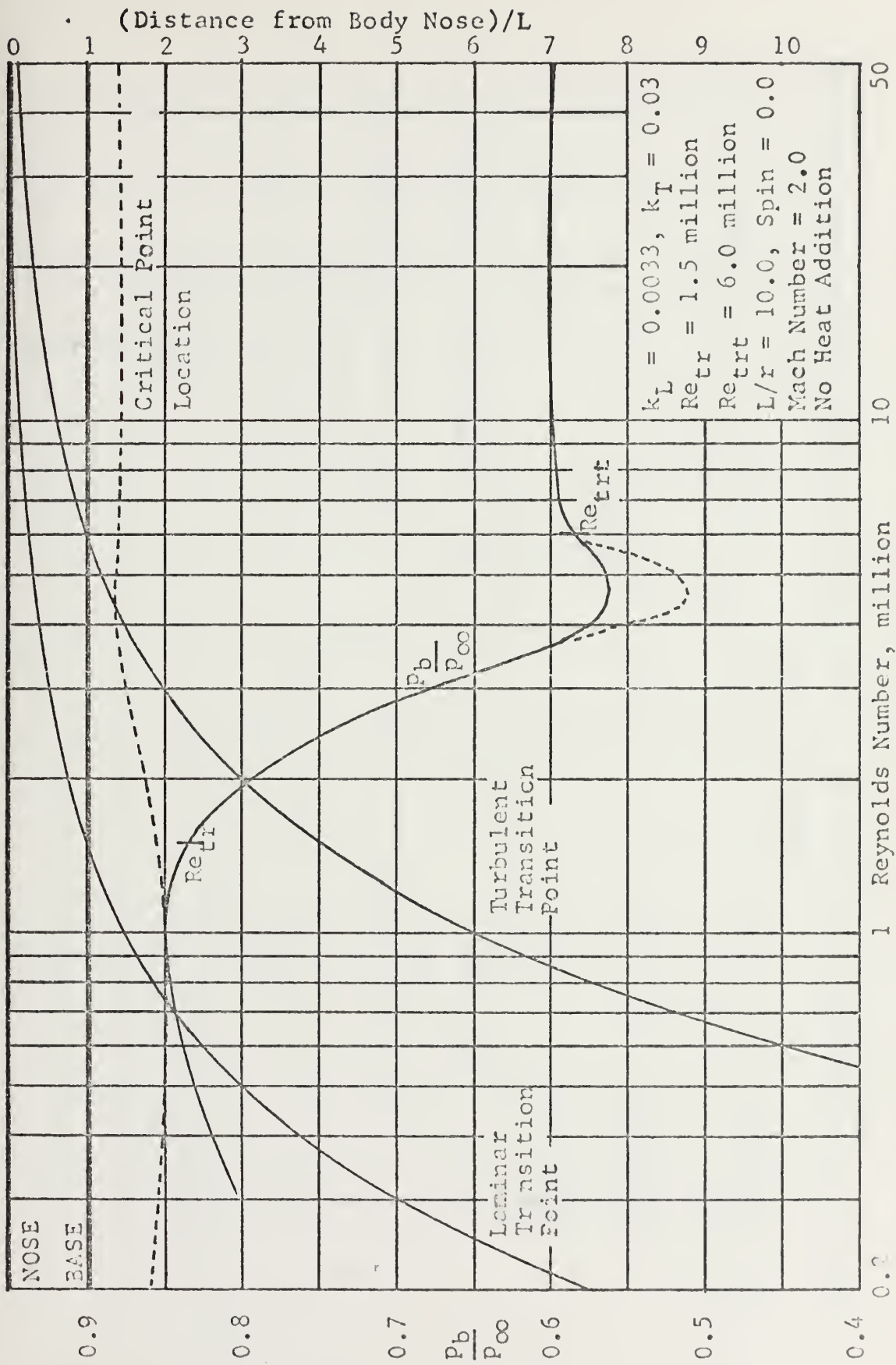


Figure 17. Computed Values of  $P_b/P_\infty$ , Transition Points and Critical Point



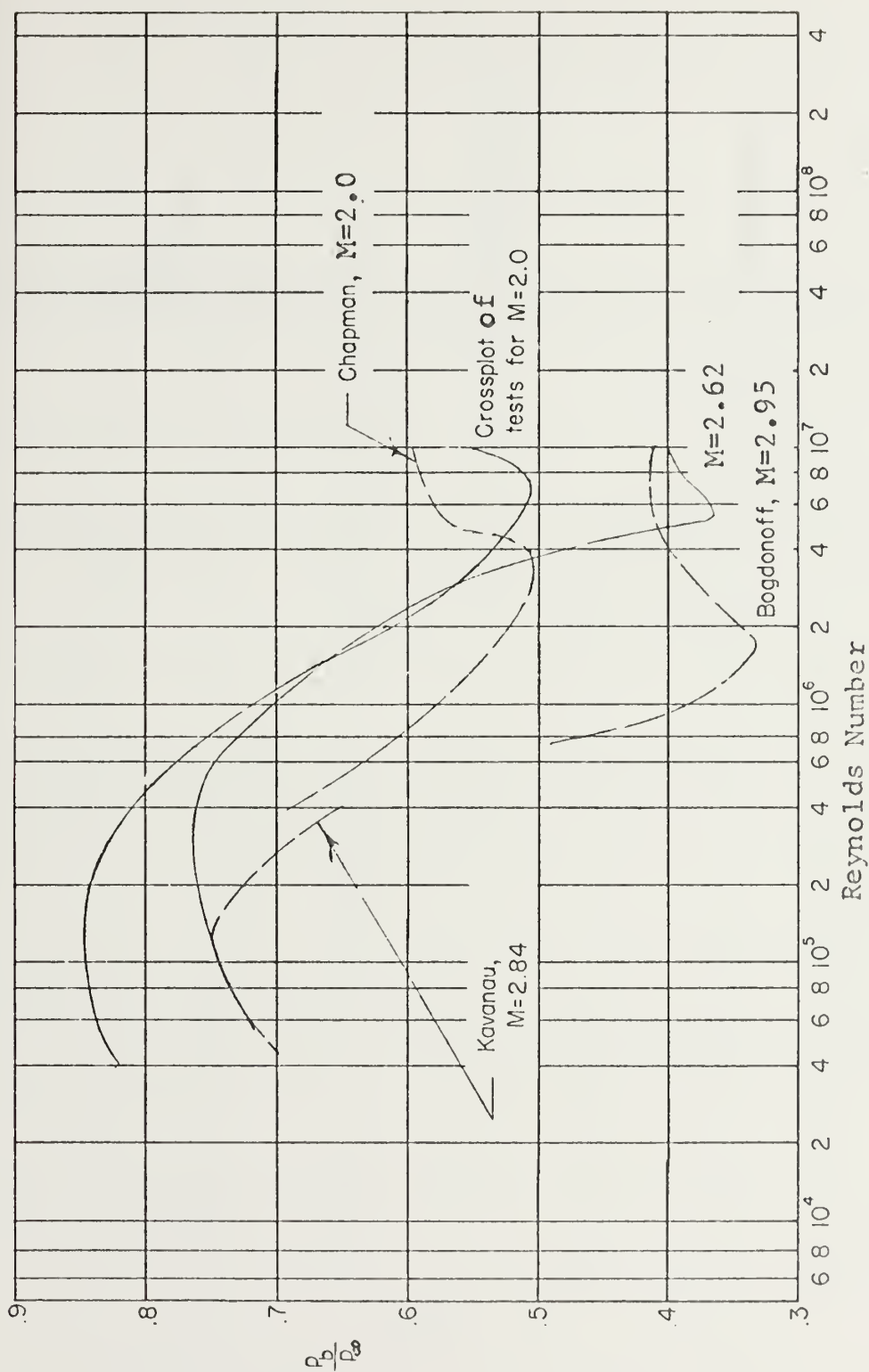


Figure 18. Experimental Values of  $p_0/p_\infty$  vs. Reynolds Number Without Heat Addition, from Ref. 32.



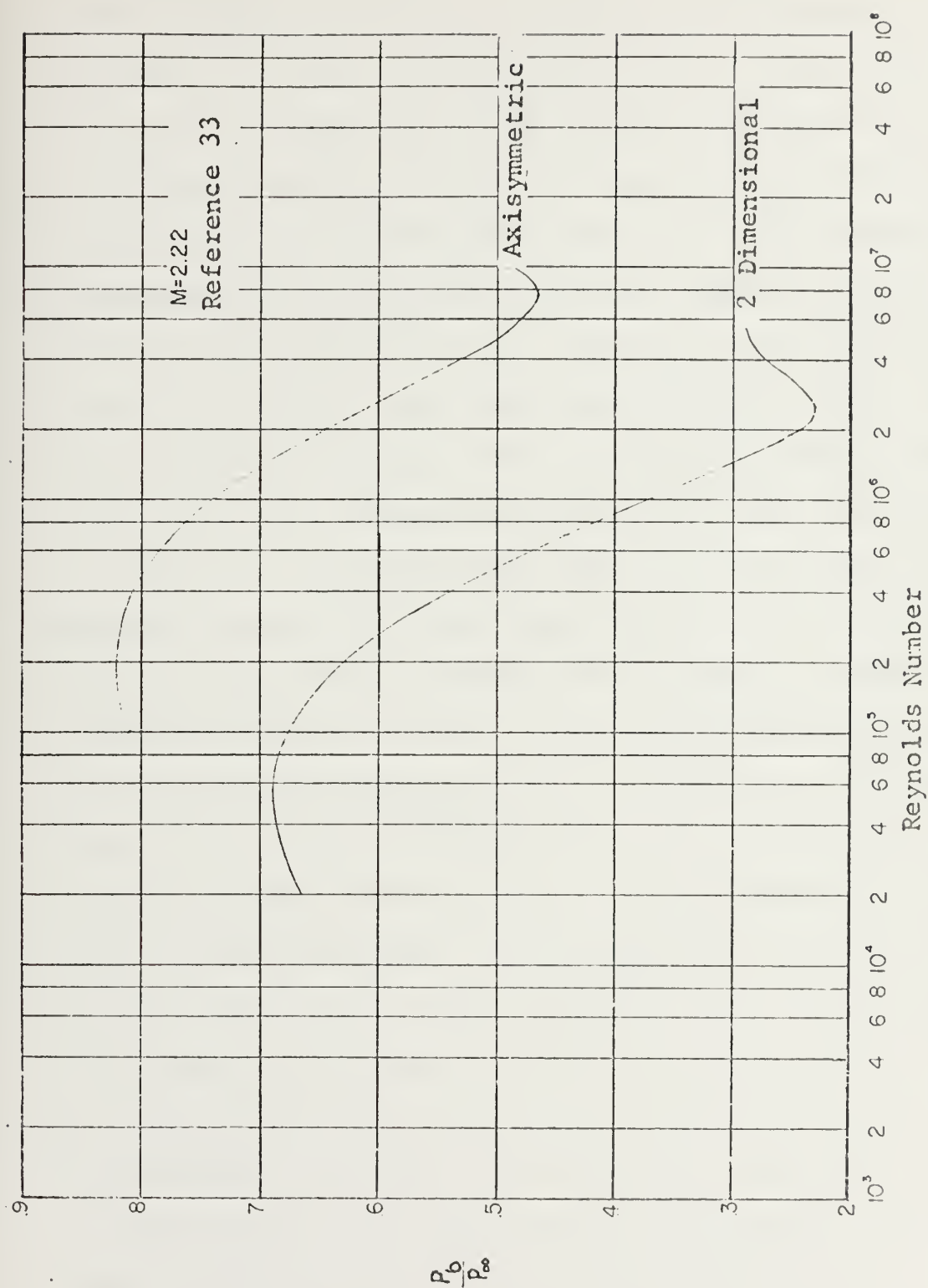


Figure 19. Experimental Values of  $p_0/p_\infty$  vs. Reynolds Number Without Heat Addition



maximum value of  $p_b/p_\infty$  to the right of  $Re_{trt}$ . The slight decrease of  $p_b/p_\infty$  to the right of this second maximum is in agreement with the  $r/\delta$  sensitivity curve of Fig. 8, since increasing  $Re$  decreases  $\delta$  and therefore increases  $r/\delta$ .

Three additional curves are shown in Fig. 17; these are transition and critical point locations. The laminar and turbulent transition points are found simply by dividing base Reynolds number into  $Re_{tr}$  and  $Re_{trt}$ . The critical point location was taken from calculation with the Crocco-Lees equations along the shear layer where  $dF/dw_e$  changed signs; it is the singularity in Fig. 16 which was discussed in Section IV. In going from small to large values of Reynolds number, the shear layer between the critical point and the base gradually changes from completely laminar to completely turbulent as the laminar and turbulent transition points move upstream to the base and then onto the body. Where this occurs, the shear layer mixing coefficient,  $k$ , gradually changes from  $k_L$  to  $k_T$ . Increasing from some small value of Reynolds number, the thickness of the laminar boundary layer at the base decreases until the laminar transition point reaches the base and moves onto the body. As the boundary layer at the base transitions to turbulent its thickness increases. The thickness continues to increase as the turbulent transition point moves forward along the body, reaching a maximum when the transition point is near the nose of the body. Beyond this point, the thickness decreases.





In Fig. 17, the value of  $p_b/p_\infty$  starts to decrease slightly before reaching  $Re_{tr}$ , while the laminar transition point is still on the shear layer and the base boundary layer is laminar. Although the boundary layer thickness is still decreasing at this point and in turn should provide an increase in  $p_b/p_\infty$ , the value of  $k$  along part of the shear layer (between the laminar transition point and the critical point) starts to increase from  $k_L$  to  $k_T$  and consequently dominates the overall change in  $p_b/p_\infty$  with Reynolds number.

The mechanism responsible for the abrupt minimum value of  $p_b/p_\infty$  in Fig. 18 was not clear. However, this minimum was calculated and is shown in Fig. 17 as a dashed line. From the sensitivity curve in Fig. 8, it appeared that  $k$  would be most likely quantity responsible. In numerical experiments this abrupt minimum was calculated by assuming additional mixing. The additional mixing was assumed to have a normal distribution about  $Re_{trt}$ , i.e.  $k = k_T(1 + (e^{-x^2/2})/(2\pi)^{1/2})$ . The argument,  $x$ , was adjusted so that the additional mixing fell to about ten percent of its maximum value in  $2 \times 10^6$  either side of  $Re_{trt}$ . This additional mixing was not used in any other calculations since it was not understood and was not clearly observed in the experimental data reported later in this section.

Calculations were made for external heat addition in two dimensional planar flow to compare with Strahle's previously reported calculations [Ref. 7]. The values of  $Re_{tr} = 1.95 \times 10^6$  and  $Re_{trt} = 7.8 \times 10^6$  were assumed and a



Reynolds number of  $Re_b = 20.0 \times 10^6$  gave the same value of  $\delta/r$  used by Strahle. The Mach number was  $M = 2.3$ . The heat addition zone was started at the same point,  $z/r = 0.4$ , and assigned the same length,  $w/r = 3.0$ , but to avoid subsonic flow with the method of characteristics it was necessary to increase the height of the heat zone from the value of  $0.2r_b$  used by Strahle to a value of one base radius. The values of  $Q = r_b q / U c_p T$  were reduced accordingly to provide the same total heat addition based on the rectangular heat zone used by Strahle, i.e.  $Q = 0.2\eta / \tan\mu$ . The results in Table II show good agreement at the low intensity of heat addition, but only fair agreement at the higher intensities with the method of characteristics program showing higher values of  $p_b/p_\infty$ . Although the non linearity included in the method of characteristics calculation may be responsible for part of the higher base pressure ratio, the main cause was attributed to expansion of the heat zone. This effect was included in the bounding streamline calculation for the heat zone in the method of characteristics program and resulted in a greater amount of total heat added than in the linearized theory calculations.

Linearized Theory <sup>[7]</sup>		Method of Characteristics	
$\eta$	$p_b/p_\infty$	$Q$	$p_b/p_\infty$
0.0	0.420	0.0	0.410
0.4	0.657	0.167	0.669
0.8	0.900	0.334	1.075
1.2	1.158	0.5	$1.45 \pm 0.02$

Table II. Comparison of Calculated Base Pressure Ratio with External Heat Addition, Two Dimensional Planar Flow and Mach Number of 2.3.



Both experimental and calculated results are shown in Fig. 20 for a Mach number of 2.0. The value of  $p_b/p_\infty = 0.6314$  at  $Re_b = 10.4$  was the average of nine runs with the uniform flow nozzle. The probable error about this average was  $\pm 0.004$ , with a maximum observed deviation of  $- 0.0104$ . In comparing the experimental values of Fig. 20 and Table I with early test results using the free jet, variations as high as 7% in  $p_b/p_\infty$  were found for similar runs. These variations were attributed to problems, such as mechanical alignment during nozzle installation or leaks in the manometer tubing, which were found and corrected during subsequent testing.

Early test data were rejected and were not reported herein. As experience was gained with operation of the facility, the 7% variations were narrowed to less than  $3\frac{1}{2}\%$ .

Cylinder wall temperatures were also recorded during these nine runs using a thermocouple imbedded in the wall,  $1\frac{1}{2}$  inches from the base. These temperatures ranged from  $5^\circ\text{F}$  to  $35^\circ\text{F}$ . A plot of  $p_b/p_\infty$  versus temperature showed no correlation scatter in  $p_b/p_\infty$  due to temperature was less than 1.4%. Since the stagnation temperatures of the air supply were not recorded, they could not be compared with the cylinder wall temperatures.

The values of  $Re_{tr} = 1.95 \times 10^6$  and  $Re_{trt} = 7.8 \times 10^6$  were assumed for the computed values of  $p_b/p_\infty$  shown in Fig. 20 as triangles. The experimental values of  $p_b/p_\infty$  for the



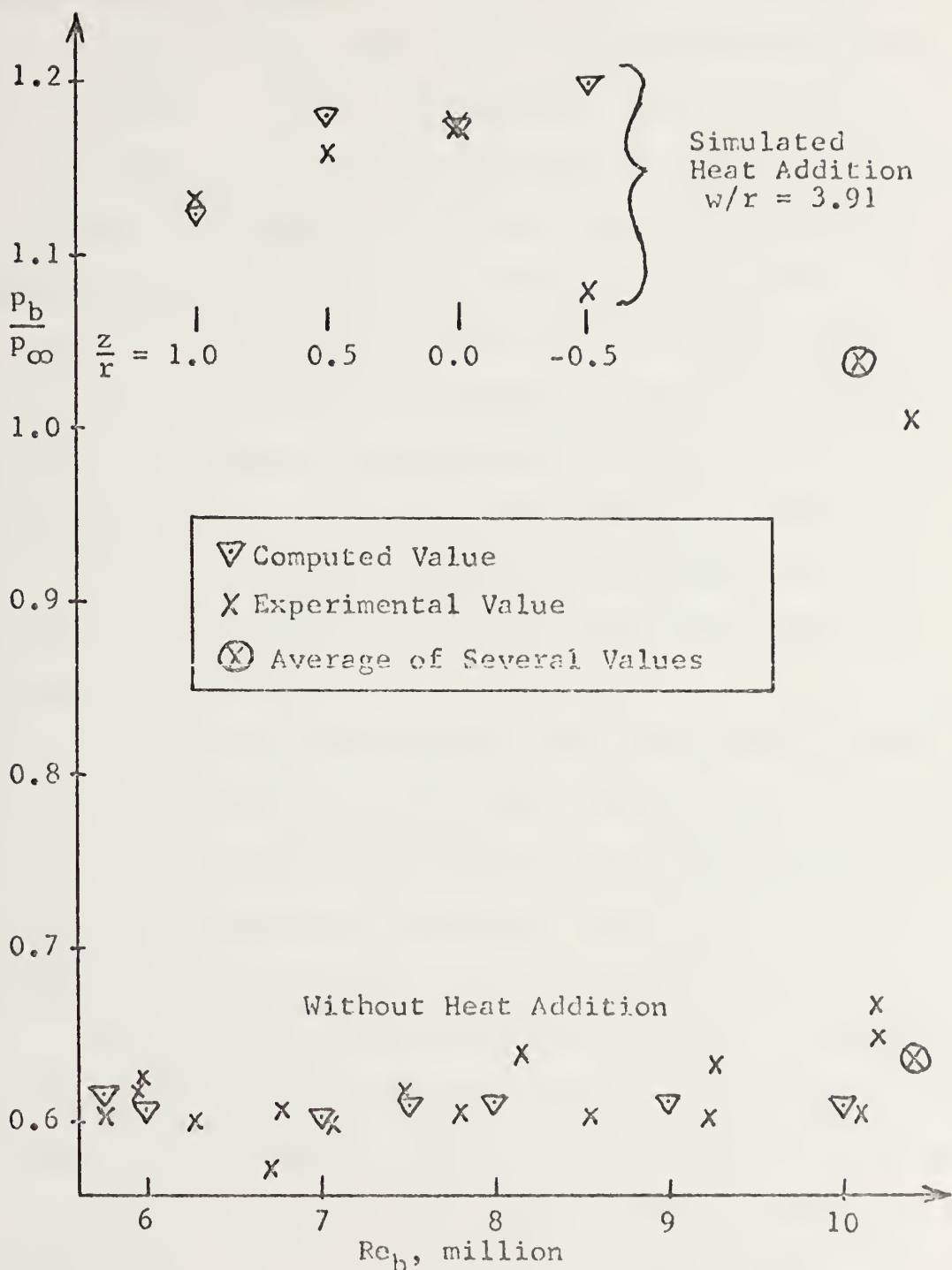


Figure 20. Comparison of Experimental and Computed Values of Base Pressure Ratio vs. Reynolds Number at Mach 2.0 Without and With Simulated Heat Addition





uniform flow nozzle without heat addition showed good agreement with the computed values. Three of the four experimental values of  $p_b/p_\infty$  with  $w/r = 3.91$  compression agreed with the computed values. The observed value of  $p_b/p_\infty$  with  $z/r = -0.5$  was less than the computed value. This difference was attributed to an adverse pressure gradient along the cylinder wall that was not considered in the calculation. In view of this result, base pressure ratios computed by the program given in Appendix J should be considered with caution if the full compression due to external burning impinges ahead of the base on the projectile body.

Figure 21 shows a comparison of experimental [Ref. 26] and computed values of base pressure ratio resulting from spin.

In the Crocco-Lees model there are several input parameters including  $M_\infty$ ,  $k_L$ ,  $k_T$ ,  $Re_{tr}$ ,  $Re_{trt}$  and  $F - \kappa$  relationship. A procedure for predicting the influence of spin on  $p_b/p_\infty$  was discussed previously at the end of Section II. This procedure was used for the computed values in Fig. 21.

Choice of the input parameters remains. Preliminary calculations were conducted with  $M_\infty = 2.86$ ,  $Re_{tr} = 1.95 \times 10^6$  and  $Re_{trt} = 4.6 \times 10^6$ . Values of  $p_b/p_\infty$  had the correct trends relative to experimental values. However, the calculated  $p_b/p_\infty$  for  $Re_b = 2.6 \times 10^6$  and zero spin was about 0.54. To decrease the calculated  $p_b/p_\infty$ , the Mach number was arbitrarily increased to 3.0. For  $Re_b = 2.6 \times 10^6$ , zero spin and  $M_\infty = 3.0$ , the calculated and observed  $p_b/p_\infty$  values agree. In



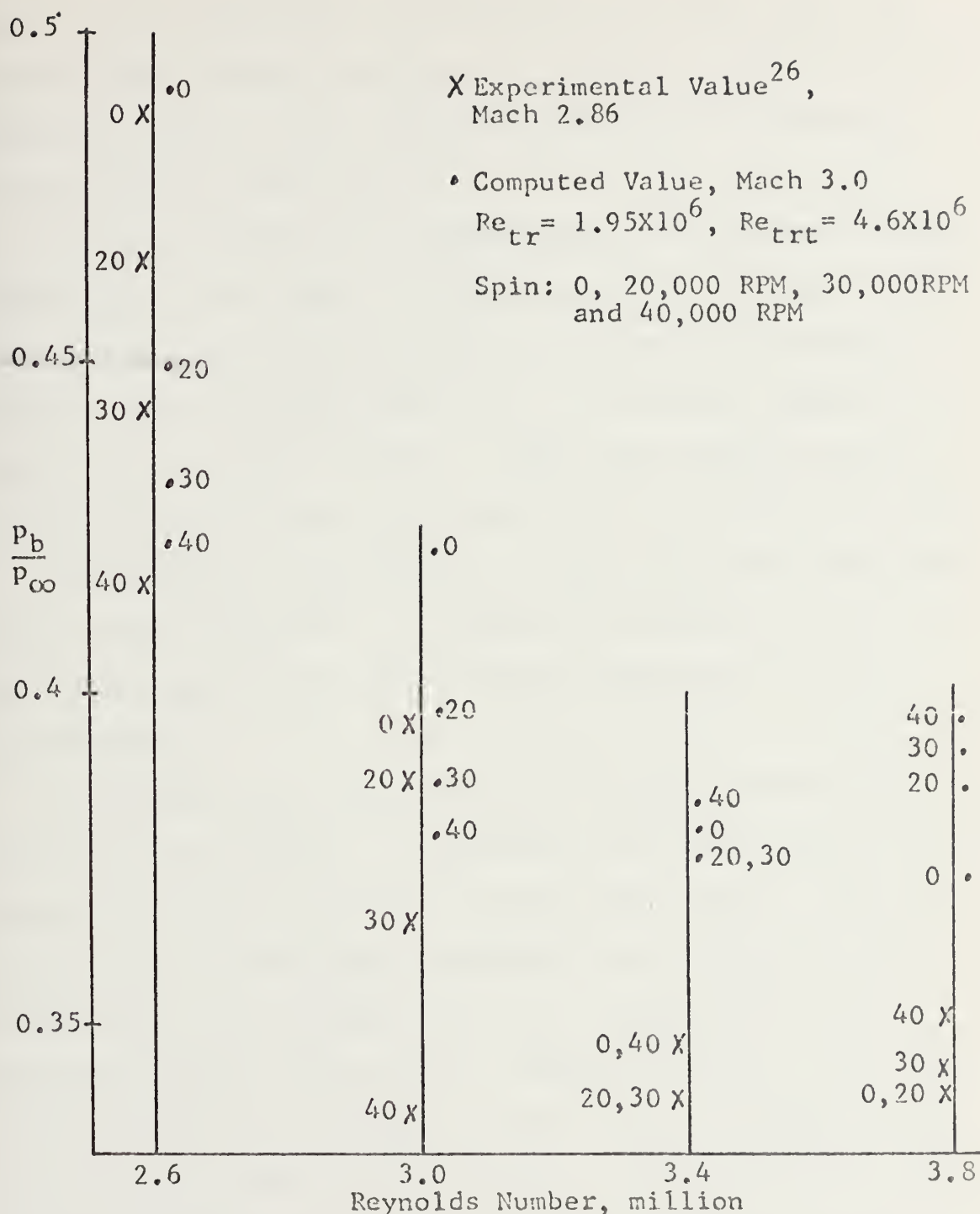


Figure 21. Comparison of Experimental<sup>26</sup> and Computed Values of Base Pressure Ratio vs. Reynolds Number With Spin



retrospect, additional calculations should have been conducted with increased mixing, i.e. larger  $k_T$ , while retaining correct  $M_\infty = 2.86$ . In fact, spin should increase  $k_T$  as discussed in Section II.

A better procedure for calculating the influence of spin might be to use a shift in transition Reynolds number coupled with a  $k_{spin} = k(1+(r\omega/U))$ , as discussed by Smithey, Naber, Caswell and Fuhs [Ref. 15]. The dashed segment of  $p_b/p_\infty$  vs.  $Re_b$  curve in Fig. 17 shows the influence of increased mixing (larger  $k_T$ ) in the vicinity of minimum  $p_b/p_\infty$ .

The computed values shown in Fig. 21 required four hours time on the IBM 360/67. In view of the computing time, the procedure suggested in the preceding paragraph was not accomplished.

To provide some estimate of the optimum location for external heat addition, a fixed fuel flow was assumed to be burned in zones of different length and location. The initial radius of the inner streamline was 2.0 and the outer streamline initial radius was 3.0. The heat zone were assigned integer values from 1 through 6 for  $w/r$ . The zone with  $w/r = 1.0$  was assigned a value of  $Q = r_b q/Uc_p T = 0.2$ . This value was decreased by  $1/(w/r)$  for the other five zones. The heat zones were positioned along the axial axis starting with compression at the base and moving downstream in integer values of radius. The results of two of these computations are shown as the two lower curves in Fig. 22. The



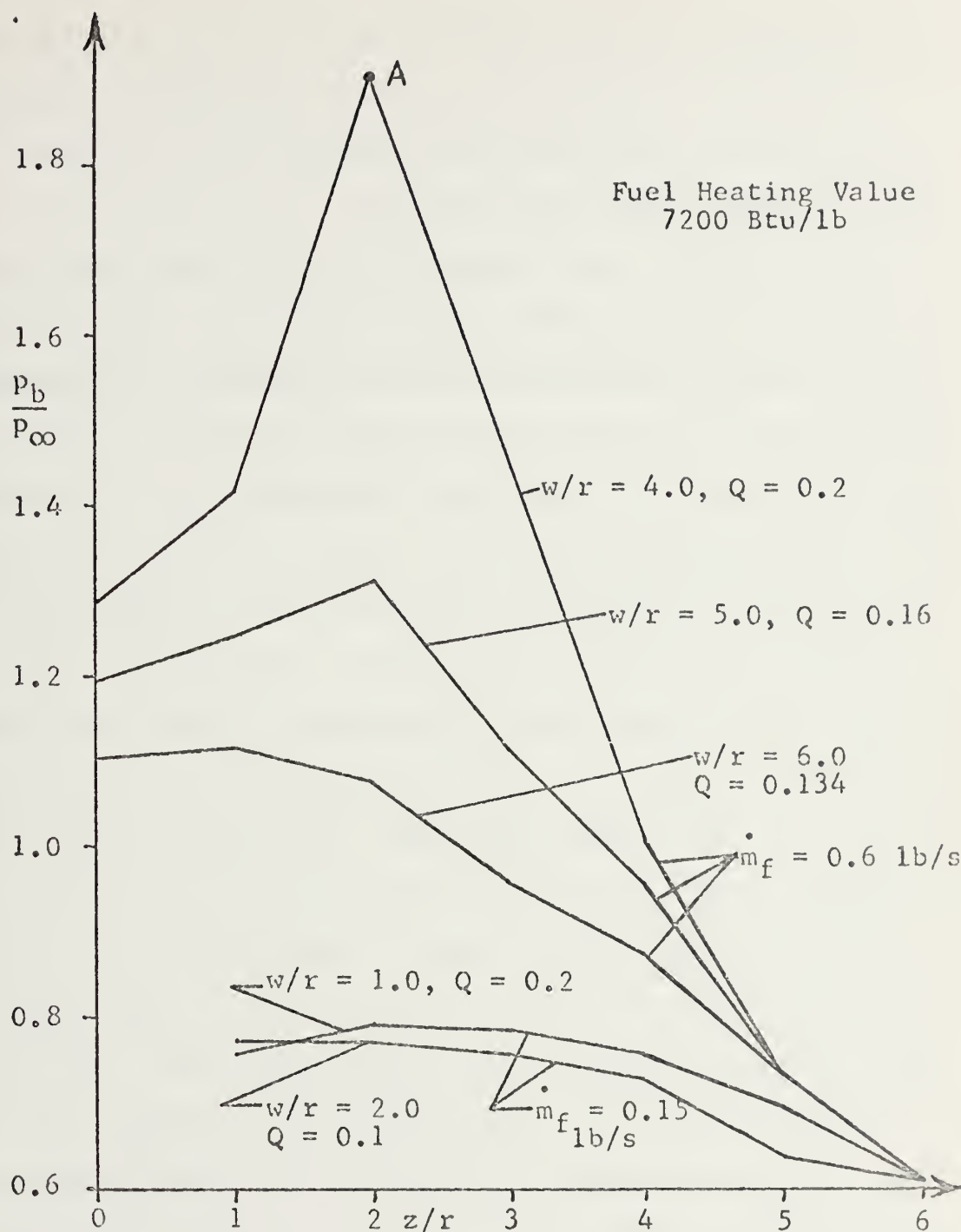


Figure 22. Computed Values of Base Pressure Ratio at a Mach Number of 2.0 With External Burning





gain in  $p_b/p_\infty$  for  $\dot{m} = 0.15$  lb/sec is seen to be fairly insensitive to heat zone size and placement.

Another set of similar calculations were made based on  $Q = 0.8$  at  $w/r = 1.0$ . This value of  $Q$  corresponded to the design fuel flow rate of 0.6 pounds per second at 23,000 feet altitude. The first three values of  $w/r$ , 1.0, 2.0 or 3.0 would not compute because the external flow was driven to a sonic condition by the base pressure rise and the heat addition. This condition is analogous of thermal choking; however, in two dimensional flow both streamtube area change and heat addition drive the flow toward sonic conditions. The last three values of  $w/r = 4.0, 5.0$  and  $6.0$ , did not experience subsonic conditions in the external flow and their values of base pressure ratio are shown as the upper three curves in Fig. 22. The high value of  $p_b/p_\infty = 1.91$  for the  $w/r = 4.0$  curve was not expected. This represents a factor of six increase in base pressure over the two bottom curves in Fig. 22 with a factor of four increase in fuel flow. The combustion for this flight condition, Fig. 23, was assumed to start at  $(z/r) = -1.2$  and the initial compression was on the shear layer, downstream of the base, with full compression at  $z/r = +2.0$ . There is some error in the calculation introduced by neglecting vorticity and by the compression fan at the base, rather than the oblique shock. See Shaprio [Ref. 31] for a discussion of compression fans. Assuming as much as a  $1^\circ$  error in the flow angle, far exceeding the estimate given in Section IV, the value of



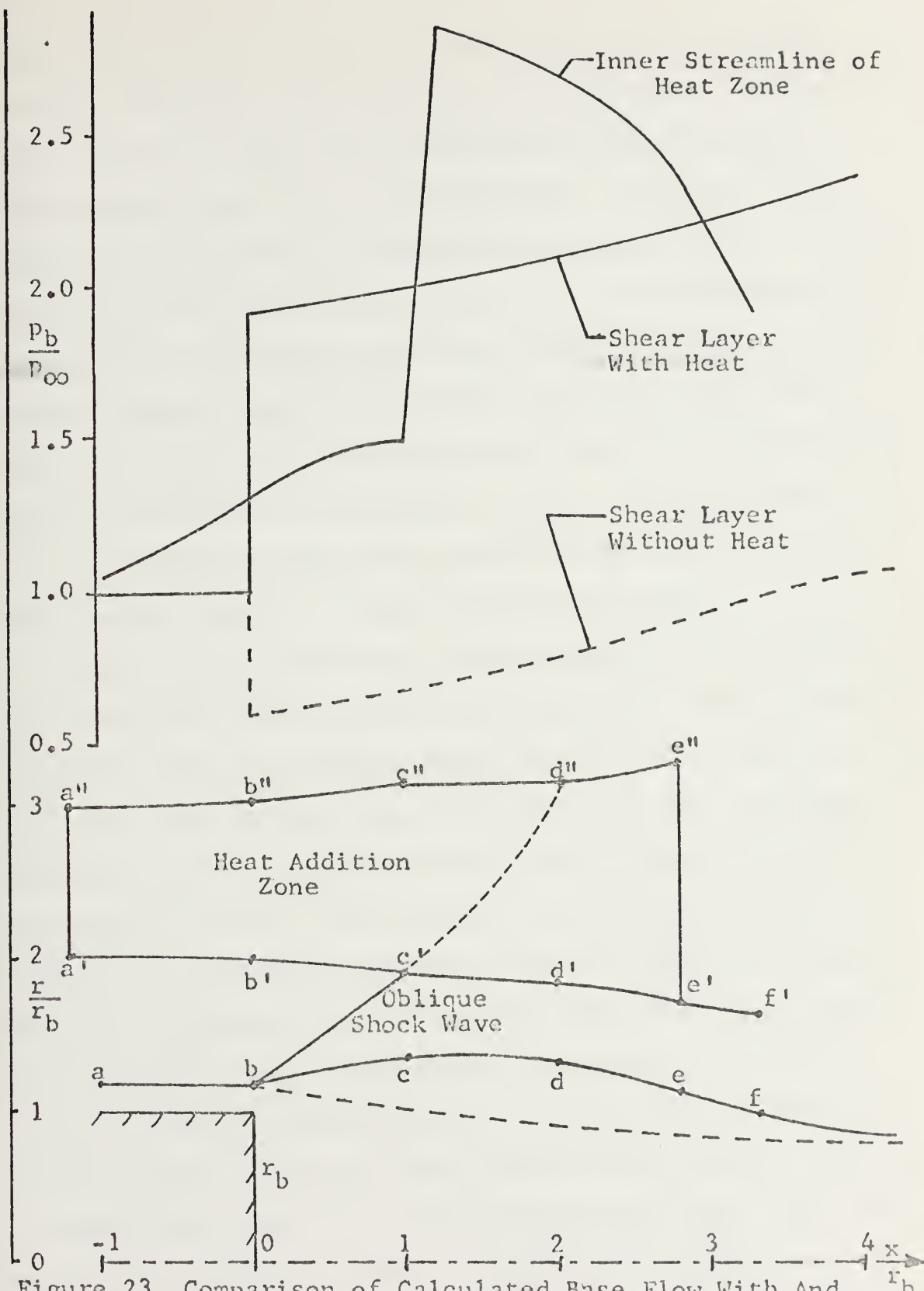


Figure 23. Comparison of Calculated Base Flow With And Without Heat Addition at Mach 2.0



$p_b/p_\infty$  remains at 1.8 and gives specific impulse of 230 seconds. With  $w/r = 4.0$  and  $z/r = 2.0$ , part of the compression due to combustion was applied along the shear layer downstream of the critical point. With  $z/r = 1.0$  more of the compression was applied upstream of the critical point, but the base pressure was less. The variation of  $p_b/p_\infty$  with  $z/r$  indicates that the location of  $dp/ds$  (due to the external compression waves) along the shear layer may be an important consideration in achieving high values of base pressure with external burning. This hypothesis and the condition where the external flow with heat addition becomes subsonic require additional study.

Figure 23 provides some details regarding the optimum flow condition shown in Fig. 22 as point A. The heat zone and shear layer have been plotted in the lower half of Fig. 23. The boundary layer thickness has been included as well as the oblique shock wave which forms when  $p_b/p_\infty$  is greater than one. For comparison, the shear layer without heat addition has been shown as a dashed curve in Fig. 23. Pressure ratios along the shear layer have been plotted in the upper half of Fig. 23; again, the dashed curve is without heat addition. In both cases, with and without heat, the shear layer pressure ratio shows a gradual increase with distance downstream from the base. The pressure ratio along the inner streamline of the heat zone (points a' through e') has also been plotted along with the shear layer pressure ratios (points a through f). This



streamline experiences an abrupt increase in pressure ratio where it intersects the oblique shock wave at  $c'$ ; then, its pressure ratio starts to decrease with a corresponding increase in Mach number, indicating that the flow along the inner streamline accelerates downstream of the oblique shock wave. The calculation along the shear layer was terminated before reaching a maximum pressure ratio due to the saddle point singularity, Fig. 4, since the straddle method employed in the computer program had established the required base pressure ratio within  $\pm \frac{1}{2}\%$ .

Additional calculations with the computer program given in Appendix J would improve the accuracy of  $p_b/p_\infty$  and would take values for the shear layer slightly closer to the critical point, but, since the critical point is a saddle point singularity, would not be expected to calculate through the critical point. Calculation "through" the critical point, using the straddle method, would require changes in the program to restrict the values allowed for  $dF/dw_c$  and force the calculation across the singularity. Additional study is required to include this change and provide the capability of calculating the entire base flow field.

To verify the existence of an oblique shock wave at the base, which was calculated in Fig. 23, one may consider the field of compression waves impinging on the shear layer as being concentrated into a single oblique shock wave impinging on the shear layer. This simplified condition, shown in Fig. 24, has been studied experimentally by Korst





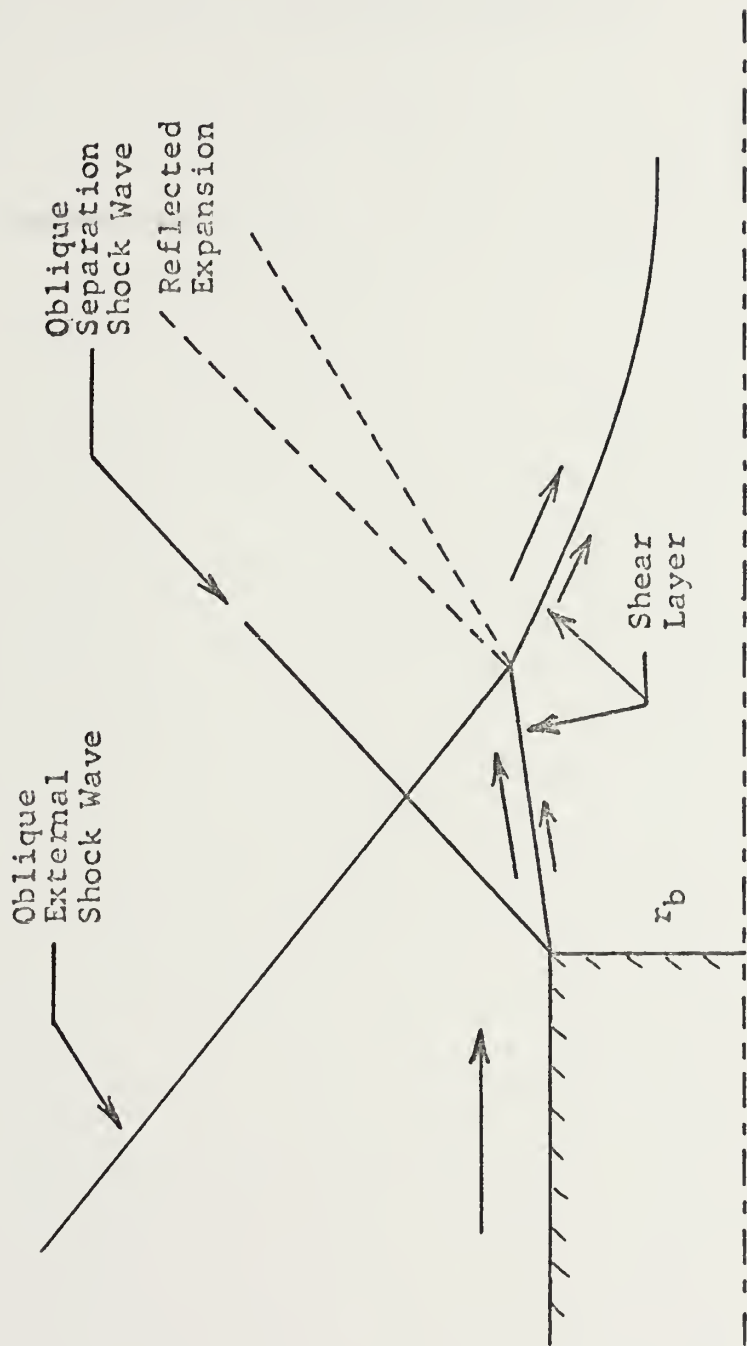


Figure 24. Schematic Diagram of Resulting Base Flow When an External Shock Wave Impinges on the Shear Layer



[Ref.: 36] and was found to create an oblique shock wave at the base. Thus, the calculated shear layer profile and pressure ratios in Fig. 23 are in agreement with experimental results from the simplified condition.



## VI. CONCLUSIONS

With the method of characteristics and the Crocco-Lees base flow model, one can accurately predict the base pressure ratio of a two dimensional or axisymmetric body with moderate external burning for various Mach and Reynolds numbers. The correct values for the two transition Reynolds numbers are essential for accurate base pressure ratio calculation of a particular body and should be obtained from experiment. The effect of projectile spin can be included approximately by dividing the transition Reynolds numbers with one plus the spin number.

Net thrust can be produced by external burning. Placing the combustion zone well forward of the base to give full compression on the body was found by experiment to produce a decrease in thrust. For maximum projectile thrust with supersonic external flow the computed heat zone placement was found to start 1.2 base radii upstream of the base and extend 4.0 base radii downstream. The zone started with an inner and outer streamline of 2.0 and 3.0 base radii respectively and received a fuel flow of 0.6 pounds per second of fuel rich propellant exhaust, ARC-168. It appeared higher values of base pressure would be possible with the same fuel flow rate by decreasing the length of the combustion zone still further. The flow field could not be computed with this heat distribution because of the resulting



subsonic flow and requires additional study to determine any further advantage or limits under these conditions. Experiments with actual combustion should be conducted to determine the feasibility of the desired combustion placement and to measure the resulting base pressure.

The rate of pressure increase along the shear layer due to the heat zone placement appeared to influence the computed value of base pressure ratio. This effect requires additional study to determine its significance in achieving higher values of base pressure ratio with external burning. Experimental studies are needed to determine any variation of the empirical  $F - \kappa$  relation when external pressure waves impinge on the shear layer.





## APPENDIX A: DERIVATION OF THE CHARACTERISTIC EQUATIONS WITH HEAT ADDITION

Equations (1) through (4) govern steady compressible flow with heat addition [Ref. 18]. These equations neglect heat conduction, viscosity and body forces. In natural coordinates, Fig. 1,  $\bar{U} = w\bar{s}$ . The continuity equation, Eqn. (1), may be written

$$(2\pi r)^\alpha \rho w \Delta n = \text{constant} \quad (1A)$$

where  $\alpha = 0$  for two dimensional planar flow and  $\alpha = 1$  for axisymmetric flow. The momentum equation, Eqn. (2), may be written for the two unit vector directions,  $\bar{s}$  and  $\bar{n}$ ,

$$\left( \rho w \frac{\partial w}{\partial s} + \frac{\partial p}{\partial s} \right) \bar{s} = 0 \quad (2A)$$

$$\left( \rho w^2 \frac{\partial \theta}{\partial s} + \frac{\partial p}{\partial n} \right) \bar{n} = 0 \quad (3A)$$

The energy equation, Eqn. (3), becomes

$$w \frac{\partial}{\partial s} \left( h + \frac{1}{2} w^2 \right) = q = w \frac{\partial h_0}{\partial s} \quad (4A)$$

where the total enthalpy,  $h_0 = h + \frac{1}{2}w^2$ , has been used. The thermodynamic relation for entropy,  $S$ , may be written

$$T \nabla S = \nabla h - \frac{1}{\rho} \nabla p \quad (5A)$$

$$T \frac{\partial S}{\partial s} = - \left( w \frac{\partial w}{\partial s} + \frac{1}{\rho} \frac{\partial p}{\partial s} \right) + \frac{\partial h_0}{\partial s} \quad (6A)$$

$$T \frac{\partial S}{\partial n} = - \left( w \frac{\partial w}{\partial n} + \frac{1}{\rho} \frac{\partial p}{\partial n} \right) + \frac{\partial h_0}{\partial n} \quad (7A)$$



Using Eqn. (3A) into (7A)

$$\frac{1}{w} \frac{\partial w}{\partial n} - \frac{\partial \theta}{\partial s} = - \frac{T}{w^2} \frac{\partial S}{\partial n} + \frac{1}{w^2} \frac{\partial h_0}{\partial n} . \quad (8A)$$

Forming the logarithmic derivative of Eqn. (1A) in the s direction

$$\frac{\alpha}{r} \sin \theta + \frac{1}{\rho} \frac{\partial \rho}{\partial s} + \frac{1}{w} \frac{\partial w}{\partial s} + \frac{\partial \theta}{\partial n} = 0 \quad (9A)$$

where the relations  $\partial r / \partial s = \sin \theta$  and  $[1/\Delta n][\partial \Delta n / \partial s] = \partial \theta / \partial n$  have been used. Forming the logarithmic derivative of Eqn. (4) in the s direction

$$\frac{1}{p} \frac{\partial p}{\partial s} = \frac{1}{\rho} \frac{\partial \rho}{\partial s} + \frac{1}{T} \frac{\partial T}{\partial s} . \quad (10A)$$

Substituting Eqns. (2A) and (10A) into (9A)

$$\frac{\alpha}{r} \sin \theta + \left( \frac{1}{w} - \frac{w}{RT} \right) \frac{\partial w}{\partial s} - \frac{1}{T} \frac{\partial T}{\partial s} + \frac{\partial \theta}{\partial n} = 0 . \quad (11A)$$

From Eqn. (4A)

$$\frac{q}{w} = c_p \frac{\partial T}{\partial s} + w \frac{\partial w}{\partial s} \quad (12A)$$

where the enthalpy has been written in terms of a constant  $c_p$ ,  $h = c_p T$ . Substituting Eqn. (12A) into (11A)

$$\left( \frac{1}{w} - \frac{w}{RT} + \frac{w}{c_p T} \right) \frac{\partial w}{\partial s} + \frac{\partial \theta}{\partial n} - \frac{q}{wc_p T} + \frac{\alpha \sin \theta}{r} = 0 . \quad (13A)$$

Combining terms, and using the Mach angle relation  $\cot^2 \mu = M^2 - 1$ , Eqn. (13A) becomes

$$\frac{\cot^2 \mu}{w} \frac{\partial w}{\partial s} - \frac{\partial \theta}{\partial n} = \frac{\alpha \sin \theta}{r} - \frac{q}{wc_p T} . \quad (14A)$$



The Prandtl-Meyer Angle,  $\nu$ , is defined by the relation

$$d\nu = \frac{\cot \mu}{w} dw . \quad (15A)$$

Using Eqn. (15A) into (14A) and multiplying by  $\tan \mu$

$$\frac{\partial \nu}{\partial s} - \tan \mu \frac{\partial \theta}{\partial n} = \tan \mu \left\{ \frac{\alpha \sin \theta}{r} - \frac{q}{w c_p T} \right\} . \quad (16A)$$

Similarly, Eqn. (15A) into (8A) becomes

$$\tan \mu \frac{\partial \nu}{\partial n} - \frac{\partial \theta}{\partial s} = - \frac{T}{w^2} \frac{\partial S}{\partial n} + \frac{1}{w^2} \frac{\partial h_0}{\partial n} . \quad (17A)$$

Adding Eqns. (16A) and (17A)

$$\begin{aligned} \left( \frac{\partial}{\partial s} + \tan \mu \frac{\partial}{\partial n} \right) (\nu - \theta) &= \tan \mu \left\{ \frac{\alpha \sin \theta}{r} - \frac{q}{w c_p T} \right\} \\ &- \frac{1}{w^2} \left\{ T \frac{\partial S}{\partial n} - \frac{\partial h_0}{\partial n} \right\} . \end{aligned} \quad (18A)$$

Subtracting Eqn. (17A) from (16A)

$$\begin{aligned} \left( \frac{\partial}{\partial s} - \tan \mu \frac{\partial}{\partial n} \right) (\nu + \theta) &= \tan \mu \left\{ \frac{\alpha \sin \theta}{r} - \frac{q}{w c_p T} \right\} \\ &+ \frac{1}{w^2} \left\{ T \frac{\partial S}{\partial n} - \frac{\partial h_0}{\partial n} \right\} . \end{aligned} \quad (19A)$$

Now, in the characteristic coordinate system

$$\sec \mu \frac{\partial ( \quad )}{\partial \eta} = \left( \frac{\partial}{\partial s} + \tan \mu \frac{\partial}{\partial n} \right) ( \quad ) \quad (20A)$$

and

$$\sec \mu \frac{\partial ( \quad )}{\partial \xi} = \left( \frac{\partial}{\partial s} - \tan \mu \frac{\partial}{\partial n} \right) ( \quad ) . \quad (21A)$$



With this, Eqns. (18A) and (19A) become

$$\frac{\partial(v - \theta)}{\partial\eta} = \sin\mu \left\{ \frac{\alpha \sin\theta}{r} - \frac{q}{wc_p T} \right\} - \frac{\cos\mu}{w^2} \left\{ T \frac{\partial S}{\partial n} - \frac{\partial h_0}{\partial n} \right\} \quad (22A)$$

and

$$\frac{\partial(v + \theta)}{\partial\xi} = \sin\mu \left\{ \frac{\alpha \sin\theta}{r} - \frac{q}{wc_p T} \right\} + \frac{\cos\mu}{w^2} \left\{ T \frac{\partial S}{\partial n} - \frac{\partial h_0}{\partial n} \right\}. \quad (23A)$$

Eqns. (22A) and (23A) are the characteristic equations, with heat addition, governing the two dimensional planar,  $\alpha = 0$ , or axisymmetric,  $\alpha = 1$ , flow. These equations are dimensional, having the dimension of reciprocal length.





## APPENDIX B: DERIVATION OF CONDITION FOR IRROTATIONALITY WITH HEAT ADDITION

The equations required for this derivation are momentum with no viscosity or body force,

$$\frac{D\bar{U}}{Dt} = - \frac{1}{\rho} \nabla p \quad (1B)$$

where  $\bar{U}$  is velocity,  $\rho$  is density, and  $p$  is static pressure; energy with heat addition, but without viscosity, body force, or conduction,

$$\frac{D(h + \frac{1}{2}\bar{U} \cdot \bar{U})}{Dt} = q + \frac{1}{\rho} \frac{\partial p}{\partial t} \quad (2B)$$

where  $h$  is enthalpy, and  $q$  is time rate of heat addition per unit mass; the second law of thermodynamics

$$T \nabla S = \nabla h - \frac{1}{\rho} \nabla p \quad (3B)$$

where  $S$  is specific entropy; and the vector identity

$$\bar{U} \cdot \nabla \bar{U} = \nabla(\frac{1}{2}\bar{U} \cdot \bar{U}) - \bar{U} \times (\nabla \times \bar{U}). \quad (4B)$$

Combining Eqns. (1B), (3B) and (4B)

$$\frac{\partial \bar{U}}{\partial t} + \nabla(\frac{1}{2} \bar{U} \cdot \bar{U}) - \bar{U} \times (\nabla \times \bar{U}) = T \nabla S - \nabla h. \quad (5B)$$

Introducing the definition for total enthalpy,  $h_0 = h + \frac{1}{2}\bar{U} \cdot \bar{U}$ , into Eqn. (5B), one obtains Crocco's Theorem

$$T \nabla S + \bar{U} \times (\nabla \times \bar{U}) = \nabla h_0 + \frac{\partial \bar{U}}{\partial t}. \quad (6B)$$

Let  $\nabla \times \bar{U} = \bar{\Omega}$  and take the curl of Eqn. (6B),

$$\frac{D\bar{\Omega}}{Dt} = \nabla T \times \nabla S + \bar{\Omega} \cdot \nabla \bar{U} - \bar{\Omega} \nabla \cdot \bar{U} \quad (7B)$$



since  $\nabla \cdot \bar{\Omega} = \nabla \cdot (\nabla X \bar{U}) = 0$  and the curl of a gradient is zero. Eqn. (7B) describes the total rate of change of vorticity,  $\bar{\Omega}$ .

Now assume that  $\bar{\Omega} = 0$  prior to and during heat addition. Eqn. (7B) becomes

$$\frac{D\bar{\Omega}}{Dt} = \nabla T \times \nabla S = 0. \quad (8B)$$

Then, Eqn. (8B) is the condition which must be satisfied during heat addition if the flow is to remain irrotational; that is, the temperature gradient must be parallel to the entropy gradient. Referring to Eqn. (3B) and assuming  $h = c_p T$ , where  $c_p$  is constant, the condition for irrotationality may be stated in terms of pressure; that is, the temperature gradient must be parallel to the pressure gradient.

In the case of steady flow, the irrotationality condition may be given in terms of heat per unit mass which has been added,  $Q$ . In Eqn. (2B) let  $q = \bar{U} \cdot \nabla Q$ , and, using the total enthalpy  $h_0 = h + \frac{1}{2} \bar{U} \cdot \bar{U}$ ,

$$\bar{U} \cdot \nabla (h_0 - Q) = 0. \quad (9B)$$

Then along any streamline

$$h_0 - Q = h_{0\infty} \quad (10B)$$

where it is assumed that the upstream conditions, before heat is added, i.e.  $Q = 0$ , are uniform [Ref. 19]. With these assumptions one may take the gradient of Eqn. (10B)

$$\nabla (h_0 - Q) = 0 \quad (11B)$$



since  $h_{0\infty}$  is constant. Using the steady form of Eqn. (6B), with  $\bar{\Omega} = 0$ , and Eqn. (11B)

$$\nabla S = \frac{1}{T} \nabla h_0 = \frac{1}{T} \nabla Q. \quad (12B)$$

Also, from Eqn. (11B), one may write

$$\nabla Q = \nabla(h + \frac{1}{2}\bar{U} \cdot \bar{U}) = c_p \nabla T + \nabla(\frac{1}{2}\bar{U} \cdot \bar{U}). \quad (13B)$$

Combining Eqns. (12B) and (13B) in (8B)

$$\frac{1}{c_p} \left\{ \nabla Q - \nabla(\frac{1}{2}\bar{U} \cdot \bar{U}) \right\} \times \frac{1}{T} \nabla Q = 0. \quad (14B)$$

Since  $(\nabla Q) \times (\nabla Q) = 0$ , Eqn. (14B) reduces to

$$(\nabla Q) \times \nabla(\frac{1}{2}\bar{U} \cdot \bar{U}) = 0. \quad (15B)$$

Eqn. (15B) is the condition which must be satisfied to preserve irrotationality in steady flow with heat addition; that is, the gradient of heat added must be parallel to the gradient of kinetic energy.

If the gradient of heat added is a small perturbation, as is the case of linearized flow, then the irrotationality condition in Eqn. (15B) is automatically satisfied. To show this let  $Q = h_{\infty} Q'$ , where  $|Q'| \ll 1$ , and  $\bar{U} = U_{\infty}(\bar{i} + \frac{\bar{U}'}{U_{\infty}})$ , where  $\bar{U}' \cdot \bar{U}' \ll 1$ , then, substituting in Eqn. (15B),

$$\nabla Q \times \nabla(\frac{1}{2}\bar{U} \cdot \bar{U}) = h_{\infty} \nabla Q' \times \nabla(U_{\infty} \bar{i} \cdot \bar{U}' + \frac{1}{2}\bar{U} \cdot \bar{U}') \quad (16B)$$

is of second and third order perturbation.

This condition may be applied to Eqns. (24A) and (25A), Appendix A, and neglect the vorticity term

$$\frac{1}{w} \left\{ T \frac{\partial S}{\partial n} - \frac{\partial h_0}{\partial n} \right\},$$



thus simplifying the method of characteristics calculation. First of all, if the heat zone is started in a region of uniform flow along a line normal to the streamlines, and if the heat is added uniformly in a zone bounded by two streamlines, then the condition of Eqn. (15B) will be approximately satisfied within the zone since the gradient of heat added will be approximately parallel to the gradient of kinetic energy. Second, if the first condition is not satisfied (i.e., along the streamline boundaries of the heat zone where there is a jump in  $Q$  normal to the streamline), the vorticity may still be neglected if the heat added is a small perturbation, that is

$$q = \bar{U} \cdot \nabla Q = h_{\infty} \bar{U} \cdot \nabla Q'. \quad (17B)$$

Then the heat term used in Eqns. (24A) and (25A) must be

$$\frac{q}{w c_p T} = \frac{h_{\infty} w (\partial Q' / \partial s)}{w c_p T} \doteq \frac{\partial Q'}{\partial s} \ll 1/r_b. \quad (18B)$$

This condition is satisfied for the heat zone boundary, where  $r_b q / w c_p T$  is taken as 0.171 to get  $-4\frac{1}{2}^\circ$  deflection of the inner heat zone streamline.





# APPENDIX C: BRIEF DEVELOPMENT OF CROCCO-LEES BASE FLOW FORMULATION [Refs. 1,8,13]

The mass flux,  $\bar{m}$ , in the base flow is given by the integral

$$\bar{m} = \int_0^{\delta} (2\pi r)^{\alpha} \rho u dr \quad (1C)$$

where  $\delta$  is the viscous flow thickness,  $r$  is radius,  $\rho$  is density,  $u$  is axial component of velocity,  $\alpha$  equals zero for two dimensional planar flow and  $\alpha$  equals one for axisymmetric flow. The momentum flux is

$$I = \int_0^{\delta} (2\pi r)^{\alpha} \rho u^2 dr . \quad (2C)$$

For the base flow, where there is no wall drag, the momentum equation becomes

$$\frac{dI}{dx} = u_e \frac{d\bar{m}}{dx} - (\pi\delta)^{\alpha} \delta \frac{dp}{dx} \quad (3C)$$

where  $u_e$  is the external axial component of velocity,  $dp/dx$  is the static pressure gradient and, assuming small angles,

$$\frac{d\bar{m}}{dx} = (2\pi\delta)^{\alpha} \rho_e u_e \left( \frac{d\delta}{dx} - \theta_e \right). \quad (4C)$$

A major point of the Crocco-Lees theory is that

$$\frac{d\delta}{dx} - \theta_e = k \quad (5C)$$

where  $k$  is a non dimensional mixing coefficient which must be specified. The value for  $k$  is approximately 0.0033 for laminar mixing and 0.03 for turbulent mixing.



A mean velocity is defined by

$$u_1 = I/\bar{m} \quad (6C)$$

and a velocity ratio by

$$\kappa = u_1/u_e. \quad (7C)$$

The mean density,  $\rho_1$ , is defined by the equation

$$\bar{m} = (\pi\delta)^\alpha \delta \rho_1 u_1. \quad (8C)$$

It is assumed that the stagnation temperature is constant throughout the flow and that the lateral pressure gradient,  $dp/dr$ , is zero. Knowing the pressure,  $p = p_e$ , and  $\rho_1$ , a mean temperature,  $T_1$ , can be defined

$$T_1 = p_e/\rho_1 R. \quad (9C)$$

Introducing the displacement thickness,  $\delta^*$ , and momentum thickness,  $\delta^{**}$ , of ordinary boundary layer theory

$$\delta^{*(1+\alpha)} = \int_0^\delta (2r)^\alpha \left(1 - \frac{\rho u}{\rho_e u_e}\right) dr = \delta^{(1+\alpha)} - \frac{\bar{m}}{\rho_e u_e \pi^\alpha} \quad (10C)$$

and

$$\begin{aligned} \delta^{**(1+\alpha)} &= \int_0^\delta (2r)^\alpha \frac{\rho u}{\rho_e u_e} \left(1 - \frac{u}{u_e}\right) dr \\ &= \delta^{(1+\alpha)} - \delta^{*(1+\alpha)} - \frac{I}{\rho_e u_e^2 \pi^\alpha}. \end{aligned} \quad (11C)$$

Noting that  $\kappa = I/\bar{m}u_e$  and using Eqns. (10C) and (11C), one has



$$\kappa = \frac{\delta^{(1+\alpha)} - \delta^*{}^{(1+\alpha)} - \delta^{**}{}^{(1+\alpha)}}{\delta^{(1+\alpha)} - \delta^*{}^{(1+\alpha)}} . \quad (12C)$$

On application of the Stewartson transformation [Refs. 8,13] one finds  $\delta$ ,  $\delta^*$ , and  $\delta^{**}$  in Eqn. (12C) are replaced by the incompressible quantities  $\delta_i$ ,  $\delta_i^*$  and  $\delta_i^{**}$ . Thus, within the restrictions of the Stewartson transformation, any compressible laminar base flow can be related to a corresponding incompressible laminar flow. It is assumed this also applies in the turbulent case. The ratio of mean temperature,  $T_1$ , to stagnation temperature,  $T_s$ , may be written

$$\frac{T_1}{T_s} = f - \frac{\gamma-1}{2} w_1^2 \quad (13C)$$

where

$$f = \frac{\kappa \delta_i^{(1+\alpha)}}{\delta_i^{(1+\alpha)} - \delta_i^*{}^{(1+\alpha)}} \quad (14C)$$

$w_1 = u_1/a_s$ , and  $a_s$  is the stagnation speed of sound. It has been found more convenient to work with the quantity  $F \geq 0$ ,

$$F + 1 = f/\kappa^2. \quad (15C)$$

Experimental data [Ref. 8] has shown a relationship between  $F$  and  $\kappa$  which can be expressed by the polynomial

$$\kappa = 1.0 - 0.4F + 0.16F^2 - 0.01185F^3. \quad (16C)$$

For  $F \geq 1.5$ ,  $\kappa = 0.72$  and  $d\kappa/dF = 0.0$ .



From Eqn. (8C) one may write an expression for mass flux

$$m = \bar{m}_s = \frac{\gamma(\pi\delta)^\alpha \delta p_e w_e}{\kappa[F + 1 - \frac{\gamma-1}{2} w_e^2]} \quad (17C)$$

Using this and Eqns. (3C), (4C) and (5C) one may form a single ordinary differential equation

$$\frac{dF}{dw_e} = \left( \frac{\gamma+1}{2} w_e^2 - 1 \right) \left( 1 - \frac{\gamma-1}{2} w_e^2 \right) + \frac{F \left[ \gamma w_e^2 - \frac{\kappa F}{1 - \kappa} + \frac{1 - \frac{\gamma-1}{2} w_e^2}{1 - \kappa} \frac{\theta_e}{k} \right]}{w_e \left( 1 - \frac{\gamma-1}{2} w_e^2 \right) \left\{ \left[ \frac{1 - \frac{\gamma-1}{2} w_e^2}{\kappa (1 - \kappa)} \frac{\theta_e}{k} - \kappa \frac{F}{(1 - \kappa)} \right] (d\kappa/dF) - 1 \right\}} \quad (18C)$$

Eqn. (18C) has a saddle point singularity, [Refs. 1,8], also called the critical point, which, in integrated form, determines the one unique solution describing the given base flow condition. In two dimensional planar flow without external heat addition, where  $\theta_e$  is known from  $w_e$  by the Prandtl-Meyer relation, one may start at the critical point, where both the numerator and denominator of Eqn. (18C) are zero, and integrated toward the base [Ref. 8]. In flow with external heat addition, and in axisymmetric flow,  $\theta_e$  is not known as a function of  $w_e$ ; thus, in these cases, one must start integration of Eqn. (18C) at the base and concurrently solve the external flow field, by the method of characteristics or linearized theory, for the values of  $\theta_e$  along the shear layer. This process is one of trial and error described in section IV as the straddle method.





# APPENDIX D: CALCULATION OF BOUNDARY LAYER MASS FLUX AT THE BASE

The boundary layer is assumed to be adiabatic, have constant pressure across its thickness,  $\delta$ , and have a velocity profile  $(u/u_e) = (y/\delta)^{1/n}$ , where  $u_e$  is the external flow velocity and  $n$  is an integer [Ref. 24];  $1 \leq n \leq 7$ , for laminar to turbulent flow. The boundary layer mass flux at the base is given by the integral

$$\bar{m}_b = \int_{r_b}^{r_b + \delta} (2\pi r)^\alpha \rho u dr \quad (1D)$$

where  $\alpha$  is zero for two dimensional planar flow, or one for axisymmetric flow,  $\rho$  is density and  $r_b$  is the base radius or half-height. Using the equation of state,  $p = \rho RT$ , and the above assumptions, Eqn. (1D) becomes

$$\bar{m}_b = \frac{p_e}{R} \int_{r_b}^{r_b + \delta} \frac{(2\pi r)^\alpha u_e \left(\frac{r-r_b}{\delta}\right)^{1/n} dr}{T_T - \frac{u_e^2}{2c_p} \left(\frac{r-r_b}{\delta}\right)^{2/n}} \quad (2D)$$

where  $p_e$  is the external pressure. Defining  $w_e$  as  $u_e/a_s$ , where  $a_s$  is the stagnation speed of sound, Eqn. (2D) becomes

$$m_b = \bar{m}_b a_s = \gamma \delta p_e w_e (2\pi \delta)^\alpha \int_{r_b}^{r_b + \delta} \frac{\left(\frac{r-r_b}{\delta}\right)^{1/n} \left(\frac{r}{\delta}\right)^\alpha \left(\frac{dr}{\delta}\right)}{1 - \frac{\gamma-1}{2} w_e^2 \left(\frac{r-r_b}{\delta}\right)^{2/n}} \quad (3D)$$



Then

$$M_b = \frac{m_b}{\gamma \delta p_e w_e (2\pi \delta)^\alpha} = \int_0^1 \frac{X^{1/n} (X + \frac{r_b}{\delta})^\alpha dx}{1 - B^2 X^{2/n}} \quad (4D)$$

where  $x = (r - r_b)/\delta$  and  $B^2 = \frac{\gamma-1}{2} w_e^2$ .

If  $\alpha = 0$  and  $x = z^n$ , Eqn. (4D) becomes

$$I_{2D} = n \int_0^1 \frac{z^n dz}{1 - B^2 z^2} \quad (5D)$$

This may be integrated. For  $n$  odd, Eqn. (5D) gives

$$I_{2D_{ODD}} = n \left\{ \frac{1}{2B^{n+1}} \ln\left(\frac{1}{1-B^2}\right) - \sum_{j=1}^{(n-1)/2} \frac{1}{[n+1-2j] B^{2j}} \right\}$$

where the summation is omitted if  $n = 1$ . For  $n$  even, Eqn. (5D) gives

$$I_{2D_{EVN}} = n \left\{ \frac{1}{2B^{n+1}} \ln\left(\frac{1+B}{1-B}\right) - \sum_{j=1}^{n/2} \frac{1}{[n+1-2j] B^{2j}} \right\} \quad (7D)$$

If  $\alpha = 1$  and  $x = z^n$ , Eqn. (4D) becomes

$$I_{AXI} = n \int_0^1 \frac{z^{2n} dz}{1-B^2 z^2} + \frac{r_b}{\delta} n \int_0^1 \frac{z^n dz}{1-B^2 z^2} \quad (8D)$$

The second integral in Eqn. (8D) is the same as Eqn. (5D), which is evaluated in Eqns. (6D) and (7D). Integrating the first integral, Eqn. (8D) becomes



$$I_{AXI} = n \left\{ \frac{1}{2B^{2n+1}} \ln \left( \frac{1+B}{1-B} \right) - \sum_{j=1}^n \frac{1}{[2(n-j)+1]B^{2j}} \right\} + \frac{r_b}{\delta} I_{2D}. \quad (9D)$$

The results of Eqns. (6D), (7D) and (9D) are used with Eqn. (4D) to evaluate  $m_{b_{2D}}$  or  $m_{b_{AXI}}$ . This boundary layer mass flux at the base, before the corner expansion,  $m_b$ , is set equal to the mass flux after the corner expansion,  $m'_b$ , expressed in terms of the Crocco-Lees formulation, Appendix C.

$$m_{b_{2D}} = \gamma \delta p_e w_e I_{2D} = m'_{b_{2D}} = \frac{\gamma \delta' p_e' w_e'}{\kappa' [F' + 1 - \frac{\gamma - 1}{2} w_e'^2]} \quad (10D)$$

Taking  $\kappa' = 0.72$  and the value of  $w_e'$  assumed from the straddle method, one solves Eqn. (10D) for the value of  $F'$  which starts the integration along the shear layer. Similarly, in the axisymmetric case,

$$m_{b_{AXI}} = 2\pi \gamma \delta^2 p_e w_e I_{AXI} = m'_{b_{AXI}} = \frac{\pi \gamma \delta'^2 p_e' w_e'}{\kappa' [F' + 1 - \frac{\gamma - 1}{2} w_e'^2]} \quad (11D)$$



## APPENDIX E: MASS FLUX CALCULATION ALONG THE SHEAR LAYER

From Appendix C, Eqn. (17C), the mass flux,  $m$ , may be written

$$m = \frac{\gamma(\pi\delta)^\alpha \delta \rho_e w_e}{\kappa [F+1 - \frac{\gamma-1}{2} w_e^2]} \quad (1E)$$

where  $\alpha = 0$  for the two dimensional planar flow and  $\alpha = 1$  for axisymmetric flow. One may evaluate Eqn. (1E) at two adjacent points along the shear layer,  $m_i$  and  $m_{i+1}$ , and solve for the distance between these two points,  $dx$ , by using the additional relations [Ref. 1,8].

$$\frac{d\delta}{dx} = \theta + k \quad (2E)$$

and

$$\frac{dm}{dx} = (2\pi\delta)^\alpha \rho_e w_e a_s^2 \left( \frac{d\delta}{dx} - \theta \right). \quad (3E)$$

Assuming small angles, Eqn. (2E) states that the rate of change of the shear layer height or radius,  $d\delta/dx$ , is equal to the flow angle  $\theta$  plus some constant,  $k$ . Then the rate of change of mass flux,  $dm/dx$ , given by Eqn. (3E), is the mass entrained by the shear layer from the external flow.

To compute  $m_{i+1}$ , one increments  $F_i$  with  $\Delta F_i$ , say  $\Delta F_i = 0.1F_i$  with the condition  $\Delta F \geq 0.08$ ,

$$F_{i+1} = F_i + \Delta F_i. \quad (4E)$$

Then

$$w_{e,i+1} = w_{e,i} + \Delta F_i / (dF/dw_e) \quad (5E)$$





where  $dF/dw_e$  is computed from Eqn. (18C). The value for  $\kappa_{i+1}$  is computed from an empirical relation using  $F_{i+1}$ , given by Eqn. (16C), with  $\kappa_{i+1} = 0.72$  if  $F_{i+1} \geq 1.5$ . The isentropic relation between static and total pressure, in terms of  $\gamma$  and  $w_e$ , is used to evaluate  $p_e$  at  $i$  and  $i+1$ . Average values between  $i$  and  $i+1$  are used to evaluate  $d\delta/dx$  and  $dm/dx$ , where the isentropic relation between static and total density must be used with the latter. Since

$$m_{i+1} = m_i + (dm/dx)dx \quad (4E)$$

and

$$\delta_{i+1} = \delta_i + (d\delta/dx)dx \quad (5E)$$

One may solve directly for the value of  $dx$ , in the two dimensional planar case, which corresponds to the increment  $\Delta F_i$

$$dx_{i_{2D}} = \delta_i \left( \frac{m_i}{\delta_i} - \frac{m_{i+1}}{\delta_{i+1}} \right) / \left( \frac{d\delta}{dx} - \frac{dm}{dx} \right). \quad (6E)$$

For the axisymmetric case

$$dx_{i_{AXI}} = \frac{1}{2} \left( dx_{i_{2D}} - \frac{1}{\delta_i} \frac{d\delta}{dx} dx_{i_{AXI}}^2 \right). \quad (7E)$$

Eqn. (7E) may be iterated several times, as long as  $dx_{i_{AXI}} \leq 1$ , to determine the correct value of  $dx_{i_{AXI}}$ .



## APPENDIX F: CALCULATION OF BOUNDARY LAYER THICKNESS AND MIXING COEFFICIENT

The laminar boundary layer thickness,  $\delta_L$ , was computed at point  $x$  from the compressible Blasius solution [Ref. 8]

$$\delta_L = (5.0 + 1.2(\gamma-1)M^2)x/(Re_x)^{1/2} \quad (1F)$$

where  $x$  is the distance along the surface from the leading edge and  $Re_x$  is the Reynolds number based on this distance. If the base Reynolds number,  $Re_b$ , is less than the transition Reynolds number,  $Re_{tr}$ , then the boundary layer at the base is completely laminar and its thickness was computed from Eqn. (1F), with  $x$  taken as the body length.

If the base Reynolds number,  $Re_b$ , is greater than the transition Reynolds number,  $Re_{tr}$ , the boundary layer will be partly or completely turbulent. The turbulent thickness,  $\delta_T$ , was computed from [Ref. 8]

$$\delta_T = \frac{0.037x}{(Re_x)^{1/5}}(C_{fM}/C_{fi})(\delta/\delta^{**}) \quad (2F)$$

$C_{fi}$  is von Karman's incompressible turbulent skin friction coefficient given by [Ref. 24]

$$(0.242)/(C_{fi})^{1/2} = \log_{10}(Re_x C_{fi}) \quad (3F)$$

and  $C_{fM}$  is van Driest's compressible turbulent skin friction coefficient given by [Ref. 24]

$$\frac{0.242(1-B^2)^{1/2}}{(B^2 C_{fM})^{1/2}} \sin^{-1} B = \log_{10}(Re_x C_{fM}) + 1.26 \log_{10}(1-B^2) \quad (4F)$$



where  $B^2$  is  $(\gamma-1)w_e^2/2$ . Equations (3F) and (4F) must be solved by iteration. The quantity  $\delta/\delta^{**}$  (Appendix C) may be evaluated for the two dimensional 1/7th profile using the same assumptions employed in Appendix D. Briefly

$$\delta^{**} = \int_{r_b}^{r_b+\delta} \frac{(\rho u)}{(\rho_e u_e)} \left( 1 - \frac{u}{u_e} \right) dr \quad (5F)$$

$$\frac{\delta^{**}}{\delta} = \left( 1 - \frac{1}{2} w_e^2 \right) \int_{r_b}^{r_b+\delta} \frac{\left( \frac{r-r_b}{\delta} \right)^{1/7} - \left( \frac{r-r_b}{\delta} \right)^{2/7}}{\left( 1 - \frac{\gamma-1}{2} w_e^2 \left( \frac{r-r_b}{\delta} \right)^{2/7} \right)} (dr/\delta) \quad (6F)$$

$$\begin{aligned} \frac{\delta^{**}}{\delta} = & 7(1-B^2) \left( \frac{1}{2B^8} \ln \left( \frac{1}{1-B^2} \right) - \sum_{j=1}^3 \frac{1}{(8-2j)B^{2j}} \right. \\ & \left. - \frac{1}{2B^9} \ln \left( \frac{1+B}{1-B} \right) + \sum_{j=1}^4 \frac{1}{(9-2j)B^{2j}} \right). \end{aligned} \quad (7F)$$

Since the actual transition process is more or less probabilistic in nature, it was assumed that the transition from laminar to turbulent flow can be described by the integrated normal distribution. It was necessary to assume a turbulent transition Reynolds number,  $Re_{trt}$ , for this purpose, where  $Re_{trt}$  is approximately four times  $Re_{tr}$ . The transition computation was made with the error function, erf, which is exactly related to the integrated normal distribution. The argument of the error function was formed in terms of base distance from the initial transition point, and was weighted



so its value was  $-0.96$  at  $Re_{tr}$  and  $0.96$  at  $Re_{trt}$ . A numerical span,  $S$ , of  $4.0$  takes the integrated normal distribution from  $0.02$  to  $0.98$ . Formulating these conditions in terms of body radius,  $r$ ,

$$Z_{tr} = (Re_{tr}/Re_b - 1.0)(L/r) \quad (8F)$$

is the transition point on the body measured from the base, and

$$Z_{trt} = (Re_{trt}/Re_b - 1.0)(L/r) \quad (9F)$$

is the turbulent transition point. Note that  $Z_{trt}$  will lie downstream of the base if  $Re_{trt} > Re_b$ . Forming the average,

$$Z_{trav} = \frac{1}{2}(Z_{tr} + Z_{trt}) \quad (10F)$$

is the distance from the base to the center of the transition zone. If  $Z_{trav}$  is zero, the integral of the cumulative distribution must be  $0.5$ . The value of  $erf$  at this point will be  $0.0$ , and the cumulative distribution integral,  $I_{CD}$ , is

$$I_{CD} = \frac{1}{2}(1 + erf). \quad (11F)$$

The values of  $erf$  at the base,  $ERF_b$ , range from  $-1.0$  to  $+1.0$ . In terms of  $Z$

$$ERF_b = erf\left(\frac{S}{2^{1/2}} \frac{Z_{trav}}{(Z_{trt} - Z_{tr})}\right) \quad (12F)$$

Then, when  $Re_b > Re_{tr}$ ,  $\delta_{BASE}$  is given by

$$\delta_{BASE} = \frac{1}{2}\delta_L(1 + ERF_b) + \frac{1}{2}\delta_T(1 - ERF_b). \quad (13F)$$





In Eqn. (13F),  $ERF_b$  will be positive if  $Re_b$  is less than  $\frac{1}{2}(Re_{tr} + Re_{trt})$ , thus as  $Re_b$  ranges from  $Re_{tr}$  to  $Re_{trt}$ , the contribution of  $\delta_L$  will range from 0.99 to 0.01 and the contribution of  $\delta_T$  will range from 0.01 to 0.99. The value for  $n$  used to compute the velocity profile at the base (see Appendix D) is formed exactly as Eqn. (13F)

$$n_{BASE} = \frac{1}{2}(1 + ERF_b) + \frac{7}{2} (1 - ERF_b) \quad (14F)$$

since  $n$  ranges from 1 to 7.

When the transition zone lies along the shear layer, one must compute a transition value for the mixing coefficient,  $k$ , at the point being considered,  $x_{BL}$ . The distance  $x_{BL}$  is measured from the base in terms of  $r$ . To carry out this calculation, the value of erf at  $x_{BL}$ ,  $ERF_{BL}$ , is written, as in Eqn. (12F), in terms of  $Z$

$$ERF_{BL} = \text{erf}\left(\frac{S}{2^{\frac{1}{2}}} \frac{(Z_{trav} - x_{BL})}{(Z_{trt} - Z_{tr})}\right). \quad (15F)$$

Note that Eqn. (15F) reduces to (12F) since  $x_{BL}$  is zero at the base. Using Eqn. (15F), the value for the coefficient,  $k_{BL}$ , is formed in a similar manner from the laminar and turbulent mixing coefficients,  $k_L$  and  $k_T$ ,

$$k_{BL} = \frac{1}{2}k_L(1 + ERF_{BL}) + \frac{1}{2}k_T(1 - ERF_{BL}). \quad (16F)$$

In Eqn. (16F), the value of  $ERF_{BL}$  will be positive if  $Z_{trav}$  is downstream of  $x_{BL}$ , and vice versa.



# APPENDIX G: DERIVATION OF LINEARIZED STEADY FLOW EQUATION WITH HEAT ADDITION

The equations, (1) - (4), are required for this derivation.

$$\nabla \cdot (\rho \bar{U}) = 0 \quad (1G)$$

$$\rho \bar{U} \cdot \nabla \bar{U} = - \nabla p \quad (2G)$$

$$\bar{U} \cdot \nabla (h + \frac{1}{2} \bar{U} \cdot \bar{U}) = q \quad (3G)$$

$$p = \rho RT \quad (4G)$$

Forming the directional derivative,  $\bar{U} \cdot \nabla$ , of Eqn. (4G)

$$\bar{U} \cdot \nabla p = \rho R \bar{U} \cdot \nabla T + RT \bar{U} \cdot \nabla \rho. \quad (5G)$$

Substituting Eqn. (1G) into (5G)

$$\rho R \bar{U} \cdot \nabla T = \bar{U} \cdot \nabla p + \rho RT \nabla \cdot \bar{U} \quad (6G)$$

Substituting  $\bar{U} \cdot \nabla$  of Eqn. (2G) in (6G)

$$R \bar{U} \cdot \nabla T = - \bar{U} \cdot \nabla (\frac{1}{2} \bar{U} \cdot \bar{U}) + RT \nabla \cdot \bar{U} \quad (7G)$$

Assuming  $c_p$  is constant, using  $h = c_p T$  and  $c_p = \gamma R / (\gamma - 1)$ , substitute  $\gamma / (\gamma - 1)$  times Eqn. (7G) into (3G)

$$\nabla \cdot \bar{U} - \frac{1}{a^2} \bar{U} \cdot \nabla (\frac{1}{2} \bar{U} \cdot \bar{U}) = q / c_p T. \quad (8G)$$

Let  $T = T_\infty (1 + T')$ ,  $q = h_\infty q'$ ,  $\bar{U} = U_\infty \bar{i} + \nabla \phi$ .

With this, Eqn. (8G) becomes

$$\nabla^2 \phi - \frac{(U_\infty T + \nabla \phi) \cdot \nabla}{a_\infty^2 (1 + T')} (\frac{1}{2} U_\infty^2 + U_\infty \phi_x + \frac{1}{2} \nabla \phi \cdot \nabla \phi) = q' / (1 + T') \quad (9G)$$



Retaining only first order terms, Eqn. (9G) becomes

$$\nabla^2 \phi - M_\infty^2 \phi_{xx} = q'. \quad (10G)$$

This is the linearized steady flow equation, with heat addition for irrotation subsonic or supersonic flow.



## APPENDIX H: DETERMINATION OF THE MACH ANGLE

This appendix derives a numerical procedure for determining the Mach angle,  $\mu$ , for a given value of the Prandtl-Meyer angle,  $\nu$

The Prandtl-Meyer angle may be written [Ref. 18]

$$\nu = \frac{1}{g} \tan^{-1}(g(M^2-1)^{\frac{1}{2}}) - \tan^{-1}(M^2-1)^{\frac{1}{2}} \quad (1H)$$

where  $M$  is the Mach Number,  $1 \leq M \leq \infty$ ,

$$g = ((\gamma-1)/(\gamma+1))^{\frac{1}{2}} \quad (2H)$$

and  $\gamma$  is the specific heat ratio. Let

$$\mu + \epsilon = \pi/2 \quad (3H)$$

where  $\mu$  is the Mach angle defined by

$$\sin \mu = 1/M. \quad (4H)$$

From Eqns. (3H) and (4H)

$$(M^2-1)^{\frac{1}{2}} = \tan \epsilon. \quad (5H)$$

Using equation (5H), equation (1H) may be written

$$\tan(\nu+\epsilon) = g \tan \epsilon. \quad (6H)$$

In Eqn. (6H), the relation between  $\nu$  and  $\epsilon$  is still implicit.

For  $\gamma = 5/3$ ,  $g = \frac{1}{2}$  and Eqn. (6H) can be reduced to the explicit form

$$\tan^3 \frac{\epsilon}{2} = \tan \frac{\nu}{2}. \quad (7H)$$

Thus, using Eqns. (3H) and (7H), the simple relation may be written when  $\gamma = 5/3$





$$\mu = \frac{\pi}{2} - 2 \tan^{-1} \left( \left( \tan \frac{\nu}{2} \right)^{1/3} \right). \quad (8H)$$

This analytical result [Ref. 37] was first given in terms of  $M$ , rather than  $\mu$ , along with a more complicated expression when  $\gamma = 5/4$ . There are no analytical expressions,  $\mu = \mu(\nu, \gamma)$ , for other values of  $\gamma$ , consequently,  $\mu$  must be determined from tables, or numerically, in all other cases.

Equation (6H) may be written in a form for iteration which always converges to the correct value of  $\epsilon$

$$\epsilon_{i+1} = \tan^{-1} \left( \frac{1}{g} \tan g(\nu + \epsilon_i) \right) \quad (9H)$$

for  $0 \leq \epsilon_i \leq \pi/2$  and  $0 \leq \nu \leq \nu_{\max}$ . The value  $\nu_{\max}$  is given by Eqn. (1H) for  $M$  infinite

$$\nu_{\max} = \frac{\pi}{2} \left( \left( (\gamma+1)/(\gamma-1) \right)^{1/2} - 1 \right). \quad (10H)$$

One may start the iteration of Eqn. (9H) with an approximation for  $\epsilon_1$  given by Eqn. (7H)

$$\epsilon_1 = 2 \tan^{-1} \left( \left( \tan \frac{\nu}{2} \right)^{1/3} \right). \quad (11H)$$

This approximation fails for large values of  $\nu$  since it may give a value  $\epsilon_1 > \pi/2$ . When this occurs, set  $\epsilon_1 = \pi/2$  to start the iteration with Eqn. (9H).

While Eqn. (9H) will always converge to the correct value of  $\epsilon$ , its convergence is slow and, after two or three iteration, should be replaced by a method utilizing the derivatives. In effect, Eqn. (9H) is used to find an approximation of  $\epsilon$  which lies in the range of convergence of a faster method.



One method which provides rapid convergence may be written from Eqn. (6H) by using a Taylor's series expansion for the separate sides about  $\epsilon_i$  and solving for  $\Delta\epsilon$ . Let

$$f_{1_i} = \text{tang}(\nu + \epsilon_i) \quad (12H)$$

$$f_{2_i} = g \tan \epsilon_i \quad (13H)$$

then

$$\Delta\epsilon_{j+1} = (f_{1_i} - f_{2_i} + \frac{\Delta\epsilon_j^2}{2!} (f'_{1_i} - f'_{2_i}) + \frac{\Delta\epsilon_j^3}{3!} (f''_{1_i} - f''_{2_i}) + \dots) / (f'_{2_i} - f'_{1_i}) \quad (14H)$$

where  $\Delta\epsilon_1 = 0$  starts the iteration in Eqn. (14H). The advantage of this form lies in the fact that the derivatives may be written in terms of the values of  $f_{1_i}$  and  $f_{2_i}$ , i.e.  $f'_{1_i}$  and  $f'_{2_i}$  involve the  $\sec^2 x$ , which can be written as  $1 + \tan^2 x$ , etc. Thus the derivatives may be included with only two numerical evaluations by the computer of the tangent functions in Eqns. (12H) and (13H). Depending on the number of derivatives included, two or three iterations with Eqn. (14H) should be sufficient. Then, of course,

$$\epsilon_{i+1} = \epsilon_i + \Delta\epsilon_{j+1} \quad (15H)$$

is used to evaluate  $f_{1_{i+1}}$  and  $f_{2_{i+1}}$ , etc. For  $\gamma = 1.4$  and including the fourth derivative, the above procedure will provide twelve place accuracy for  $\epsilon$  in two iterations. With the required value for  $\epsilon$ ,  $\mu$  can be written using Eqn. (3H).

This method was used in the computer program discussed in Appendix J.



## APPENDIX I: SPINNING CYLINDER DESIGN

The spinning cylinder was designed to be compatible with the coaxial free jet fixtures, nozzles and spacers used for the nonspinning investigation [Ref. 29]. The spinning cylinder and its support assembly had the same external dimensions as the stationary cylinder design, 1.282-inch diameter and 9.95-inch length, to insure similar test results without spin. The cylinder was driven by an internal impulse turbine. The design speed of 48,000 revolutions per minute, to match the spin number of 0.1595, was not achieved. This was due in part to physical interference during the fabrication process which reduced the tangential component of the turbine jet to less than one-half the desired value. The maximum speed achieved, without nozzle flow, was 18,000 revolutions per minute.

The spinning cylinder was made of Plexiglas, to reduce rotating mass, and was glued to a metal endcap which formed the cylinder base. The endcap was driven through a shaft which screwed into the internal turbine. The shaft also carried thrust loads, from an internal air bearing surface on the turbine face, to react with pressure and friction forces due to the nozzle flow. This part of the design was deficient in that the loads due to nozzle flow caused the turbine face to rub and stopped the cylinder. Time did not permit modification to correct this deficiency.



The spinning cylinder was positioned radially by 24 air bearing pads provided along the outer surface of the support cylinder. High pressure air was supplied to these pads through orifices formed by drilling into supply tubes soldered into the walls of the support cylinder, Fig. 11. The bearing air exhausted through ports to the inside of the support cylinder where it mixed with turbine exhaust and flowed out the bottom.

The base pressure on the spinning cylinder was measured by a total pressure probe, positioned on centerline next to the base, and a mercury manometer. The cylinder speed was determined through a photo diode and a pulse counter. The photo diode was illuminated by a laser beam reflecting from the metal endcap and half of the endcap was painted black to generate one pulse per revolution.

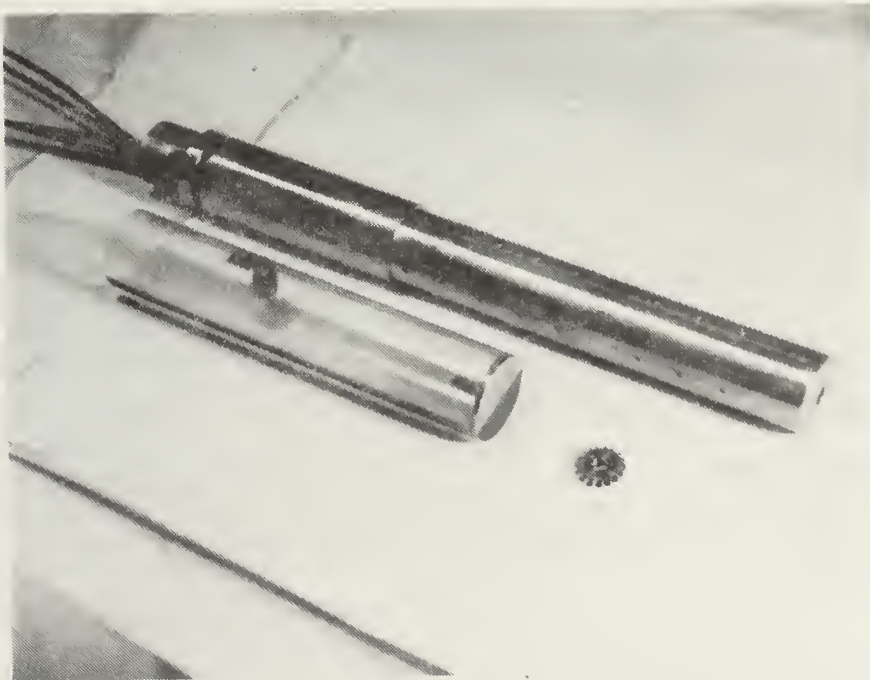


Figure 11. Disassembled View of Spinning Cylinder.





## APPENDIX J: COMPUTER PROGRAM

The FORTRAN computer program, included at the end of this appendix, required 150K for compile, 110K for link and 80K for execution. It was written to compute base pressure ratio, within approximately 0.5 percent, by applying the equations and methods discussed in this thesis. In view of the empirical information and approximations employed in many of the equations, computation to greater accuracy did not appear warranted. Using an IBM 360 computer, computation of the base pressure ratio for one flight condition required approximately two minutes for the fully turbulent shear layer without heat addition. The addition of heat upstream of the base and low Reynolds number, which involved a long laminar shear layer, increased the size of the characteristic mesh and resulted in computation times as high as ten minutes.

The flight condition was specified before making a computer run. This included choosing the Mach number, card 80, and the base Reynolds number, card 140. The two no spin transition Reynolds numbers, cards 120 and 130, were chosen for the particular body to provide agreement with available experimental data. The ratio of body radius to body length was specified on card 150. The spin number,  $rw/U$ , was given on card 131. The ratio of specific heats for air was set at 1.4 on card 200. Card 180 and 190 were interchanged for two dimensional planar flow. For flow without heat addition,



card 90 was set to zero, card 60 to  $ISTRT = 90$ , and card 100 to  $ZSTRT = 20.0$ .

Several additional considerations were required to compute the flight condition with external burning. The starting values for the radii of the heat zone inner and outer streamlines were specified on cards 420 and 430. The axial positions to start and stop heat addition were given on cards 100 and 110, with reference to the base. The value for  $Q$ , card 90, was specified to obtain a desired  $-4\frac{1}{2}^\circ$  deflection of the inner heat zone streamline, however, this value could have been specified by assuming various fuel flow rates and heating values. Finally, the value for  $ISTRT$ , card 60, was set low enough (minimum value of 1) to place the Mach line boundary condition well upstream of the outer compression waves generated by the heat zone. The values of selected quantities were printed, to monitor the progress of the computation, in addition to the required values for the base pressure ratio.

A simplified flow diagram is shown in Fig. 1J. It is intended to show the basic sections of the computer program and computational details have been omitted.

In the computer program the group of IF STATEMENTS which examine the mesh point for heat addition can introduce a slight error at two corners of the heat zone. The amount of heat assigned between two points is proportional to the element of length along the characteristic in the heat zone. The IF condition is checked in radial position against the



START

ESTABLISH FLIGHT CONDITION VARIABLES:

$M$ ,  $Re_b$ ,  $Re_{tr}$ ,  $Re_{trt}$ ,  $\gamma$ ,  $k_L$ ,  $k_T$ ,  $r/L$ ,  $\alpha$ , Heat  
Zone ( $Q, Z_{start}, Z_{stop}, R_{is}, R_{os}$ ),  $Spin$ ,  $I_{start}$  for  
Characteristic Mesh Upstream of Base to  
Enclose Heat Zone ( $Z_{mesh\ start} = -0.1(100-I)$ ).

Compute Base Boundary Layer:  $r/\delta$  and  $n$ .

Compute Characteristic Mesh Along Body and  
Through Heat Zone Up to the Base. Store Values  
Along Base Characteristic to Reset for the  
Straddle Method.

Compute Mass Flux at the Base.

Assign Value of  $w_e$  for Straddle Method.  
Compute Expansion Fan and  $F$ .

Compute Increment Along Shear Layer from  
 $dF = -0.1F$ ,  $dw_e = dF/(dF/dw_e)$  and  
 $m_{i+1} = m_i + (dm/dx)dx$ .

Compute Characteristic from Shear Layer to  
Upstream Mach Line. Correct  $\theta$  at Shear Layer

Proceed Along Shear Layer Until Critical Point  
Where  $dF/dw_e$  Becomes Negative. Compute  $p_b/p_\infty$   
from Value of  $w_e$  at Base. Assign Next Value of  
 $w_e$  at Base from Sign of  $dF/dw_e$  Numerator.

STRADDLE LOOP

STOP

Figure 1J. Simplified Flow Diagram for External Burning Assisted Projectile (EBAP) Computer Program.



inner and outer streamlines of the heat zone, and in axial position against the start and end of the heat zone. Thus a right running element at the lower left or upper right corner of the heat zone could be outside the zone, but still pass the IF condition tests and be assigned  $\frac{1}{4}$  value for heating. This error is small with a small characteristic mesh and is neglected. The same applies to a left running element at the upper left or lower right corner of the heat zone.





```

C
EBAP PRGGRAM
DIMENSION QR(200), QZ(200), QT(200), QUN(200), QUM(200), QACH(200)
1, QDEG(202), BL(200), VR(200), VZ(200), VT(200), VUM(200)
2, VACH(200), RSR(100), RSZ(100), RST(100), RSUN(100), RSUM(100),
3, VACH(100)
1, I=90
V=1.95
ACH=2.0
Q=0.0
ZSTRT=20.0
ZBYH=4.0
ZSTOP=ZSTRT+WBYPH
ZRETN=1.95
RETN=4.0*RETN
SPIN=0.06
RETR=RETN/(1.0+SPIN)
RETRT=RETR/(1.0+SPIN)
REL=15.29086
RBYL=0.1
BKLT=0.0033
IXA=0
IXA=1
G=1.4
SPAND=4.0
VSTRT=V
PIBY2=1.570796
TENLG=ALOG(10.0)
SQ2RT=SQRT(2.0)
AK1=0.72
THCO=-0.000001
TH01=0.000001
TH10=100.0*TH01
UMGO=ARCSIN(1.0/ACH0)
G1=0.5*(G-1.0)
G2=G/(G-1.0)
G3=SQRT((G+1.0)/(G-1.0))
G4=0.5*(G+1.0)
G6=1.0/(G-1.0)
G7=1.0/G3
UNMAX=PIBY2*(G3-1.0)-0.00029
SHOCK=9.99991
CL3=0.33333
START LOOP ON REYNOLDS NUMBER, REL
DC 1052 IREL=1,1
RCS=2.0
RCS=3.0
RELG=100.0*1000.0*REL

```



```

EBAP 450
EBAP 460
EBAP 470
EBAP 480
EBAP 490
EBAP 500
EBAP 510
EBAP 520
EBAP 530
EBAP 540
EBAP 550
EBAP 560
EBAP 570
EBAP 580
EBAP 590
EBAP 600
EBAP 610
EBAP 620
EBAP 630
EBAP 640
EBAP 650
EBAP 660
EBAP 670
EBAP 680
EBAP 690
EBAP 700
EBAP 710
EBAP 720
EBAP 730
EBAP 740
EBAP 750
EBAP 760
EBAP 770
EBAP 780
EBAP 790
EBAP 800
EBAP 810
EBAP 820
EBAP 830
EBAP 840
EBAP 850
EBAP 860
EBAP 870
EBAP 880
EBAP 890
EBAP 900
EBAP 910
EBAP 920

```

BKL=BKL1\*SQRT(RETR/REL)  
 ZTRT=(RETR/REL-1.0)/RBYL  
 ZTRT=(RETR/REL-1.0)/RBYL  
 ZTRAV=0.5\*(ZTR+ZTRT)  
 XCONV=(SPAND/(ZTRT-ZTR))/SQ2RT  
 ACH=ACH0  
 ACH2=ACH\*ACH  
 G5=SQRT(ACH2-1.0)  
 UN00=G3\*ATAN(G5/G3)-ATAN(G5)  
 W2=ACH2/(1.0+G1\*ACH2)  
 W=SQRT(W2)  
 NBL=1  
 RBYBL=200.0\*RBYL\*(SQRT(REL))/(1.0+0.48\*G1\*ACH2)  
 IF (ZTR.GE.0.0) GO TO 1004  
 BLERF=0.5\*ERF(ZTRAV\*XCONV)  
 BETA2=G1\*W2  
 BETA=SQRT(BETA2)  
 BLTKS=1.0/(BETA2\*\*4)  
 BLTKS=BLTKS\*(1.0+0.5\*(ALOG(1.0/(1.0-BETA2))-(1.0/BETA)\*ALOG((1.0+BETA)  
 1  
 LGCP FOR PART OF BL (MOMENTUM THKNSS)/(THKNSS)  
 DO 1001 J=1,3  
 BLTKS=BLTKS+(1.0/(9.0-2.0\*J)-1.0/(8.0-2.0\*J))/(BETA2\*\*J)  
 1001  
 COMPUTE BL (MOMENTUM THKNSS)/(THKNSS), BLTKS  
 BLTKS=7.0\*(1.0-BETA2)\*BLTKS  
 BETAAL=1.26\*(ALOG(1.0-BETA2))/TENLG  
 BETAA=(0.242/BETA)\*(ARSIN(BETA))\*SQRT(1.0-BETA2)  
 CFI=0.003  
 SCOLVE INCOMPRESSIBLE FRICTION COEFFICIENT, CFI  
 DO 1002 J=1,5  
 CFFI={ALOG(CFI\*REL6))/TENLG-0.242/SQRT(CFI)  
 DCFFI=1.0/(CFI\*TENLG)+(0.121/CFI)/SQRT(CFI)  
 CFI=CFI-DCFFI  
 1002  
 COMPUTE CFC-CFFI  
 ESTIMATE CFC-CFFI  
 CFC=CFI\*(1.0-0.08\*ACH0)  
 SCOLVE FOR CFC  
 DO 1003 J=1,5  
 CFFC={ALOG(CFC\*REL6))/TENLG+BETAL-BETAA/SQRT(CFC)  
 DCFFC=1.0/(CFC\*TENLG)+(0.5\*BETAA/CFC)/SQRT(CFC)  
 CFC=CFC-DCFFC  
 1003  
 COMPUTE (RADIUS)/(TURB BL THKNSS), RBYBT  
 RBYBT=270.5\*RBYL\*((10.0\*REL)\*\*0.2)\*{(CFI/CFC)\*BLTKS  
 RBYBL=RBYBT\*(0.5+BLERF)+RBYBT\*(0.5-BLERF)  
 NBL=1.2\*(0.5+BLERF)+7.2\*(0.5-BLERF)  
 1004  
 CONTINUE



```

TIS=TH00
TIDEG=57.3*TIS
TCS=TH00
P=(1.0-G1*W2)**G2
PC0=p
P7=P
MSTR=98
BTR=1.0
BTR IS BL(100)/BL(ISTRT) WHEN BCATTAIL IS PRESENT
DW=-0.1
ISTPL=ISTRT+1
BL(ISTRT)=1.0+1.0/RBYBL
DZC=0.1*(100-MSTBT)
DZC2=DZC*DZC
DZC=(1.0/BTR-1.0)/DZC2
VR(ISTRT)=BL(ISTRT)
GR(ISTRT)=VR(ISTRT)
VZ(ISTRT)=-DZ*(100-ISTRT)
VT(ISTRT)=VZ(ISTRT)
GT(ISTRT)=TH00
VUN(ISTRT)=UN00
VUM(ISTRT)=UM00
VUM(ISTRT)=UM00
VACH(ISTRT)=ACH0
QACH(ISTRT)=ACH0
ZLS=VZ(ISTRT)+(RIS-VR(ISTRT))/TAN(UM00+TH00)
ZCS=VZ(ISTRT)+(ROS-VR(ISTRT))/TAN(UM00+TH00)
BTDRG=0.0
M=ISTRT
QDEG(M)=0.0
WRITE (6,1053) M,VR(M),VZ(M),VT(M),VACH(M),VT(ISTRT),QDEG(M),BTDRG
PMCOR=0.0
START INCREMENTING CHARACTERISTIC MESH ALONG BODY
DO 1016 M=ISTPL,100
M7=M-1
MM100=M-ISTRT
MM99=MM100+1
MMID=ISTRT+(M-ISTRT)/2
DZB=DZ*(M-MSTBT)
BL(M)=BL(ISTRT)/(1.0+BTC*DZB*DZB)
IF (M.LE.MSTBT) BL(M)=BL(ISTRT)
QR(M)=BL(M)
GZ(M)=-DZ*(100-M)
SLP=-2.0*BTC*DZB*BL(M)*BL(M)/BL(ISTRT)
SLP=TH00

```

C

C



```

C      REMOVE SLP=TH00 WHEN PROVIDING BOATTAIL SHAPE
      IF (M.LE.MSTBT) SLP=TH00
      QT(M)=ATAN(SLP)
      QUN(M)=VUN(M7)+VT(M7)-QT(M)+PMCCR
      ABFN1=1.0
      ABFT1=1.0
      UNCMP=2.0
      JXCCR=0
      WCRK BACKWARDS ALONG RIGHT RUNNING CHARACTERISTIC FROM BODY TO
      UPSTREAM MACH LINE BC
      DO 1013 JX=1,12
      UNI=QUN(M)
      IF (UNI.LT.TH01) WRITE (6,1054) M,M,M,M,JX,UNI,QTUNM,QTUNP
      IF (UNI.LT.TH01) UNI=TH01
      IF (UNI.GE.UNMAX) WRITE (6,1054) M,M,M,M,JX,UNI,QTUNM,QTUNP
      IF (UNI.GE.UNMAX) UNI=UNMAX+TH00
      GE=2.0*ATAN((TAN(G7*UNI))**C13)
      IF (GE.GT.PIBY2) GE=PIBY2
      GE=ATAN(G3*TAN(G7*(UNI+GE)))
      GE=ATAN(G3*TAN(G7*(UNI+GE)))
      CCMPUTE MACH ANGLE COMPLEMENT ON BODY
      DO 1005 JY=1,2
      G10=TAN(G7*(UNI+GE))
      G20=G7*TAN(GE)
      G11=G7*(1.0+G10*G10)
      G21=G7+G3*G20*G20
      G12=G7*G10*G11*2.0
      G22=G3*G20*G21*2.0
      G13=G7*(G11*G11+G10*G12)*2.0
      G23=G7*(G21*G21+G20*G22)*2.0
      G14=G7*(G12*(2.0*G11+G12)+G10*G13)*2.0
      G24=G3*(G22*(2.0*G21+G22)+G20*G23)*2.0
      G30=G10-G20
      G31=G21-G11
      G32=(G12-G22)/(2.0*G31)
      G33=(G13-G23)/(6.0*G31)
      G34=(G14-G24)/(24.0*G31)
      DGE1=G30/G31
      DGE=DGE1
      DGE=DGE1+DGE*DGE*(G32+DGE*(G33+DGE*G34))
      DGE=DGE1+DGE*DGE*(G32+DGE*(G33+DGE*G34))
      DGE=DGE1+DGE*DGE
      CCNTINUE
      MACH ANGLE ON BODY
      QUM(M)=PIBY2-GE
      QACH(M)=1.0/(SIN(QUM(M)))
      CCMPUTE EACH CHARACTERISTIC POINT
      DO 1011 J=1,MM100

```





```

J0=M-J
J1=J0+1
VUM=VT=TAN(VUM(J0)+VT(J0))
QUKQT=TAN(QUK(J1)-QT(J1))
RITAN=TAN(TIS)
RCTAN=TAN(TCS)
TJ0=VUMVT+TAN(QUK(J0)+QT(J0))
TJ1=QUKQT+TAN(QUK(J1)-QT(J1))
QZ(J0)=(2.0*(QR(J1)-VR(J0))+TJ0*VZ(J0)+TJ1*QZ(J1))/(TJ0+TJ1)
QZ(J1)=VR(J0)+0.5*TJ0*(QZ(J0)-VZ(J0))
DETA=SQRT((QR(J0)-VR(J0))*2+(QZ(J0)-VZ(J0))*2)
DXI=SQRT((QR(J0)-VR(J1))*2+(QZ(J1)-QZ(J0))*2)
ZINT=(QR(J0)-RIS+RITAN*ZIS+TJ1*QZ(J0))/(RITAN+TJ1)
RINT=RIS+(ZINT-ZIS)*RITAN
ZCTR=(QR(J0)-RGS+ROUTAN*ZOS+TJ1*QZ(J0))/(ROUTAN+TJ1)
RCTR=RGS+(ZCTR-ZOS)*ROUTAN
ZINV=(RIS-QR(J0)+TJ0*QZ(J0)-RITAN*ZIS)/(TJ0-RITAN)
RINV=RIS+(ZINV-ZIS)*RITAN
ZOTV=(RGS-QR(J0)+TJ0*QZ(J0)-ROUTAN*ZOS)/(TJ0-ROUTAN)
ZOTV=RGS+(ZOTV-ZOS)*ROUTAN
RAVG=0.5*(VR(J0)+QR(J0))
THAVG=0.5*(VUM(J0)+QUK(J0))
GEAT=0.5*(VT(J0)+QT(J0))
IF (QZ(J0).LT.ZSTRT) GO TO 1006
IF (VZ(J0).GT.ZSTOP) GO TO 1006
IF (QR(J0).LT.RINV) GO TO 1006
IF (VR(J0).GT.ROTV) GO TO 1006
GEAT=1.0
IF (VZ(J0).LT.ZSTRT) GEAT=GEAT*(QZ(J0)-ZSTRT)/(QZ(J0)-VZ(J0))
IF (QZ(J0).GT.ZSTOP) GEAT=GEAT*(ZSTOP-VZ(J0))/(QZ(J0)-VZ(J0))
IF (VR(J0).LT.RINV) GEAT=GEAT*(QR(J0)-RINV)/(QR(J0)-VR(J0))
IF (QR(J0).GT.ROTV) GEAT=GEAT*(ROTV-VR(J0))/(QR(J0)-VR(J0))
1006 CONTINUE
QTUM=VT(J0)-VUN(J0)-(SIN(UMAVG))*(IXA*(SIN(THAVG))/RAVG-Q*GEAT)*D
1
ETA
RAVG=0.5*(QR(J0)+QR(J1))
UMAVG=0.5*(QUK(J0)+QUK(J1))
THAVG=0.5*(QT(J0)+QT(J1))
ACHAV=0.5*(QACH(J0)+QACH(J1))
ACAV2=ACHAV*ACHAV
HEAT=0.0
IF (QZ(J1).LT.ZSTRT) GO TO 1007
IF (QZ(J0).GT.ZSTOP) GO TO 1007
IF (QR(J0).LT.RINT) GO TO 1007
IF (QR(J1).GT.ROTR) GO TO 1007
HEAT=1.0
IF (QZ(J0).LT.ZSTRT) HEAT=HEAT*(QZ(J1)-ZSTRT)/(QZ(J1)-QZ(J0))

```

EBAPI1870  
 EBAPI1880  
 EBAPI1890  
 EBAPI1900  
 EBAPI1910  
 EBAPI1920  
 EBAPI1930  
 EBAPI1940  
 EBAPI1950  
 EBAPI1960  
 EBAPI1970  
 EBAPI1980  
 EBAPI1990  
 EBAPI2000  
 EBAPI2010  
 EBAPI2020  
 EBAPI2030  
 EBAPI2040  
 EBAPI2050  
 EBAPI2060  
 EBAPI2070  
 EBAPI2080  
 EBAPI2090  
 EBAPI2100  
 EBAPI2110  
 EBAPI2120  
 EBAPI2130  
 EBAPI2140  
 EBAPI2150  
 EBAPI2160  
 EBAPI2170  
 EBAPI2180  
 EBAPI2190  
 EBAPI2200  
 EBAPI2210  
 EBAPI2220  
 EBAPI2230  
 EBAPI2240  
 EBAPI2250  
 EBAPI2260  
 EBAPI2270  
 EBAPI2280  
 EBAPI2290  
 EBAPI2300  
 EBAPI2310  
 EBAPI2320  
 EBAPI2330  
 EBAPI2340



```

IF (QZ(J1).GT.ZSTOP) HEAT=HEAT*(ZSTOP-QZ(J0))/(QZ(J1)-QZ(J0))
IF (QR(J1).LT.RINT) HEAT=HEAT*(QR(J0)-RINT)/(QR(J0)-QR(J1))
IF (QR(J0).GT.ROTR) HEAT=HEAT*(ROTR-QR(J1))/(QR(J0)-QR(J1))
1007 CONTINUE
QTUNP=QT(J1)+QUN(J1)-(SIN(UMAVG))*(IXA*(SIN(THAVG))/RAVG-Q*HEAT)*D
1 XI (JO)=0.5*(QTUNM+QTUNP)
QTABS=ABS(QT(J0))
IF (QTABS.LT.TH01) QT(J0)=TH00
IF (ABFNI.GT.TH10) GO TO 1008
IF (ABFTI.GT.TH10) GO TO 1008
IF (QR(J0).LT.RINT) GO TO 1008
IF (QR(J1).GT.RINT) GO TO 1008
RIS=RINT
ZIS=ZINT
TIDEG=57.3*TIS
1008 CONTINUE
IF (ABFNI.GT.TH10) GO TO 1009
IF (ABFTI.GT.TH10) GO TO 1009
IF (QR(J1).GT.ROTR) GO TO 1009
IF (QR(J0).LT.ROTR) GO TO 1009
RCS=ROTR
ZCS=ZOTR
1009 CONTINUE
QUN(J0)=0.5*(QTUNP-QTUNM)
QUNI=QUN(J0)
IF (UNI.LT.TH01) WRITE (6,1054) J,J,M,M,M,UNI,QTUNM,QTUNP
IF (UNI.LT.TH01) UNITE=TH01
IF (UNI.GE.UNMAX) WRITE (6,1054) J,J,M,M,M,UNI,QTUNM,QTUNP
IF (UNI.GE.UNMAX) UNI=UNMAX+TH00
GE=2.0*ATAN(TAN(G7*UNI))*C13
GE=(GE.GT.PI*2) GE=PI*2
GE=ATAN(G3*UNITE*(UNI+GE))
GE=ATAN(G3*UNITE*(UNI+GE))
COMPUTE MACH ANGLE COMPLIMENT
DO 1010 JY=1,2
G10=TAN(G7*(UNI+GE))
G20=G7*(1.0+G10*G10)
G11=G7*G3*G20*G20
G21=G7*G3*G11*2.0
G22=G3*G20*G21*2.0
G13=G7*G3*(G11*G21+G10*G12)*2.0
G23=G7*G3*(G21*G22+G10*G13)*2.0
G14=G7*G3*(G12*G22*(2.0*G21+G22)+G20*G23)*2.0
G24=G7*G3*(G22*G23*(2.0*G21+G22)+G20*G23)*2.0

```

C



EBAP2810  
EBAP2820  
EBAP2830  
EBAP2840  
EBAP2850  
EBAP2860  
EBAP2870  
EBAP2880  
EBAP2890  
EBAP2900  
EBAP2910  
EBAP2920  
EBAP2930  
EBAP2940  
EBAP2950  
EBAP2960  
EBAP2970  
EBAP2980  
EBAP2990  
EBAP3000  
EBAP3010  
EBAP3020  
EBAP3030  
EBAP3040  
EBAP3050  
EBAP3060  
EBAP3061  
EBAP3062  
EBAP3063  
EBAP3064  
EBAP3065  
EBAP3066  
EBAP3070  
EBAP3080  
EBAP3090  
EBAP3100  
EBAP3110  
EBAP3120  
EBAP3130  
EBAP3140  
EBAP3150  
EBAP3160  
EBAP3170  
EBAP3180  
EBAP3190  
EBAP3200  
EBAP3210

```

G30=G10-G20
G31=G21-G11
G32=(G12-G22)/(2.0*G31)
G33=(G13-G23)/(6.0*G31)
G34=(G14-G24)/(24.0*G31)
DGE1=G30/G31
DGE=DGE1+DGE*DGE*(G32+DGE*(G33+DGE*G34))
DGE=DGE1+DGE*DGE*(G32+DGE*(G33+DGE*G34))
DGE=GE+DGE
CONTINUE
1010 C      COMPUTE MACH ANGLE AT EACH CHARACTERISTIC PCINT
      QUM(J0)=PI*2-GE
      QACH(J0)=1.0/(SIN(QUM(J0)))
CONTINUE
1011 C      DETERMINE FACTOR FOR AND MAKE ERROR CORRECTION
      IF (JXCOR.EQ.1) GO TO 1014
      ABDEN=ABS(QUN(ISTRT))-UN00-D1FNU
      IF (ABDEN.LE.TH10) GO TO 1012
      IF (JX.GT.2) UNCOR=ABS(D2FNU/ABDEN)
      IF (JXCOR.LT.1.0) UNCOR=1.0
      IF (UNCOR.GT.4.0) UNCOR=4.0
      IF (JX.GT.2) UNCMP=(UNCMP*(JX-1)+UNCOR)/JX
CONTINUE
1012 C      IF (JX.GT.6) UNCMP=0.75
      D1FNU=QUN(ISTRT)-UN00
      ABFNI=ABS(D1FNU)
      D1FTH=QUN(ISTRT)-TH00
      ABFTI=ABS(D1FTH)
      IF (ABFTI.GT.TH10) GO TO 2014
      IF (ABFNI.LE.TH10) JXCOR=1
      IF (ABFNI.LE.TH10) GO TO 1013
CONTINUE
2014 D2FNU=UNCMP*D1FNU
      IF (JX.LT.12) QUN(M)=QUN(M)-D2FNU
CONTINUE
1013 C      ESTIMATE PRANDTL-MEYER CORRECTION FOR NEXT BODY POINT, COMPUTE
      FINAL ERROR OF NU AT BC POINT, CCMPUTE BOATTAIL DRAG
CONTINUE
1014 C      PMCOR=QUN(M)+QT(M)-VUN(M7)-VT(M7)
      DEGM(M)=57.3*(QUN(ISTRT)-UN00)
      P=1.0/((1.0+G1*QACH(M)*QACH(M))*G2)
      BTDRG=BTDRG-(2.0*P00-P-P7)*(BL(M7)*BL(M7)-BL(M)*BL(M))
      P7=P
      C      RESET FOR NEXT CHARACTERISTIC MESH LINE
      DO 1015 J=1,MN100
      J1=M-J+1
      VR(J1)=QR(J1)

```



EBAP33220  
EBAP332230  
EBAP332240  
EBAP332250  
EBAP332260  
EBAP332270  
EBAP332280  
EBAP332290  
EBAP33300  
EBAP33310  
EBAP33320  
EBAP33330  
EBAP33340  
EBAP33350  
EBAP33360  
EBAP33370  
EBAP33380  
EBAP33390  
EBAP33400  
EBAP33410  
EBAP33420  
EBAP33430  
EBAP33440  
EBAP33450  
EBAP33460  
EBAP33470  
EBAP33480  
EBAP33490  
EBAP33500  
EBAP33510  
EBAP33520  
EBAP33530  
EBAP33540  
EBAP33550  
EBAP33560  
EBAP33570  
EBAP33580  
EBAP33590  
EBAP33600  
EBAP33610  
EBAP33620  
EBAP33630  
EBAP33640  
EBAP33650  
EBAP33660  
EBAP33670  
EBAP33680  
EBAP33690

```

VZ(J1)=QZ(J1)
VT(J1)=QT(J1)
VUN(J1)=QUN(J1)
VUM(J1)=QUM(J1)
VACH(J1)=QACH(J1)
1015 C CONTINUE
      CCMPUTE FINAL VALUE OF THETA AT BC POINT
      QTDEG=57.3*QT(ISTR)
      WRITE (6,1055) JX,UNCMP,VZ(M),QTDEG,P,QDEG(M),RIS,TIDEG
1016 C CONTINUE
      BTDRG BASED CN P TOTAL OF 1, R OF 1, NEGLECT BL THKNESS
      BTDRG=PIBY2*BTDRG
      STCR RESET VALUES FOR BASE CHARACTERISTIC MESH LINE
      DC 1017 MRS=ISTR,100
      RSR(MRS)=VR(MRS)
      RSZ(MRS)=VZ(MRS)
      RST(MRS)=VT(MRS)
      RSUM(MRS)=VUM(MRS)
      RSUN(MRS)=VUN(MRS)
      RSACH(MRS)=VACH(MRS)
1017 C CONTINUE
      STCR RESET VALUES FOR HEAT ZONE
      RSRIS=RIS
      RSRCIS=RCIS
      RSZIS=ZIS
      RSTIS=TCIS
      RSTCS=TCIS
      NCK1=NBL/2
      NCK2=(NBL+1)/2
      NCK3=(NBL-1)/2
      RBYBL=BTNR*RYBL
      W2=1.0/(G1+1.0/(RSACH(100)*RSACH(100)))
      BETA2=G1*W2
      BETA=SQRT(BETA2)
      BMO=(0.5/(BETA**{(2*NBL+1)}))*ALOG((1.0+BETA)/(1.0-BETA))
      CCMPUTE BL MASS FLUX AT BASE
      DC 1018 J=1,NBL
      BMO=BMO-C.5/((NBL+0.5-J)*(BETA2**J))
1018 C CONTINUE
      CETERMINE IF BL VEL PROFILE EXPONENT IS ODD OR EVEN
      IF (NCK2.GT.NCK1) GO TO 1020
      BMEVN=(0.5/(BETA**{(NBL+1)}))*ALOG((1.0+BETA)/(1.0-BETA))
      CCMPUTE EVEN CONTRIBUTION
      DC 1019 J=1,NCK1
      BMEVN=BMEVN-0.5/((NCK1+0.5-J)*(BETA2**J))
1019 C CONTINUE
      CETERMINE EVEN BL MASS FLUX AT BASE

```





```

BMASS=NBL*(IXA*BMO+RBYBL*BMEVN)
GO TO 1023
1020 CONTINUE
BMCDD=(0.5/(BETA**(NBL+1)))*ALOG(1.0/(1.0-BETA2))
IF (NBL.EQ.1) GO TO 1022
C COMPUTE ODD CONTRIBUTION
DC 1021 J=1,NCK3
BMCDD=BMCDD-0.5/((NCK2-J)*(BETA2**J))
1021 CONTINUE ODD BL MASS FLUX AT BASE
C COMPUTE
1022 CONTINUE
BMASS=NBL*(IXA*BMO+RBYBL*BMCDD)
1023 CONTINUE
C NST=(IXA+RBYBL)*(1.0+RBYBL)/(AK1*P*W*BMASS)
C NST USED TO DETERMINE F AT BASE
DC 1024 I=101,111
BL(I)=BL(100)
1024 CONTINUE
C INITIAL RADIUS OF EXPANSION CORNER FAN SET
KQ=V
W2=W*W
WRITE (6,1056) G,BKLL,BKT,Q,ZSTRT,ZSTOP,NBL
WRITE (6,1056) REL,RETR,RETRI,RBYL,ACHO,RIS,IXA
C LCCP FOR INCREASING CLOSENESS OF STRADDLE
DC 1050 L=1,4
LL1=(L+1)/2
C LCCP UNTIL SADDLE POINT IS STRADDED
DC 1048 N=1,11
C RESET CHARACTERISTIC MESH LINE AFTER EACH INTEGRATION
DC 1025 CMRS=ISTRT,100
VR(MRS)=RSTR(MRS)
VZ(MRS)=RSTZ(MRS)
VT(MRS)=RSTT(MRS)
VUN(MRS)=RSUN(MRS)
VUM(MRS)=RSUM(MRS)
VACH(MRS)=RSACH(MRS)
1025 CONTINUE
C RESET HEAT ZONE AFTER EACH INTEGRATION
RIS=RSRIS
RUS=RSRUS
ZIS=RSZIS
ZUS=RSZUS
TIS=RSSTIS
TUS=RSSTUS
XBL=0.0
C SET COORDINATES OF EXPANSION CORNER.
DC 1026 I=100,111

```



EBAP4180  
EBAP4190  
EBAP4200  
EBAP4210  
EBAP4220  
EBAP4230  
EBAP4240  
EBAP4250  
EBAP4260  
EBAP4270  
EBAP4280  
EBAP4290  
EBAP4300  
EBAP4310  
EBAP4320  
EBAP4330  
EBAP4340  
EBAP4350  
EBAP4360  
EBAP4370  
EBAP4380  
EBAP4390  
EBAP4400  
EBAP4410  
EBAP4420  
EBAP4430  
EBAP4440  
EBAP4450  
EBAP4460  
EBAP4470  
EBAP4480  
EBAP4490  
EBAP4500  
EBAP4510  
EBAP4520  
EBAP4530  
EBAP4540  
EBAP4550  
EBAP4560  
EBAP4570  
EBAP4580  
EBAP4590  
EBAP4600  
EBAP4610  
EBAP4620  
EBAP4630  
EBAP4640  
EBAP4650

```

1026 C      VR(I)=BL(100)
      VZ(I)=XB(L)
      CCONTINUE
      CCOMPUTE P RATIO AND F DOWNSTREAM OF FAN
      P=(1.0-G1*W2)**G2
      F=CNST*P*W-1.0+G1*W2
      KQ=W0
      W0=W
      W0=W2
      FQ=FF
      PO=P
      C      PNCOR=0.0
      C      INCREMENT CHARACTERISTIC MESH ALCNG SHEAR LAYER
      DC 1046 M=111,200
      MMID=(IISTRT+M)/2
      M7=M-1
      MM100=M-IISTRT
      MM95=MM100+1
      XBL7=XB(L)
      W9=1.0-G1*W2
      EM2=W2/W9
      G5=SQRT(EM2-1.0)
      EM=SQRT(EM2)
      IF (M.EQ.111) WRITE (6,1057) L,N,M,F,W,BL(111),P,EM
      IF (M.EQ.111) VACH(111)=EM
      UM=ARSIN(1.0/EM)
      IF (M.EQ.111) VUN(111)=UM
      IF (M.EQ.111) VUN(111)=VUN(111)-ATAN(G5)
      IF (M.EQ.111) VUN(111)=ENU
      IF (M.EQ.111) TH=RSUN(100)+RST(100)-ENU
      IF (M.EQ.111) VT(111)=TH
      IF (M.EQ.111) GO TO 1027
      TH=TH7+ENU7-ENU+PMCOR
1027 CCONTINUE
      CACH(M)=EM
      QUM(M)=UM
      QUN(M)=ENU
      QT(M)=TH
      IF (M.GT.111) GO TO 1030
      THCMP=(VT(111)-VT(100))/11.0
      CCOMPUTE REMAINING VALUES FOR FAN
      DC 1029 I=101,110
      IM1=I-1
      VT(I)=VT(IM1)+THCMP
      VUN(I)=VUN(100)+VT(100)-VT(I)
      QN1=VUN(I)
      IF (UNI.LT.TH01) WRITE (6,1058) L,N,M,JX,J0,UNI,QTUNM,QTUNP
      IF (UNI.LT.TH01) UNI=TH01

```



```

C
IF (UNI*GE*UNMAX) WRITE (6,1058) L,N,M,JX,JC,UNI,QTUNM,QTUNP
IF (2.0*ATAN((TAN(G7*UNI))**C13)
IF (GE*PIBY2) GE=PIBY2
GE=ATAN(G3*ATAN(G7*(UNI+GE)))
GE=ATAN(G3*ATAN(G7*(UNI+GE)))
CC COMPUTE MACH ANGLE OF EACH WAVE IN FAN
DO 1028 IX=1,2
G10=ATAN(G7*(UNI+GE))
G20=G7*ATAN(GE)
G11=G7*(1.0+G10*G10)
G12=G7*G3*G20*G20
G22=G7*G10*G11*2.0
G13=G7*G3*(G11*G11+G10*G12)*2.0
G14=G7*(G11*G21+G20*G12)*2.0
G24=G7*(G12*(2.0*G11+G22)+G20*G23)*2.0
G30=G10-G20
G31=G21-G11
G32=(G12-G22)/(2.0*G31)
G33=(G13-G23)/(6.0*G31)
G34=(G14-G24)/(24.0*G31)
DGE1=G30/G31
DGE=DGE1+DGE*DGE*(G32+DGE*(G33+DGE*G34))
DGE=DGE1+DGE*DGE*(G32+DGE*(G33+DGE*G34))
DGE=GE+DGE
1028 CONTINUE
SET IN ESTIMATED VALUES FOR NEXT COMPUTATION
VUM(I)=PIBY2-GE
VACH(I)=1.0/(SIN(VUM(I)))
QT(I)=VT(I)
QUM(I)=VUM(I)
QACH(I)=VACH(I)
CC CONTINUE KAPPA
CC COMPUTE KAPPA
1029 CONTINUE
1030 AK=1.0-(0.5-(0.29333-0.0563*F)*F)*F
DKDF=-0.5*(0.58667-0.16889*F)*F
IF (F*GT.1.5) AK=0.72
IF (F*EQ.1.5) DKDF=0.0
IF (M*EQ.111) GO TO 1044
WA=0.5*(W+W7)
WA2=WA*WA
ABFT1=1.0
ABFN1=1.0

```

```

EBAP4660
EBAP4670
EBAP4680
EBAP4690
EBAP4700
EBAP4710
EBAP4720
EBAP4730
EBAP4740
EBAP4750
EBAP4760
EBAP4770
EBAP4780
EBAP4790
EBAP4800
EBAP4810
EBAP4820
EBAP4830
EBAP4840
EBAP4850
EBAP4860
EBAP4870
EBAP4880
EBAP4890
EBAP4900
EBAP4910
EBAP4920
EBAP4930
EBAP4940
EBAP4950
EBAP4960
EBAP4970
EBAP4980
EBAP4990
EBAP5000
EBAP5010
EBAP5020
EBAP5030
EBAP5040
EBAP5050
EBAP5060
EBAP5070
EBAP5080
EBAP5090
EBAP5100
EBAP5110
EBAP5120
EBAP5130

```



```

THCMP=2.0
JXCCR=0
WCRK BACKWARDS ALCNG RIGHT RUNNING CHARACTERISTIC FROM SHEAR
LAYER TO UPSTREAM MACH LINE BC
C
DC 1041 JX=1,12
C
DETERMINE NEXT POINT ON SHEAR LAYER WITH MASS FLUX COMPUTATION
DC 1033 IBK=1,2
XBL6=0.5*(XBL7+XBL)
BLERF=0.5*ERF((ZTRAV-XBL6)*XCONV)
BK=BKL*(0.5+BLERF)+BKT*(0.5-BLERF)
X1=((1.0-G1*W2)**G2)*(W/AK)/(F+1.0-G1*W2)
X2=((BL(M7))*((1.0-G1*W72)**G2)*(W7/AK7))/(F7+1.0-G1*W72)
X3=BK*WA*((1.0-G1*WA2)**G6)
TPK=0.5*(TH+TH7)+BK
DX0=(X2-X1*BL(M7))/(X1*TPK-X3)
IF (IXA.EQ.0) GO TO 1032
DX=0.5*DX
C
C COMPUTE DX FOR AXISYMMETRIC
DC 1031 MM=1,4
DX=0.5*(DX0-TPK*DX*DX/BL(M7))
C
C CONTINUE
CAN SOMETIMES GET NEG DX IF W IS LOW AND LEFT OF SADDLE
1031
C
C CONTINUE
IF (DX.LE.0.0) ANUM=SHOCK
IF (DX.LE.0.0) GO TO 1047
BL(M)=BL(M7)+DX*TPK
XBL=XBL7+DX
1033
C
C SET MESH POINT POSITION TO SHEAR LAYER POINT
QR(M)=BL(M)
C
C COMPUTE EACH CHARACTERISTIC POINT
DC 1039 J=1,MM100
JO=M-J
J1=JO+1
VUMVT=TAN(VUM(JO)+VT(JO))
VUMQT=TAN(VUM(J1)-QT(JO))
RITAN=TAN(TIS)
RCTAN=TAN(TOS)
TJO=VUMVT+TAN(QUM(JO)+QT(JO))
TJ1=VUMQT+TAN(QUM(J1)-VT(JO))
QZ(JO)=VR(JO)+0.5*TJU*(QZ(JO)-VZ(JO))
QZ(J1)=VR(J1)+0.5*TRJ*(QZ(J1)-VZ(J1))
DETA=SQRT((QR(JO)-VR(JO))**2+(QZ(JO)-VZ(JO))**2)
DXI=SQRT((QR(J1)-VR(J1))**2+(QZ(J1)-VZ(J1))**2)
ZINT=RIIS+(ZINT-ZIS)*RITAN
RINT=RIIS+(ZINT-ZIS)*RITAN

```





```

ZCTR=(QR(JO)-RCS+ROTAN*ZOS+TJ1*QZ(JO))/(RO TAN+TJ1)
RCTR=ROCS+(ZOTR-ZOS)*RO TAN
ZINV=(RIS-QR(JO)+TJO*QZ(JO)-RITAN*ZIS)/(TJO-RITAN)
ZINV=RIS+(ZINV-ZIS)*RITAN
ZOTV=(RCS-QR(JO)+TJO*QZ(JO)-ROTAN*ZOS)/(TJO-RO TAN)
RO TV=ROCS+(ZOTV-ZOS)*RO TAN
RAVVG=0.5*(VR(JO)+QR(JO))
THAVVG=0.5*(VUM(JO)+QUM(JO))
GEAT=0.0
IF (QZ(JO).LT.ZSTRT) GO TO 1034
IF (VZ(JO).GT.ZSTOP) GO TO 1034
IF (QR(JO).LT.RINV) GO TO 1034
IF (VR(JO).GT.RO TV) GO TO 1034
GEAT=1.0
IF (VZ(JO).LT.ZSTRT) GEAT=GEAT*((QZ(JO)-ZSTRT)/(QZ(JO)-VZ(JO))
IF (QZ(JO).GT.ZSTOP) GEAT=GEAT*((QZ(JO)-ZSTRT)/(QZ(JO)-VZ(JO))
IF (VR(JO).LT.RINV) GEAT=GEAT*((QR(JO)-RINV)/(QR(JO)-VR(JO))
IF (QR(JO).GT.RO TV) GEAT=GEAT*((RO TV-VR(JO))/(QR(JO)-VR(JO))
1034 CUNTINUE
QTUNM=VT(JO)-VUN(JO)-(SIN(UMAVG))*(IXA*(SIN(THAVG))/RAVG-Q*GEAT)*D
1
1RAVG=0.5*(QR(JO)+QR(J1))
UMAVG=0.5*(QUM(JO)+QUM(J1))
THAVG=0.5*(QT(JO)+QT(J1))
HEAT=0.0
IF (QZ(J1).LT.ZSTRT) GO TO 1035
IF (QZ(JO).GT.ZSTOP) GO TO 1035
IF (QR(JO).LT.RINT) GO TO 1035
IF (QR(J1).GT.ROUT) GO TO 1035
HEAT=1.0
IF (QZ(JO).LT.ZSTRT) HEAT=HEAT*((QZ(J1)-ZSTRT)/(QZ(J1)-QZ(JO))
IF (QZ(J1).GT.ZSTOP) HEAT=HEAT*((QZ(J1)-ZSTRT)/(QZ(J1)-QZ(JO))
IF (QR(J1).LT.RINT) HEAT=HEAT*((QR(JO)-RINT)/(QR(JO)-QR(J1))
IF (QR(JO).GT.ROUT) HEAT=HEAT*((RO TR-QR(J1))/(QR(JO)-QR(J1))
CUNTINUE
1035 QTUNP=QT(J1)+QUN(J1)-(SIN(UMAVG))*(IXA*(SIN(THAVG))/RAVG-Q*HEAT)*D
1
1XI(JO)=0.5*(QTUNM+QTUNP)
QTABS=ABS(QT(JO))
IF (QTABS.LT.TH01) QT(JO)=TH00
IF (QABF1.GT.TH10) GO TO 1036
IF (ABFN1.GT.TH10) GO TO 1036
IF (QR(JO).LT.RINT) GO TO 1036
IF (QR(J1).GT.RINT) GO TO 1036
RIS=PI NT
ZIS=ZINT
TIS=QT(J1)+(QT(JO)-QT(J1))*(RINT-QR(J1))/(QR(JO)-QR(J1))

```



```

1036      ACHIS=GACH(J1)+(QACH(J0)-QACH(J1))*(RINT-QR(J1))/(QR(J0)-QR(J1))
      PRIS=1.0/(P00*(1.0+G1*ACHIS*ACHIS)**G2)
      CCNTINUE
      IF (ABFT1.GT.TH10) GO TO 1037
      IF (ABFN1.GT.TH10) GO TO 1037
      IF (QR(J1).GT.ROTR) GO TO 1037
      IF (QR(J0).LT.ROTR) GO TO 1037
      RCS=ROTR
      ZCS=ZOTR
      TOS=QT(J1)+(QT(J0)-QT(J1))*(ROTR-QR(J1))/(QR(J0)-QR(J1))
      ACHOS=QACH(J1)+(QACH(J0)-QACH(J1))*(ROTR-QR(J1))/(QR(J0)-QR(J1))
      CCNTINUE
1037      QUN(J0)=0.5*(QTUNP-QTUNM)
      QUN1=QUN(J0)
      IF (UNI.LT.TH01) WRITE (6,1058) M,N,L,JX,J0,UNI,QTUNM,QTUNP
      IF (UNI.LT.TH01) UNI=TH01
      IF (UNI.GE.UNMAX) WRITE (6,1058) M,N,L,JX,J0,UNI,QTUNM,QTUNP
      IF (UNI.GE.UNMAX) UNI=UNMAX+TH00
      GE=2.0*ATAN(TAN(G7*UNI))*C13
      IF (GE.GT.PIBY2) GE=PIBY2
      GEE=ATAN(G3*ATAN(G7*(UNI+GE)))
      GEE=ATAN(G3*ATAN(G7*(UNI+GE)))
      CCMPUTE MACH ANGLE COMPLIMENT
      DO 1038 JY=1,2,(UNI+GE)
      G10=ATAN(GE)
      G20=G7*(1.0+G10*G10)
      G11=G7*(1.0+G10*G20)
      G21=G7*(1.0+G10*G20)
      G22=G7*(1.0+G10*G21*2.0)
      G12=G7*(G11*G11+G10*G12)*2.0
      G13=G7*(G11*G11+G20*G22)*2.0
      G14=G7*(G12*(2.0*G11+G12)+G10*G13)*2.0
      G24=G7*(G12*(2.0*G21+G22)+G20*G23)*2.0
      G30=G10-G20
      G31=G21-G11
      G32=(G12-G22)/(2.0*G31)
      G33=(G13-G23)/(6.0*G31)
      G34=(G14-G24)/(24.0*G31)
      DGE1=G30/G31
      DGE=DGE1+DGE*DGE1+DGE*(G32+DGE*(G33+DGE*G34))
      DGE=DGE1+DGE*DGE1+DGE*(G32+DGE*(G33+DGE*G34))
      DGE=DGE1+DGE*DGE1+DGE*(G32+DGE*(G33+DGE*G34))
      CCNTINUE MACH ANGLE AT EACH CHARACTERISTIC PCINT
      QUN(J0)=PIBY2-GE
1038      C

```

```

EBAP6061
EBAP6062
EBAP6070
EBAP6080
EBAP6081
EBAP6090
EBAP6100
EBAP6110
EBAP6120
EBAP6130
EBAP6131
EBAP6132
EBAP6140
EBAP6150
EBAP6160
EBAP6170
EBAP6180
EBAP6190
EBAP6200
EBAP6210
EBAP6220
EBAP6230
EBAP6240
EBAP6250
EBAP6260
EBAP6280
EBAP6290
EBAP6300
EBAP6310
EBAP6320
EBAP6330
EBAP6340
EBAP6350
EBAP6360
EBAP6370
EBAP6380
EBAP6390
EBAP6400
EBAP6410
EBAP6420
EBAP6430
EBAP6440
EBAP6450
EBAP6460
EBAP6470
EBAP6490

```



```

1039 QACH(JO)=1.0/(SIN(QUM(JO)))
C CONTINUE FACTOR FOR AND MAKE ERROR CORRECTION
  IF (JXCOR.EQ.1) GO TO 1042
  ABTEN=ABS(QT(ISTRT)-TH00-D1FTH)
  IF (ABTEN.LE.TH10) GO TO 1040
  IF (JXCOR.LT.2) THCOR=ABS(D2FTH/ABTEN)
  IF (JXCOR.LT.1.0) THCOR=1.0
  IF (JXCOR.LT.4.0) THCOR=4.0
  IF (JXCOR.LT.2) THCMP=(THCMP*(JX-1)+THCOR)/JX
1040 CONTINUE
  IF (JXCOR.LT.6) THCMP=0.75
  DIFNU=QUN(ISTRT)-UN00
  ABFNI=ABS(DIFNU)
  D1FTH=QT(ISTRT)-TH00
  ABFTI=ABS(D1FTH)
  IF (ABFTI.LT.TH10) GO TO 2042
  IF (ABFTI.LE.TH10) JXCOR=1
  IF (ABFTI.LE.TH10) GO TO 1041
2042 CONTINUE
  D2FTH=THCMP*D1FTH
  IF (JXCOR.LT.12) QT(M)=QT(M)-D2FTH
  TH=QT(M)
C CONTINUE PRANDTL-MEYER CORRECTION FOR NEXT SHEAR LAYER POINT
1041 CONTINUE
1042 QDEG(M)=57.3*(QUN(ISTRT)-UN00)
  QDENU=57.3*(QUN(ISTRT)-UN00)
  BLPR=1.0/(P00*(1.0+G1*QACH(M)*QACH(M))*G2))
  IF (L.EQ.1) WRITE (6,1060) JX,N,M,BL(M),QZ(M),QT(M),QDEG(M),QDENU
  IF (L.EQ.1) WRITE (6,1060) JX,N,M,BLPR,RIS,ZIS,ROS,ZCS
  IF (L.EQ.1) WRITE (6,1060) JX,N,M,PRIS,ACHIS,PROS,ACHOS
C RESET FOR NEXT CHARACTERISTIC MESH LINE
  DO 1043 J=1,MM100
  J1=M-J+1
  VR(J1)=QR(J1)
  VZ(J1)=QZ(J1)
  VT(J1)=QT(J1)
  VUN(J1)=QUN(J1)
  VUM(J1)=QUN(J1)
  VACH(J1)=QACH(J1)
C CONTINUE
1043 CHECK FOR DFDW SIGN CHANGE, RESET FOR NEXT COMPUTATION
C CONTINUE
1044 XBL6=0.5*(XBL7+XBL)
  BLEFF=0.5*EQF((ZTRAV-XBL6)*XCONV)
  BK=BKL*(0.5+BLEFF)+RKT*(0.5-BLEFF)

```

EBAP6500  
 EBAP6510  
 EBAP6520  
 EBAP6530  
 EBAP6540  
 EBAP6550  
 EBAP6560  
 EBAP6570  
 EBAP6580  
 EBAP6590  
 EBAP6600  
 EBAP6610  
 EBAP6611  
 EBAP6612  
 EBAP6620  
 EBAP6621  
 EBAP6622  
 EBAP6623  
 EBAP6624  
 EBAP6625  
 EBAP6630  
 EBAP6650  
 EBAP6660  
 EBAP6670  
 EBAP6680  
 EBAP6690  
 EBAP6700  
 EBAP6710  
 EBAP6720  
 EBAP6730  
 EBAP6740  
 EBAP6741  
 EBAP6742  
 EBAP6750  
 EBAP6760  
 EBAP6770  
 EBAP6790  
 EBAP6790  
 EBAP6800  
 EBAP6810  
 EBAP6820  
 EBAP6830  
 EBAP6840  
 EBAP6850  
 EBAP6860  
 EBAP6870  
 EBAP6880  
 EBAP6890



```

H3=(TH/BK)*W9/(1.0-AK)
ANUM=(G4*W2-1.0)*W9+F*(G*W2-F*AK/(1.0-AK)+H3)
DEN=W*W9*(DKDF*(H3/AK)-(F/AK)/(1.0-AK))-1.0)
DFDW=ANUM/DEN
IF (DFDW.LE.0.0) GO TO 1047
FNU7=ENU
TH7=TH
F7=F
W7=W
W72=W2
AK7=AK
DFDW7=DFDW
DF=0.1*F
IF (F.LT.0.8) DF=0.08
F=F-DF
C INCREMENT W TO MATCH F AND APPROX DFDW AT NEXT POINT
DC 1045 J=1,3
W=W7-0.5*DF*(1.0/DFDW+1.0/DFDW7)
IF (W.LE.1.0) W=1.0+TH01
W2=W*W-G1*W2
W5=1.0-G1*W2
EM2=W2/W9
G5=SQR(T(EM2-1.0))
TH=TH7+ENU+PMCCR
AK=1.0-(0.5-(0.29333-0.0563*F)*F)*F
DKDF=-0.5+(0.58667-0.16889*F)*F
IF (F.GT.1.5) AK=0.72
IF (F.GT.1.5) DKDF=0.0
XBL6=0.5*(XBL7+XBL)
BLERF=0.5*ERF((ZTRAV-XBL6)*XCONV)
BK=8KL*(0.5+BLERF)+BKT*(0.5-BLERF)
H3=(TH/BK)*W9/(1.0-AK)
ANUM=(G4*W2-1.0)*W9+F*(G*W2-F*AK/(1.0-AK)+H3)
DEN=W*W9*(DKDF*(H3/AK)-(F/AK)/(1.0-AK))-1.0)
DFDW=ANUM/DEN
IF (DFDW.LE.0.0) GO TO 1047
C 1045
CONTINUE W FOR NEXT POINT
COMPUTE W FOR NEXT POINT
W=W7-0.5*DF*(1.0/DFDW+1.0/DFDW7)
W2=W*W
IF (W.LE.1.0) WRITE (6,1059) W,W2,W,W2,W,W2
IF (F.LE.0.7) GO TO 1051
IF (W.LE.1.0) GO TO 1049
IF (W.GT.2.2) GO TO 1047
C 1046
CONTINUE DRAG, INCREMENT W FOR NEXT INTEGRATION OF STRADDLE METHOD
C 1047
CONTINUE

```

EBBAP6990  
 EBBAP6910  
 EBBAP6920  
 EBBAP6930  
 EBBAP6940  
 EBBAP6950  
 EBBAP6960  
 EBBAP6970  
 EBBAP6980  
 EBBAP6990  
 EBBAP7000  
 EBBAP7010  
 EBBAP7020  
 EBBAP7030  
 EBBAP7040  
 EBBAP7050  
 EBBAP7060  
 EBBAP7070  
 EBBAP7080  
 EBBAP7090  
 EBBAP7100  
 EBBAP7110  
 EBBAP7120  
 EBBAP7130  
 EBBAP7140  
 EBBAP7150  
 EBBAP7160  
 EBBAP7170  
 EBBAP7180  
 EBBAP7190  
 EBBAP7200  
 EBBAP7210  
 EBBAP7220  
 EBBAP7230  
 EBBAP7240  
 EBBAP7250  
 EBBAP7260  
 EBBAP7270  
 EBBAP7280  
 EBBAP7290  
 EBBAP7300  
 EBBAP7310  
 EBBAP7320  
 EBBAP7330  
 EBBAP7340  
 EBBAP7350  
 EBBAP7360  
 EBBAP7370





```

IF (M.GT.111) WRITE (6,1060) L,N,M7,F7,W7,BL(M7),XBL7,ANUM
PBYP0=P0/P00
BDRAG=2.0*PIBY2*(P0-P00)*BTR*BTR
TDRAG=BDRAG+BTDRG
WRITE (6,1061) PBYP0,BTDRG,BDRAG,TDRAG
IF (ANUM.GT.0.0) GO TO 1049
W=X+DW
IF (W.LE.1.0) WRITE (6,1059) W,W,W,W,W,W
IF (W.LE.1.0) GO TO 1049
C=MINUE
1048 C=STRADLE
C=MINUE
1045 CC=K00
DW=K00/SHOCK
W=X+DW
W2=W*W
1050 C=MINUE
1051 CC=K00
PBYP0=P0/P00
BDRAG=2.0*PIBY2*(P0-P00)*BTR*BTR
TDRAG=BDRAG+BTDRG
WRITE (6,1061) PBYP0,BTDRG,BDRAG,TDRAG
V=V*STRT
1053 C=MINUE
1054 C=FORMAT(1,1112,7E16.7)
1055 C=FORMAT(1,15112,3E16.7)
1056 C=FORMAT(1,1112,7E16.7)
1057 C=FORMAT(1,15112,7E16.7)
1058 C=FORMAT(1,13112,3E16.7)
1059 C=FORMAT(1,15112,3E16.7)
1060 C=FORMAT(1,15112,3E16.7)
1061 C=FORMAT(1,14E16.7)
STOP
END

```

```

EBAP7330
EBAP7390
EBAP7400
EBAP7410
EBAP7420
EBAP7430
EBAP7440
EBAP7450
EBAP7460
EBAP7470
EBAP7480
EBAP7490
EBAP7500
EBAP7510
EBAP7520
EBAP7530
EBAP7540
EBAP7550
EBAP7560
EBAP7570
EBAP7580
EBAP7590
EBAP7600
EBAP7610
EBAP7620
EBAP7630
EBAP7640
EBAP7650
EBAP7660
EBAP7670
EBAP7680
EBAP7690
EBAP7700
EBAP7710
EBAP7720
EBAP7730
EBAP7740

```



## LIST OF REFERENCES

1. Fuhs, A. E., Smithey, W., and Naber, M. E., "Axisymmetric Analysis of External Burning Assisted Projectile," 9th JANNAF Combustion Meeting, Vol. II (CPIA Pub. 231, Dec. 1972), pp. 384-416. Inc. many refs.
2. Tsien, H. S., and Beilock, M., "Heat Sources in a Uniform Flow," J. Aero. Sci., 16, p. 756, 1949.
3. Beilock, Milton, "Heat Sources in a Compressible Fluid." Master of Science Thesis, Massachusetts Institute of Technology, 1949.
4. Rues, D., "Concerning the Equivalence Between Heat, Force and Mass Sources," RAE Lib. Trans. No. 1119, July 1965.
5. Fuhs, A. E., "Quasi Area Rule for Heat Addition in Transonic and Supersonic Flight Regimes," Technical Report AFAPL-TR-72-10, Aug. 1972.
6. Strahle, W. C., "Combustion Effects on Base Pressure in Supersonic Flight and Application," IDA Research Paper P-389, Feb. 1968.
7. Strahle, W. C., "Theoretical Consideration of Combustion Effects on Base Pressure in Supersonic Flight," Twelfth Symposium on Combustion, Combustion Institute, Pittsburgh., pp. 1163-1173, 1969.
8. Crocco, L., and Lees, L., "A Mixing Theory for the Interaction Between Dissipative Flows and Nearly Isentropic Streams," J. Aero. Sci., 19, pp. 649-676, 1952.
9. Billig, F. S., "External Burning in Supersonic Streams," The Johns Hopkins University Applied Physics Laboratory, TG-912, May 1967.
10. Serafini, J. I., *et. al.*, "Exploratory Investigation of Static and Base Pressure Increases Resulting from Combustion of Aluminum Borohydride Adjacent to a Body of Revolution in a Supersonic Wind Tunnel," NACA RME57E15, Oct. 2, 1957.
11. Hosack, G. A., O'Learly, R. A., and Schnurstein, R. E., "External Burning Propulsion." 10th JANNAF Combustion Meeting, Vol. IV (CPIA Pub. 243, Dec. 1973) pp. 43-55.



12. Davis, D. D., "Extension of Simplified Mixing Theory to Axially Symmetric Supersonic Wake Flows and Application to Base Pressure Problem for a Body of Revolution," Princeton University, M.Sc. Thesis, 24-V-1952.
13. de Krasinski, J. S. A., "A Study of Axially Symmetrical Base Flow Behind Bodies of Revolution at Supersonic Speeds," AGARD Conference Proceedings No. 4 on Separated Flows, Part 2, pp. 747-771, May 1966.
14. de Krasinski, J. E., "A Study of Axially Symmetrical Base Flow Behind Bodies of Revolution at Supersonic Speed," London University, Ph.D. Thesis, Nov. 1964.
15. Smithey, W., Naber, M., Caswell, G., and Fuhs, A. E., "External Burning Assisted Projectile; Theory and Experiment," AIAA/SAE 9th Propulsion Conference, AIAA Paper No. 73-1193, Nov. 1973.
16. Guderley, G., "On the Application of the Theory of Characteristics to Problems of Supersonic Flow," Ministry of Supply, Armament Research Establishment Translation No. 5/49. pp. 12-18.
17. Hosack, G. A., and O'Leary, R. A., "Base Burning Feasibility Investigation," North American Rockwell Rocketdyne, Technical Report No. RK - TR- 70-17, Dec. 1970, pp. 50-65.
18. Liepmann, H. W., and Roshko, A., "Elements of Gasdynamics," John Wiley & Sons, Inc., 1957, pp. 191-193, 284-296, 226-233.
19. Ziercp, J., "Ähnlichkeitsgesetze für Profilströmungen mit Wärmezufuhr," Acta Mechanica, Vol. 1, 1965, pp. 60-70.
20. Ashley, H., and Landahl, M., "Aerodynamics of Wings and Bodies," Addison-Wesley, 1965, p. 154.
21. Ludloff, H. F., and Reiche, F., "Linearized Supersonic Flow Through Ducts," J. Appl Physics., Vol. 18, July 1947, pp. 681-682.
22. Mack, C. E. Jr., Ludloff, H. F., and Reiche, F., "Rigorous Solution of Linearized Flow Through Ducts," J.App. Physics, Vol. 18, July 1947, pp. 682-683.
23. Ludloff, H. F., and Reiche, F., "Linearized Treatment of Supersonic Flow Through Ducts," J. Aero.Sci., Vol. 16, Jan. 1949, pp. 5-21.



24. Schlichting, H., "Boundary Layer Theory," McGraw-Hill, Inc., Fourth Ed., 1960, Chapt. XII, also pp. 25, 38, 541, 545.
25. Darling, J. A., and Knott, J., "Effect of Spin on the Aerodynamics of the 20mm Projectile," NOLTR 71-180, Sept. 1971.
26. Lehnert, R., and Hastings, S. M., "Spin Effects on Base Pressure of Cone Cylinders at  $M=2.86$ ," Naval Ordnance Laboratory, TR 2956, Oct. 1953.
27. Schmidt, L. E., and Murphy, C. H., "Effect of Spin on Aerodynamic Properties of Bodies and Revolution," USA Ballistic Research Laboratories, Memorandum Report No. 715, August 1953.
28. Smithey, W., Naber, M., Caswell, G., and Fuhs, A. E., "An Open Jet Wind Tunnel for External Burning with Spinning Projectiles," AIAA/SAE 9th Propulsion Conference, Nov. 1973, AIAA Paper No. 73-1225.
29. Smithey, W., Naber, M., Caswell, G., and Fuhs, A. E., "External Burning Assisted Projectile - A Progress Report," 10th JANNAF Combustion Meeting Proceedings, Vol. 11 (CPIA Pub. 243, Dec. 1973) pp. 193-205.
30. Kolpin, M. A., Horn, K. P., and Reicherbach, R. E., "Study of Penetration of a Liquid Injectant into a Supersonic Flow," AIAA Journal, Vol. VI, May 1968, pp. 853-858.
31. Shapiro, A. H., "The Dynamics and Thermodynamics of Compressible Flow," Two Volumes, Ronald Press, 1954, pp. 540, 790-791.
32. van Hise, Vernon, "Investigation of Variation in Base Pressure Over the Reynolds Number Range in Which Wake Transition Occurs for Nonlifting Bodies of Revolution at Mach Numbers from 1.62 to 2.62," NACA Technical Note 3942, January 1957.
33. van Hise, Vernon, "Investigation of Variation in Base Pressure Over the Reynolds Number Range in which Wake Transition Occurs for Two-Dimensional Bodies at Mach Numbers from 1.95 to 2.92," NASA Technical Note D-167, November 1959.
34. Murthy, S. N. B. and Osborn, J. R., "Base Flow Data with and without Injection: Bibliography and Semi-Rational Correlations," USA Ballistics Research Laboratories Contract Report No. 113, August 1973.





35. Chang, P. K., "Separation of Flow," Pergamon Press, Inc., 1970, pp. 543-549.
36. Korst, H. H., "Component Analysis and Synthesis for Fully Separated Flows with Special Consideration of Base Drag by Combustion," Workshop on Aerodynamics of Base Combustion, School of Mechanical Engineering, Purcuc University, May 1974.
37. Probststein, R. F., "Inversion of the Prandtl-Meyer Relation for Specific - Heat Ratios of  $5/3$  and  $5/4$ "; J. Aero Sci., Apr. 1957, pp. 316-317.



# INITIAL DISTRIBUTION LIST

No. Copies

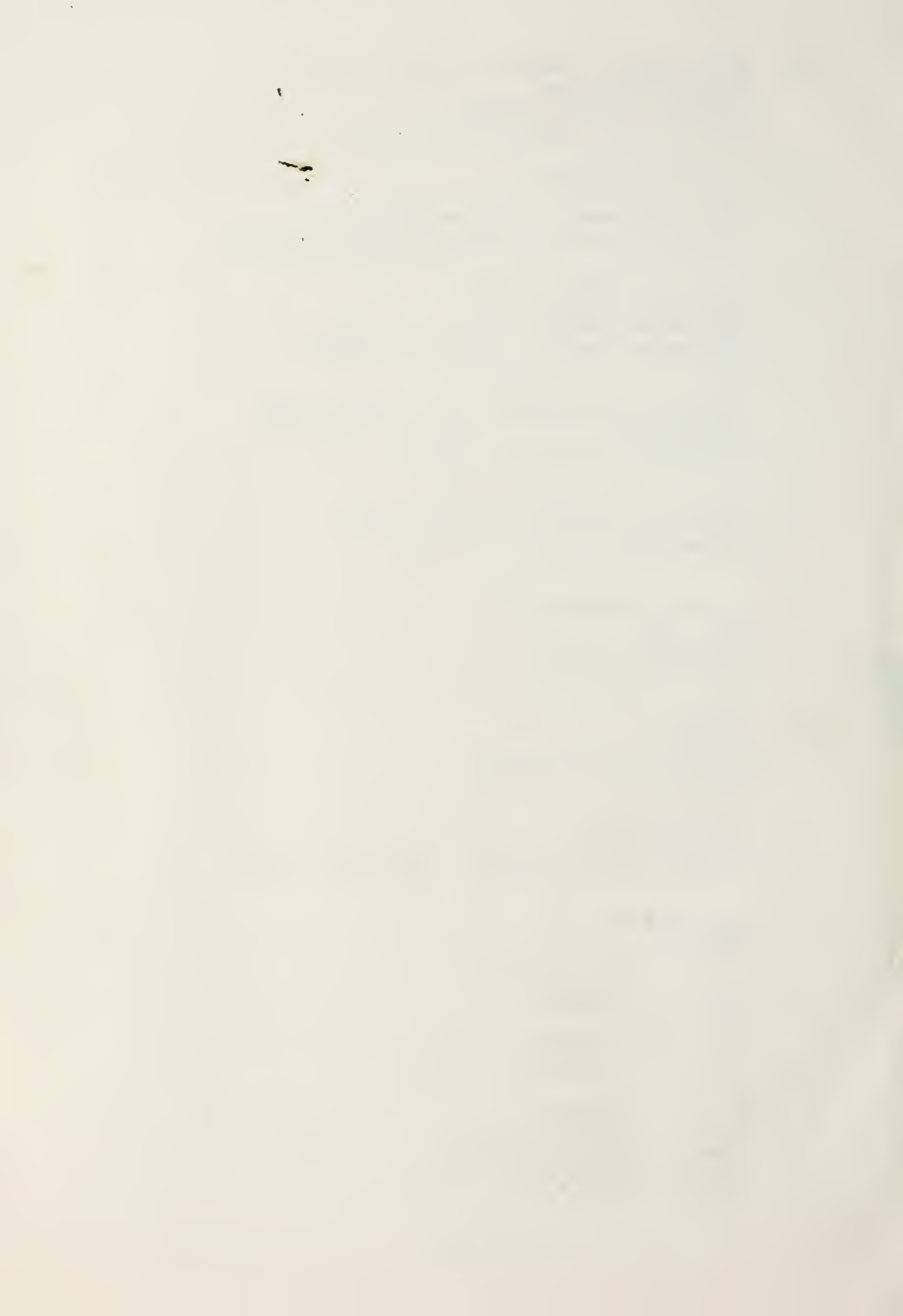
1. Defense Documentation Center 2  
Cameron Station  
Alexandria, Virginia 22314
2. Library, Code 0212 2  
Naval Postgraduate School  
Monterey, California 93940
3. Professor A. E. Fuhs 10  
Department of Aeronautics  
Naval Postgraduate School  
Monterey, California 93940
4. LTjg Gary J. Caswell, USN 1  
399 Troy  
Aurora, Colorado 80010
5. Dr. Warren Strahle 1  
Aerospace Engineering  
Georgia Institute of Technology  
Atlanta, Georgia 30332
6. Mr. Dominic J. Monetta 2  
Gun Systems Engineering  
Naval Ordnance Station  
Indian Head, Maryland 20640
7. Dr. Alan Roberts 5  
Gun Systems Engineering  
Naval Ordnance Station  
Indian Head, Maryland 20640
8. Dr. Frederick Billig 1  
Applied Physics Laboratory  
Johns Hopkins University  
8621 Georgia Avenue  
Silver Springs, Maryland 20910
9. CDR William Smithey 5  
207 Hillside St., N.W.  
Lenoir, N. C. 28645



10. Dr. James S. Holdhusen 1  
Vice President  
Fluidyne Engineering Corporation  
5900 Olsen Highway  
Minneapolis, Minnesota 55422
11. Mr. Thomas Curran 1  
Chief of Ramjet Technology Branch  
Air Force Aero Propulsion Laboratory  
Wright Patterson Air Force Base, Ohio 45433
12. LT Noel P. Horn, USN 1  
SMC, Box 1183  
Naval Postgraduate School  
Monterey, California 93940
13. Dr. Richard Weiss 1  
Air Force Rocket Propulsion Laboratory  
Edwards Air Force Base, California
14. Professor John Clarke 1  
Cranfield Institute of Technology  
Bedford, ENGLAND
15. Dr. E. G. Broadbent 1  
Royal Aeronautical Establishment  
Farnborough, ENGLAND
16. Chairman, Department of Aeronautics 1  
Naval Postgraduate School  
Monterey, California 93940
17. Dr. Ing. G. Winterfeld 1  
D F V L R  
Institut f. Luftstrahlantriebe  
505 Porz-Wahn, Linder Höhe  
GERMANY
18. LT M. Naber 1  
RT. 1, Box 1048  
Sequim, Washington 98382
19. Dr. Andrew Mark (AMXBR-EB) 1  
Ballistic Research Lab.  
Aberdeen Proving Grounds, Maryland 21005
20. LT L. Michael Freeman 1  
ARL/LH  
Wright Patterson Air Force Base, Ohio 45433
21. Professor G. W. Zumwalt 1  
6311 Marjorie Lane  
Wichita, Kansas 67208



22. Miss Theresa Elmendorf (SARFA-MDS-B) 1  
Frankford Arsenal  
Bridge & Tacony Streets  
Philadelphia, Pennsylvania 19137
23. Dr. Raymond Sedney 1  
EBL, Bldg. 120  
Ballistic Research Laboratory  
Aberdeen Proving Grounds, Maryland 21005
24. Dr. H. H. Tang, A3-253 1  
McDonnell Douglas Corp.  
5301 Bolsa Avenue  
Huntington Beach, California 92647
25. Professor J. A. Schetz 1  
Virginia Polytechnic Institute & State  
University  
Blacksburg, Virginia 24061
26. Professor H. Doyle Thompson 1  
School of Mechanical Engineering  
Purdue University  
W. Lafayette, Indiana 47907
27. Mr. Henry Hudgins 1  
Bldg. 350  
Picatinny Arsenal  
Dover, New Jersey 07801
28. Professor H. H. Korst 1  
210 MEL  
University of Illinois  
Urbana, Illinois 61820
29. Dr. J. R. Ward 1  
Ballistic Research Laboratory, Bldg. 390  
Aberdeen Proving Ground, Maryland 21005
30. Mr. Dan Jones III 1  
Code GPA  
NWL Dahlgren, Virginia
31. LCDR H. W. Burden 1  
Code 57Zt  
Naval Postgraduate School  
Monterey, California 93940
32. Dr. D. W. Netzer 1  
Department of Aeronautics  
Naval Postgraduate School  
Monterey, California 93940





30 MAY 75

16 AUG 77

16 AUG 77

22063

24817

24817

153702

Thesis

S624

c.1

Smithey

Projectile thrust-drag  
optimization with external  
burning.

30 MAY 75

16 AUG 77

16 AUG 77

220637

24817

Thesis

S624

c.1

Smithey

Projectile thrust-drag  
optimization with external  
burning.

153702

thesS624

Projectile thrust-drag optimization with



3 2768 002 00804 7

DUDLEY KNOX LIBRARY